

# **Rotating Equipment Defect Detection Using the Algorithm of Mode Isolation**

A Thesis  
Presented to  
The Academic Faculty

by

**Benjamin B. Wagner**

In Partial Fulfillment  
of the Requirements for the Degree  
Doctor of Philosophy

Woodruff School of Mechanical Engineering  
Georgia Institute of Technology  
August 2007

Copyright © 2007 by Benjamin B. Wagner

# Rotating Equipment Defect Detection Using the Algorithm of Mode Isolation

Approved by:

Dr. Jerry H. Ginsberg, Chair  
School of Mechanical Engineering  
*Georgia Institute of Technology*

Dr. Aldo A. Ferri  
School of Mechanical Engineering  
*Georgia Institute of Technology*

Dr. Olivier A. Bauchau  
School of Aerospace Engineering  
*Georgia Institute of Technology*

Dr. Itzhak Green  
School of Mechanical Engineering  
*Georgia Institute of Technology*

Dr. Dewey H. Hodges  
School of Aerospace Engineering  
*Georgia Institute of Technology*

Date Approved: February 2007

## ACKNOWLEDGEMENTS

I would like to thank my advisor, Dr. Jerry H. Ginsberg, for the vast and varied support he provided during the course of my work at Georgia Tech. Dr. Ginsberg worked with me to ease my transition from industry back into the academic environment. He remained patient through the many setbacks in my program. Dr. Ginsberg also financially supported my research effort for four years, through the George W. Woodruff Chair in Mechanical Systems.

I would like to thank the members of my thesis committee: Dr. Aldo A. Ferri, Dr. Itzhak Green, Dr. Dewey H. Hodges, and Dr. Olivier A. Bauchau. A considerable amount of time is involved in the thesis process. I appreciate their valuable input and their willingness to serve.

I would be remiss if I did not publicly record my gratitude to Dr. Green. My degree program would have ended in failure at the point of the Ph.D. Qualifying Examinations, had it not been for his actions.

My classmate and labmate, Dr. Matthew S. Allen, generously shared with me his impressive knowledge of experimental modal analysis, dynamics, vibrations, and linear algebra. My work was bolstered by his patient explanations of complex material, and I have been enriched by his friendship.

I will never be able to adequately thank my wife, Christy, for her continuing love and support. As I wrestled with the highs and lows of my degree program, Christy and our children, John and Hannah, kept me firmly connected to the world outside academia and to those aspects of life that are truly important. For this, I will always be grateful.

Finally, I must acknowledge Almighty God. Without His support, the extent of which is truly known only to Him, none of this would have been possible.

# TABLE OF CONTENTS

<b>ACKNOWLEDGEMENTS</b>	<b>iii</b>
<b>LIST OF TABLES</b>	<b>viii</b>
<b>LIST OF FIGURES</b>	<b>xi</b>
<b>SUMMARY</b>	<b>xiv</b>
<b>I INTRODUCTION</b>	<b>1</b>
1.1 Motivation . . . . .	1
1.2 Hypothesis . . . . .	2
1.3 Objectives . . . . .	2
<b>II BACKGROUND AND LITERATURE REVIEW</b>	<b>4</b>
2.1 Modal Parameter Identification Methods . . . . .	4
2.1.1 Analytical Concepts . . . . .	5
2.1.2 Literature Review . . . . .	9
2.1.3 Complex Modal Analysis . . . . .	12
2.2 Bearing Faults and Bearing Fault Detection . . . . .	14
2.2.1 Hydrodynamic Bearings . . . . .	14
2.2.2 Hydrodynamic Bearing Fault Detection . . . . .	16
2.2.3 Rolling Element Bearings . . . . .	16
2.2.4 Rolling Element Bearing Fault Detection . . . . .	17
2.2.5 Comment on the Use of Rolling Element Bearings in the Proposed Work . . . . .	17
2.3 Shaft Cracks and Shaft Crack Detection . . . . .	18
2.3.1 Breathing Cracks . . . . .	18
2.3.2 Gaping Cracks . . . . .	19
2.3.3 Stiffness and Damping Effects . . . . .	19
2.3.4 Shaft Crack Detection . . . . .	21
2.4 Algorithm of Mode Isolation . . . . .	23
2.4.1 Comment on the Use of AMI . . . . .	24

<b>III</b>	<b>PROTOTYPICAL SYSTEM</b>	<b>26</b>
3.1	Introduction . . . . .	26
3.2	System Parameters . . . . .	26
3.3	Brief Description of Models . . . . .	27
3.4	Simplified Model of Prototypical System (Uncracked Shaft) . . . . .	28
3.4.1	Description . . . . .	28
3.4.2	Ritz Series Analysis . . . . .	28
3.4.3	Equations of Motion . . . . .	29
3.4.4	Model Use . . . . .	30
3.5	Use of Short-Bearing Model . . . . .	30
3.6	Bearing Wear Description . . . . .	33
3.7	Conversion Between Fixed And Moving Coordinate Systems . . . . .	34
3.8	Standard Model of Prototypical System (Cracked Shaft) . . . . .	36
3.8.1	Type of Crack Model . . . . .	36
3.8.2	Modification of Shaft Model . . . . .	37
3.8.3	Ritz Series Analysis . . . . .	40
3.8.4	Equations of Motion . . . . .	44
3.8.5	Crack Damping . . . . .	45
3.8.6	Model Use . . . . .	46
<b>IV</b>	<b>EVALUATION OF THE DIRECTIONAL FREQUENCY RESPONSE FUNCTION (DFRF)</b>	<b>47</b>
4.1	Introduction . . . . .	47
4.2	Development of Two-Sided AMI to Process dFRFs . . . . .	47
4.3	Two-Sided AMI Testing with Rigid Rotor System . . . . .	49
4.3.1	Analytical Model Description . . . . .	49
4.3.2	Results . . . . .	50
4.3.3	Discussion . . . . .	53
4.4	Two-Sided AMI Testing with Prototypical System (Simplified Model) . . .	58
4.4.1	Results . . . . .	58
4.4.2	Discussion . . . . .	59

<b>V</b>	<b>EVALUATION OF EIGENVALUES AND RESIDUES FOR USE IN DETECTION OF A WORN BEARING</b>	<b>67</b>
5.1	Potential Damage Metrics . . . . .	67
5.1.1	Detectability . . . . .	68
5.2	Analysis Method . . . . .	69
5.3	Results . . . . .	70
5.3.1	Detectability Using Eigenvalues . . . . .	71
5.3.2	Detectability Using Residues . . . . .	73
5.4	Discussion . . . . .	76
<b>VI</b>	<b>EVALUATION OF EIGENVALUES AND RESIDUES FOR USE IN DETECTION OF A SHAFT CRACK</b>	<b>79</b>
6.1	Introduction . . . . .	79
6.2	Method Overview . . . . .	81
6.3	Detectability Concepts . . . . .	83
6.3.1	Calculation of Detectability Bands . . . . .	83
6.4	Measurement Noise Model . . . . .	88
6.5	Time Domain Solution Procedure . . . . .	89
6.6	Exponential Window for Time Response . . . . .	91
6.7	Valid Frequency Range of Prototypical System Model . . . . .	93
6.8	Analysis Method . . . . .	95
6.9	Results . . . . .	97
6.9.1	Time Domain Response . . . . .	97
6.9.2	Frequency Domain Response . . . . .	100
6.9.3	Detectability Plots . . . . .	107
6.9.4	Detectability Summary . . . . .	112
6.10	Discussion . . . . .	117
<b>VII</b>	<b>DEFECT DETECTION WITH MULTIPLE DEFECTS PRESENT</b>	<b>130</b>
7.1	Introduction . . . . .	130
7.2	Method Overview . . . . .	130
7.3	Analysis Method . . . . .	132
7.4	Results . . . . .	133

7.4.1	Constant Shaft Crack and Increasing Bearing Wear . . . . .	135
7.4.2	Constant Bearing Wear and Increasing Shaft Crack . . . . .	136
7.5	Discussion . . . . .	137
7.5.1	Constant Shaft Crack and Increasing Bearing Wear . . . . .	139
7.5.2	Constant Bearing Wear and Increasing Shaft Crack . . . . .	140
7.5.3	General . . . . .	141
<b>VIII</b>	<b>SUMMARY AND CONCLUSIONS</b>	<b>144</b>
<b>IX</b>	<b>FUTURE WORK</b>	<b>149</b>
<b>APPENDIX A</b>	<b>— BEARING COEFFICIENTS</b>	<b>152</b>

## LIST OF TABLES

1	Comparison of prototypical system eigenvalues for the 8-coefficient and 16-coefficient short bearing models. . . . .	33
2	Frequency domain comparison: effects of converting FRF and dFRF data from fixed to moving coordinate system. . . . .	36
3	Rigid rotor system; isotropic case. Analytical eigenvalues, Two-Sided AMI estimated eigenvalues, AMI estimated eigenvalues, and percent error for modes 1 and 2 of isotropic system. (+) = detected in positive frequency range, (-) = detected in negative frequency range, and (+/-) = detected in both ranges with average value reported. . . . .	51
4	Rigid rotor system; isotropic case. Analytical eigenvalues, Two-Sided AMI estimated eigenvalues, AMI estimated eigenvalues, and percent error for modes 3 and 4 of isotropic system. (+) = detected in positive frequency range, (-) = detected in negative frequency range, and (+/-) = detected in both ranges with average value reported. . . . .	53
5	Rigid rotor system; anisotropic case. Analytical eigenvalues, Two-Sided AMI estimated eigenvalues, AMI estimated eigenvalues, and percent error for modes 1 and 2 of anisotropic System. (+) = detected in positive frequency range, (-) = detected in negative frequency range, and (+/-) = detected in both ranges with average value reported. . . . .	56
6	Rigid rotor system; anisotropic case. Analytical eigenvalues, Two-Sided AMI estimated eigenvalues, AMI estimated eigenvalues, and percent error for modes 3 and 4 of anisotropic system. (+) = detected in positive frequency range, (-) = detected in negative frequency range, and (+/-) = detected in both ranges with average value reported. . . . .	56
7	Prototypical system; nominal condition. Analytical eigenvalues and damping ratios for all underdamped modes below 120 nondimensional frequency units. . . . .	63
8	Prototypical system (simplified model); nominal condition. Analytical eigenvalues, eigenvalues estimated by AMI processing of FRF, and eigenvalues estimated by Two-Sided AMI processing of FRF for two lower-frequency detected modes. (+) = detected in positive frequency range, (-) = detected in negative frequency range, and (+/-) = detected in both ranges with average value reported. . . . .	64
9	Prototypical system (simplified model); nominal condition. Analytical eigenvalues, eigenvalues estimated by AMI processing of FRF, and eigenvalues estimated by Two-Sided AMI processing of FRF for two higher-frequency detected modes. (+) = detected in positive frequency range, (-) = detected in negative frequency range, and (+/-) = detected in both ranges with average value reported. . . . .	65



10	Prototypical system (simplified model); nominal condition. Analytical eigenvalues and eigenvalues estimated by Two-Sided AMI processing of dFRF for two lower-frequency detected modes. (+) = detected in positive frequency range, (-) = detected in negative frequency range, and (+/-) = detected in both ranges with average value reported. . . . .	65
11	Prototypical system (simplified model); nominal condition. Analytical eigenvalues and eigenvalues estimated by Two-Sided AMI processing of dFRF for two higher-frequency modes. (+) = detected in positive frequency range, (-) = detected in negative frequency range, and (+/-) = detected in both ranges with average value reported. . . . .	66
12	Bearing radial clearances used to simulate wear of Bearing 1. . . . .	70
13	Performance of eigenvalue-based damage metrics for FRF and dFRF data. . . . .	74
14	Performance of residue-based damage metrics for FRF and dFRF data. . . . .	75
15	Clean data detectability band values (estimation error of AMI and Two-Sided AMI for prototypical system in uncracked condition). Error values and absolute values of analytical quantities averaged over the identified peaks. . . . .	87
16	Noisy data detectability band values (estimation error of AMI and Two-Sided AMI, adjusted with noise confidence interval, for prototypical system in uncracked condition). Error values and absolute values of analytical quantities averaged over the identified peaks. . . . .	89
17	Shaft cracks used in analysis. . . . .	97
18	Crack detection performance of eigenvalue-based damage metrics for clean fixed reference frame FRF and dFRF data. . . . .	122
19	Crack detection performance of residue-based damage metrics for clean fixed reference frame FRF and dFRF data. . . . .	123
20	Crack detection performance of eigenvalue-based damage metrics for clean moving reference frame FRF and dFRF data. . . . .	124
21	Crack detection performance of residue-based damage metrics for clean moving reference frame FRF and dFRF data. . . . .	125
22	Crack detection performance of eigenvalue-based damage metrics for noisy fixed reference frame FRF and dFRF data. . . . .	126
23	Crack detection performance of residue-based damage metrics for noisy fixed reference frame FRF and dFRF data. . . . .	127
24	Crack detection performance of eigenvalue-based damage metrics for noisy moving reference frame FRF and dFRF data. . . . .	128
25	Crack detection performance of residue-based damage metrics for noisy moving reference frame FRF and dFRF data. . . . .	129
26	Operating conditions for standard model of prototypical system in dual defect study. . . . .	132

27	Defect detection performance of damage metrics with two defects present. Crack held constant at 0.3 relative depth while bearing clearance increased. Noisy, fixed reference frame data. . . . .	142
28	Defect detection performance of damage metrics with two defects present. Bearing clearance held constant at 20 percent increase from nominal while crack depth increased. Noisy, fixed reference frame data. . . . .	143

## LIST OF FIGURES

1	Prototypical System. . . . .	30
2	Relationships between axes and rotations for a differential shaft element. . .	31
3	Rigid rotor system [38]. . . . .	50
4	Rigid rotor system; isotropic case. FRF $H_{YY}$ at bearing 1. . . . .	52
5	Rigid rotor system; isotropic case. FRF $H_{ZY}$ at bearing 1. . . . .	52
6	Rigid rotor system; isotropic case. dFRF $H_{PG}$ at bearing 1. . . . .	54
7	Rigid rotor system; anisotropic case. FRF $H_{YY}$ at bearing 1. . . . .	54
8	Rigid rotor system; anisotropic case. FRF $H_{ZY}$ at bearing 1. . . . .	55
9	Rigid rotor system; anisotropic case. dFRFs $H_{PG}$ (solid) and $H_{P\hat{G}}$ (dashed) at bearing 1. . . . .	55
10	Prototypical system (simplified model); nominal condition. Magnitude, real part, and imaginary part of FRF $H_{YY}$ at bearing 1. . . . .	60
11	Prototypical system (simplified model); nominal condition. Magnitude, real part, and imaginary part of FRF $H_{ZY}$ at bearing 1. . . . .	61
12	Prototypical system (simplified model); nominal condition. Magnitude, real part, and imaginary part of dFRF $H_{PG}$ at bearing 1. . . . .	62
13	Prototypical system (simplified model); nominal condition. Magnitude, real part, and imaginary part of dFRF $H_{P\hat{G}}$ at bearing 1. . . . .	62
14	Detectability of eigenvalue properties using percent change $\text{Re}(\lambda)$ and percent change $\text{Im}(\lambda)$ for the nominal $\lambda = -1.2695 + 33.1138i$ mode. . . . .	72
15	Detectability of residue properties using percent change $\text{Re}(A)$ and percent change $\text{Im}(A)$ with the nominal $\lambda = -1.2695 + 33.1138i$ mode identified from $H_{YY}$ at bearing 1. . . . .	73
16	Sample detectability plot. . . . .	84
17	Percent error in AMI-estimated $\text{Re}(\lambda)$ versus exponential window coefficient $\beta$ . Solid = $-1.2568 + i5.4879$ mode. Dashed = $-1.2695 + i33.1281$ mode. . . . .	92
18	Percent error in AMI-estimated $\text{Im}(\lambda)$ versus exponential window coefficient $\beta$ . Solid = $-1.2568 + i5.4879$ mode. Dashed = $-1.2695 + i33.1281$ mode. . . . .	93
19	FRF $H_{ZZ}$ of nominal system calculated from time domain response of simplified model of prototypical system. . . . .	95
20	FRF $H_{ZZ}$ of nominal system calculated from time domain response of standard model of prototypical system. . . . .	96

21	Z-direction response of nominal system at Bearing 1 due to Z-direction impulse at Bearing 1. Clean, unwindowed, fixed $XYZ$ data. . . . .	98
22	Y-direction response of nominal system at Bearing 1 due to Z-direction impulse at Bearing 1. Clean, unwindowed, fixed $XYZ$ data. . . . .	98
23	Z-direction response of nominal system at Bearing 1 due to Z-direction impulse at Bearing 1. Noisy, unwindowed, fixed $XYZ$ data. . . . .	99
24	Z-direction response of nominal system at Bearing 1 due to Z-direction impulse at Bearing 1. Noisy, windowed, fixed $XYZ$ data. . . . .	99
25	$z$ -direction response of nominal system at Bearing 1 due to Z-direction impulse at Bearing 1. Noisy, windowed, moving $xyz$ data. . . . .	100
26	Z-direction response at Bearing 1, due to Z-direction impulse at Bearing 1, of system with crack of 0.4 relative depth. Noisy, windowed, fixed $XYZ$ data.	101
27	$z$ -direction response at Bearing 1, due to Z-direction impulse at Bearing 1, of system with crack of 0.4 relative depth. Noisy, windowed, moving $xyz$ data.	101
28	FRF $H_{ZZ}$ of nominal system at Bearing 1, due to impulse at Bearing 1. Clean, windowed, fixed $XYZ$ data . . . . .	102
29	dFRF $H_{PG}$ of nominal system at Bearing 1, due to impulse at Bearing 1. Clean, windowed, fixed $XYZ$ data . . . . .	103
30	dFRF $H_{P\hat{G}}$ of nominal system at Bearing 1, due to impulse at Bearing 1. Clean, windowed, fixed $XYZ$ data . . . . .	103
31	FRF $H_{ZZ}$ of nominal system at Bearing 1, due to impulse at Bearing 1. Clean, windowed, moving $xyz$ data . . . . .	104
32	dFRF $H_{PG}$ of nominal system at Bearing 1, due to impulse at Bearing 1. Clean, windowed, moving $xyz$ data . . . . .	105
33	dFRF $H_{P\hat{G}}$ of nominal system at Bearing 1, due to impulse at Bearing 1. Clean, windowed, moving $xyz$ data . . . . .	105
34	FRF $H_{ZZ}$ of nominal system at Bearing 1, due to impulse at Bearing 1. Noisy, windowed, fixed $XYZ$ data . . . . .	106
35	dFRF $H_{PG}$ of nominal system at Bearing 1, due to impulse at Bearing 1. Noisy, windowed, fixed $XYZ$ data . . . . .	106
36	dFRF $H_{P\hat{G}}$ of nominal system at Bearing 1, due to impulse at Bearing 1. Noisy, windowed, fixed $XYZ$ data . . . . .	107
37	FRF $H_{ZZ}$ at Bearing 1, due to impulse at Bearing 1, for system with crack of 0.2 relative depth. Noisy, windowed, fixed $XYZ$ data. . . . .	108
38	dFRF $H_{PG}$ at Bearing 1, due to impulse at Bearing 1, for system with crack of 0.2 relative depth. Noisy, windowed, fixed $XYZ$ data. . . . .	108
39	dFRF $H_{P\hat{G}}$ at Bearing 1, due to impulse at Bearing 1, for system with crack of 0.2 relative depth. Noisy, windowed, fixed $XYZ$ data. . . . .	109

40	FRF $H_{ZZ}$ at Bearing 1, due to impulse at Bearing 1, for system with crack of 0.4 relative depth. Noisy, windowed, fixed $XYZ$ data. . . . .	109
41	dFRF $H_{PG}$ at Bearing 1, due to impulse at Bearing 1, for system with crack of 0.4 relative depth. Noisy, windowed, fixed $XYZ$ data. . . . .	110
42	dFRF $H_{P\hat{G}}$ at Bearing 1, due to impulse at Bearing 1, for system with crack of 0.4 relative depth. Noisy, windowed, fixed $XYZ$ data. . . . .	110
43	Detectability chart for $\text{Re}(A)$ . FRF $H_{ZZ}$ constructed with clean, fixed $XYZ$ coordinate system data. Horizontal dashed lines are detectability band limits.	111
44	Detectability chart for $\text{Im}(\lambda)$ . Negative frequency range dFRF $H_{PG}$ constructed with clean, fixed $XYZ$ coordinate system data. Horizontal dashed lines are detectability band limits. . . . .	112
45	Detectability chart for $\text{Im}(\lambda)$ . Negative frequency range dFRF $H_{P\hat{G}}$ constructed with clean, fixed $XYZ$ coordinate system data. Horizontal dashed lines are detectability band limits. . . . .	113
46	Detectability chart for $\text{Im}(\lambda)$ . Negative frequency range dFRF $H_{P\hat{G}}$ constructed with noisy, fixed $XYZ$ coordinate system data. Horizontal dashed lines are detectability band limits. . . . .	114
47	FRF $H_{ZZ}$ at Bearing 1, due to impulse at Bearing 1, for system with crack of 0.3 relative depth. Nominal bearing clearance: dotted line. 79% increase in bearing clearance: solid line. Noisy, windowed, fixed $XYZ$ data. . . . .	134
48	dFRF $H_{PG}$ at Bearing 1, due to impulse at Bearing 1, for system with crack of 0.3 relative depth. Nominal bearing clearance: dotted line. 79% increase in bearing clearance: solid line. Noisy, windowed, fixed $XYZ$ data. . . . .	135
49	dFRF $H_{P\hat{G}}$ at Bearing 1, due to impulse at Bearing 1, for system with crack of 0.3 relative depth. Nominal bearing clearance: dotted line. 79% increase in bearing clearance: solid line. Noisy, windowed, fixed $XYZ$ data. . . . .	136
50	FRF $H_{ZZ}$ at Bearing 1, due to impulse at Bearing 1, for system with 20% increase in bearing clearance. Intact shaft: dotted line. Shaft with crack of 0.4 relative depth: solid line Noisy, windowed, fixed $XYZ$ data. . . . .	137
51	dFRF $H_{PG}$ at Bearing 1, due to impulse at Bearing 1, for system with 20% increase in bearing clearance. Intact shaft: dotted line. Shaft with crack of 0.4 relative depth: solid line Noisy, windowed, fixed $XYZ$ data. . . . .	138
52	dFRF $H_{P\hat{G}}$ at Bearing 1, due to impulse at Bearing 1, for system with 20% increase in bearing clearance. Intact shaft: dotted line. Shaft with crack of 0.4 relative depth: solid line Noisy, windowed, fixed $XYZ$ data. . . . .	139

## SUMMARY

Findings from a project involving rotating equipment defect detection using the Algorithm of Mode Isolation (AMI) are presented. The prototypical system evaluated is a rotating shaft, supported by hydrodynamic bearings at both ends, with one disk mounted to the shaft. Shaft cracks and bearing wear are the two equipment defects considered. An existing model of the prototypical system from the literature, termed the “simplified model,” is modified to simulate the presence of a transverse shaft crack at mid-span. This modified model is termed the “standard model.” Ritz series analysis, in conjunction with a previously published description of the compliance related to the presence of a transverse shaft crack, is used to describe the decrease in shaft stiffness associated with the crack.

The directional frequency response function (dFRF) is shown in the literature to provide benefits over the standard frequency response function (FRF) in both system identification and shaft crack detection for rotating equipment. The existing version of AMI is modified to process dFRFs and termed Two-Sided AMI. The performance of Two-Sided AMI is verified through system identification work using both the simplified model and a rigid rotor model from the literature. The results confirm the benefits of using the dFRF for system identification of isotropic systems. AMI and Two-Sided AMI are experimental modal analysis (EMA) routines, which estimate modal properties based on a frequency domain expression of system response. Eigenvalues and associated modal residues are the modal properties considered in the present work.

Three defect detection studies are fully described. In the first, the simplified model is used to investigate bearing wear detection. Various damage metrics related to the eigenvalue and the residue are evaluated. The results show that residue-based metrics are sensitive to bearing wear. Next, the standard model is used in an in-depth investigation of shaft crack detection. When a shaft crack is present, the standard model is time-varying in both the fixed and moving coordinate systems. Therefore, this analysis is also used to evaluate performing EMA on non-modal data. In addition to continuing the evaluation of various

damage metrics, the shaft crack study also investigates the effects of noise and coordinate system choice (fixed or moving) on shaft crack detection. Crack detection through EMA processing of noisy, non-modal data is found to be feasible. The eigenvalue-based damage metrics show promise. Finally, the standard model is used in a dual-defect study. The system is configured with both a shaft crack and a worn bearing. One defect is held constant while the magnitude of the other is increased. The results suggest that AMI is usable for defect detection of rotating machinery in the presence of multiple system defects, even though the response data is not that of a time-invariant system. The relative merits of both input data types, the FRF and the dFRF, are evaluated in each study.

# CHAPTER I

## INTRODUCTION

### *1.1 Motivation*

Predictive maintenance techniques that allow for continuous data collection during normal machinery operation without any additional instrumentation would be economically beneficial for any industry using rotating equipment. Critical pieces of rotating equipment in most industrial and aerospace applications have some form of transducer to monitor displacement, velocity, or acceleration at the bearings. The commonly used mechanical equipment standard API 670 [6] requires the use of two permanently-mounted radial proximity probes per bearing to monitor shaft motion. The similar use of accelerometers is also common. The availability of such dynamical measurements suggests their use for monitoring concepts that make use of recent advances in vibration technology.

Each mode of a system's vibration has a natural frequency and an associated damping ratio, which describes the system's ability to dissipate energy while vibrating in that particular mode. Both quantities depend on the stiffness, damping and inertia properties of the system, as well as the shaft rotation rate and the behavior of the bearings. Changes in the system's physical properties will therefore lead to changes in the system natural frequencies and the associated damping ratios. Additionally, special properties of rotating structures, as compared with nonrotating structures, lead to equal or closely spaced pairs of modes [10].

If conditions are acceptable, the natural frequencies and modal damping ratios can be extracted from the output signal of industry standard instrumentation. However, external flow noise is present during normal operation of aerospace rotating equipment. Industrial rotating equipment is usually installed in close proximity to other operating equipment. Both situations decrease the signal-to-noise ratio of the vibration monitoring transducer's output.



Aerospace gas turbine engines are operated over a wide range of speed and power settings during a single aircraft flight. Some industrial rotating equipment is operated over a speed range corresponding to process conditions. For example, the speed of a boiler’s steam turbine-driven induced-draft fan needs to be varied with boiler load. Other industrial equipment, such as a centrifugal pump driven by an electric motor without a variable frequency drive, operates continually at one speed. Thus, while “normal” operation is almost always assumed to be continuous operation, it can mean fixed- or variable-speed operation. This is significant because the natural frequencies and damping ratios are rotation rate dependent.

These facts suggest that a method to extract modal parameters would be quite useful for machinery health monitoring, but the method will need to work in a noisy environment, have high accuracy, and account for the unique properties of rotordynamic systems.

## ***1.2 Hypothesis***

The natural frequencies and associated damping ratios of a rotating structure can be calculated from system eigenvalues, which are directly related to a system’s physical properties. Hence, changes in physical properties lead to changes in eigenvalues. Bearing wear or a cracked shaft will each change the system’s physical properties. The Algorithm of Mode Identification (AMI) has successfully detected small changes in system eigenvalues in high-noise environments. In addition to the eigenvalue, AMI uses the modal residue to describe a system’s response. It is hypothesized that AMI can be used to process low signal-to-noise ratio vibration data, in order to provide early, reliable detection of bearing defects and shaft cracks through tracking changes to eigenvalues and associated residues.

## ***1.3 Objectives***

The first objective of the research program was to develop an analytical model of a simple rotating system. The model was to simulate the effects of bearing wear and shaft cracks separately, and in combination. The magnitude of the defects was to be adjustable by the user. An analytical model was used in order to avoid the uncertainties regarding the

nominal properties associated with experimental work. The analytical model would provide an unambiguous representation of the defects investigated.

The second objective was to determine the threshold of detectability of each type of defect alone, and in the presence of other defects during constant-speed operation. Industrial standards and guidelines were to be used to quantify normal operating range for bearing clearance. The work was to explore whether AMI is capable of detecting changes in bearing clearance in the normal range of operation. The analytical model was to provide the data for this analysis. The research program was also to investigate whether AMI could improve the current crack detection state-of-the-art.

The third objective was to continue to evaluate AMI's robustness in dealing with noisy data. The effects of the white noise content of the time-domain signal on the threshold of detectability of single and multiple defects were to be quantified.

## CHAPTER II

### BACKGROUND AND LITERATURE REVIEW

#### *2.1 Modal Parameter Identification Methods*

Experimental Modal Analysis (EMA) is a method that allows one to determine a system's modal properties (natural frequencies, associated damping ratios, and mode shapes) by inspection of measured response data. A known input force is used to excite the system, and measured response is fit to a known analytical form in order to identify modal parameters.

System eigenvalues describe two of the three modal properties. The real part of an eigenvalue is proportional to the damping ratio for that mode, while the magnitude of an eigenvalue corresponds to the natural frequency of that mode. The third modal property, the system mode shapes, is given by the associated eigenvectors. (Note that the terms “complete modal solution” and “complete modal definition” indicate that both eigenvalues and eigenvectors are defined.) Since modal parameters are directly related to system physical parameters (mass, stiffness, and damping), changes in modal parameters indicate changes in system physical parameters. With constant operating conditions, changes in system physical parameters typically point to some form of equipment defect.

EMA is less used for rotating structures than it is for non-rotating structures. Symmetry in the system coefficient matrices of non-rotating structures decreases the number of combinations of excitation and measurement points required to provide a complete modal solution. In contrast, the system matrices for rotating systems are not all symmetric. Furthermore, typical rotating equipment has most of the structure of interest for EMA testing, the rotating shaft, sealed inside the machine housing, so it is not readily accessible for measurements. A small portion of the shaft is usually available for excitation or measurement. Using a limited number of measurement points greatly decreases the overall accuracy of any modal estimation, and leads to spatial aliasing.

### 2.1.1 Analytical Concepts

Calculation of the Frequency Response Function (FRF) is central to frequency domain EMA. The FRF for an isotropic rotating system is briefly developed below following Ginsberg [23]. Let  $[M]$  denote the inertia matrix,  $[K]$  the stiffness matrix,  $[C]$  the damping matrix,  $[G]$  the gyroscopic matrix,  $\{q\}$  the  $N$ -length generalized coordinate vector, and  $\{Q\}$  the corresponding generalized force vector. The system matrices are functions of shaft speed,  $\Omega$ , and time,  $t$ , so

$$[M(\Omega, t)] \{\ddot{q}\} + [[C(\Omega, t)] + [G](\Omega, t)] \{\dot{q}\} + [K(\Omega, t)] \{q\} = \{Q\} \quad (1)$$

Analysis in an inertial frame for the case of a rotor having axisymmetry simplifies this to

$$[M] \{\ddot{q}\} + [[C(\Omega)] + [G(\Omega)]] \{\dot{q}\} + [K(\Omega)] \{q\} = \{Q\} \quad (2)$$

The inertia matrix,  $[M]$ , is symmetric, and is not speed dependent. Symmetry of the stiffness matrix,  $[K]$ , and the damping matrix,  $[C]$ , depends on the properties of the bearings. Depending on the definition of the variables contained in  $\{q\}$ , internal or external damping can also be manifested as nonsymmetric terms in the stiffness matrix  $[K]$ . External damping of the rotating shaft, provided only by bearings for a simple system, is beneficial from a stability standpoint, however the follower force portion of the internal damping of the rotating shaft, provided by the shaft material, can decrease stability [23]. The gyroscopic matrix,  $[G]$ , is skew-symmetric and does not lead to dissipative forces. Note that the stiffness and damping matrices include the forces the bearings exert on the rotor. It is implicit to the development that the selection and number of generalized coordinates is sufficient to accurately describe the frequency domain response of the system in the frequency interval of interest.

Consider two coordinate systems. The origin of the moving  $xyz$  coordinate system is attached to the center of the rotating shaft and the  $x$  axis is coincident with the shaft's axial direction. The origin of the inertial  $XYZ$  coordinate system is located at the center of the shaft in the shaft's stationary position, and the  $X$  axis is coincident with the axis of the shaft when it is not rotating. A local stiffness asymmetry is a basic representation of a shaft

crack. In a simple model, the crack is assumed to be of constant depth and opening. In a more complicated model, the depth and size of crack opening could be functions of time. It is less troublesome to describe the behavior of either type of crack model in the moving coordinate system than in the fixed coordinate system. Thus the moving  $xyz$  coordinate system is appropriate for defect detection work searching for shaft cracks [23], [26]. Bearing stiffness and damping may be orthotropic in the fixed  $XYZ$  coordinate system, depending on the type of bearing. In contrast, the bearing stiffness and damping are functions of shaft speed only, so the fixed  $XYZ$  coordinate system is appropriate for analyses that are intended to be used to detect bearing defects.

When  $\{Q\}$  is harmonic at frequency  $\omega$ , with arbitrary complex amplitudes described by  $\{F\}$ , then the steady state response is

$$\{q\} = \text{Re}[\{\Upsilon\} \exp \{i\omega t\}] \quad (3)$$

Substitution into Eq. 2 leads to an equation for the complex amplitudes of the generalized coordinates,

$$\{\Upsilon\} = [[K] + i\omega [[C] + [G]] - \omega^2[M]]^{-1} \{F\} \quad (4)$$

The generalized coordinates are not necessarily the response variables one measures in experimental modal analysis. Let  $\{\hat{q}\}$  denote the set of measured physical displacement variables, and  $\{\hat{Q}\}$  denote the corresponding physical excitations. For a linear structure, these quantities may be evaluated by a condensation of the generalized coordinates and forces. The result is that the physical displacements  $\{\hat{q}\}$  and their complex steady-state amplitudes  $\{\hat{\Upsilon}\}$  are obtained from the corresponding mathematical variables by

$$\{\hat{q}\} = [B] \{q\}, \quad \{\hat{\Upsilon}\} = [B] \{\Upsilon\} \quad (5)$$

where  $[B]$  is a set of constants having fewer rows than columns, corresponding to a coordinate reduction. The virtual work done by the physical forces and by the generalized forces must be the same, which leads to

$$\{Q\} = [B]^T \{\hat{Q}\}, \quad \{F\} = [B]^T \{\hat{F}\} \quad (6)$$

The result of substituting Eqs. 5 and 6 into Eq. 4 is a frequency domain transfer matrix  $[H(\omega)]$ , defined such that

$$\begin{aligned} \{\hat{Y}\} &= [H(\omega)] \{\hat{F}\} \\ [H(\omega)] &= [B] [[K] + i\omega [[C] + [G]] - \omega^2[M]]^{-1} [B]^T \end{aligned} \quad (7)$$

The elements of  $[H(\omega)]$  are the individual FRFs for each displacement-force pair. Note that the eigenvalues of the dynamic stiffness  $[[K] + i\omega [[C] + [G]] - \omega^2[M]]$  correspond to the resonances. Thus, although fewer displacements than the number of degrees of freedom might be processed, all of the natural frequencies lying in any frequency band should be exhibited by each FRF, assuming that neither the excitation nor measurement locations are nodal points for a mode.

One consequence of the skew-symmetry of  $[G]$  and the possible asymmetry of the bearing coefficients is that  $[H(\omega)]$  is not symmetric. Another important property is that it is conjugate-even,

$$H_{jn}(\omega) = H_{jn}(-\omega)^* \quad (8)$$

Standard frequency domain EMA techniques process conjugate-even FRF data over a frequency range from a low limit up to  $\omega_{\max}$ .

One way in which the FRFs can be obtained experimentally is through application of an impulsive excitation. The corresponding impulse response may be computed as a convolution of  $[H(\omega)]$  and the Fourier transform of the physical forces  $\{\hat{Q}\}$ . Analytically, one can generate an FRF by direct frequency domain analysis, as described by Eq. 7. An alternative is to perform a modal analysis using a state-space formulation, as described by Ginsberg [23],

$$\begin{bmatrix} -[K] & [0] \\ [0] & [M] \end{bmatrix} \frac{d}{dt} \begin{Bmatrix} \{q\} \\ \{\dot{q}\} \end{Bmatrix} + \begin{bmatrix} [0] & [K] \\ [K] & [C + G] \end{bmatrix} \begin{Bmatrix} \{q\} \\ \{\dot{q}\} \end{Bmatrix} = \begin{Bmatrix} \{0\} \\ \{Q\} \end{Bmatrix} \quad (9)$$

Ewins [19] gives an alternate state-space form, in which the equations of motion are stacked above the derivative identity, but the modal properties of the alternative formulations are identical to those obtained from the preceding.

The homogeneous solution of the state-space equations is described by a non-self-adjoint linear eigenvalue problem. Defining  $[R]$  and  $[S]$  in the following manner,

$$[R] = - \begin{bmatrix} [0] & [K] \\ [K] & [G] + [C] \end{bmatrix}; [S] = \begin{bmatrix} -[K] & 0 \\ 0 & [M] \end{bmatrix} \quad (10)$$

the problem can be expressed as right and left eigenvalue problems.

$$[[R] - \lambda^R [S]] \{\psi^R\} = \{0\} \quad (11)$$

$$\{\psi^L\}^T [[R] - \lambda^L [S]] = \{0\} \quad (12)$$

Here  $\lambda^R$  is the right eigenvalue,  $\lambda^L$  is the left eigenvalue,  $\{\psi^R\}$  is the right eigenvector, and  $\{\psi^L\}$  is the left eigenvector. The right eigenvalues are equal to the left eigenvalues,

$$\lambda^R = \lambda^L \quad (13)$$

but the right eigenvectors are not equal to the left eigenvectors.

$$\{\psi^R\} \neq \{\psi^L\} \quad (14)$$

The eigenvalues describe the temporal properties of a free modal vibration. Underdamped modes occur as complex conjugate pairs, in which the real part of an eigenvalue is proportional to the mode's damping ratio,  $\zeta_k$ , while the magnitude of each eigenvalue is analogous to the mode's undamped natural frequency,  $\Omega_k$ ,

$$\Omega_k = |\lambda_k|, \quad \zeta_k = -\text{Re}(\lambda_k) / |\lambda_k| \quad (15)$$

The associated complex eigenvectors describe the relative amplitude and phase of the generalized coordinates, all of which are modulated by  $\exp(\text{Re}(\lambda_k t))$  as they oscillate at frequency  $\text{Im}(\lambda_k)$  in a modal free vibration.

The impulse response of each generalized coordinate, and hence, of each physical displacement, can be represented as a superposition of modal responses in which the time dependence has an exponential behavior,  $\exp(\lambda_k t)$ . The frequency domain transfer matrix may be extracted by deconvolving the Fourier transform of the response from the transform of the excitation. If all of the modes are underdamped, which is usually true, the result is

that an FRF is representable as a superposition of poles  $\lambda_k$  and  $\lambda_k^*$ , and associated residues  $A_{jn,k}$  and  $A_{jn,k}^*$ , such that

$$H_{jn}(\omega) = \sum_{k=1}^N \left[ \frac{A_{jn,k}}{i\omega - \lambda_k} + \frac{A_{jn,k}^*}{i\omega - \lambda_k^*} \right] \quad (16)$$

The residues may be expressed as products of the physical displacements in each of the  $N$  pairs of complex conjugate modes.

### 2.1.2 Literature Review

In a lengthy survey of the state of the art of EMA applied to rotating equipment, Bucher and Ewins [10] discussed assumptions and simplifications that could be employed with EMA to get a complete modal solution (all eigenvalues and all eigenvectors) for a rotating shaft in five general configurations. The least complex case discussed was a perfectly axisymmetric shaft with isotropic (equal stiffness in all directions) bearings and no damping. The authors showed that a complete modal solution could be obtained with one excitation point and  $n = N/2$  measured FRFs in one direction. Here,  $n$  is the number of measurement locations, and  $N$  is the number of modes taken into account. For the more realistic case of a system with general anisotropic bearings and some damping, the authors reported that data for one complete column *and* one complete row of the FRF matrix have to be taken in order to get a complete modal solution (eigenvalues and eigenvectors). More complex configurations lead to greater excitation and measurement requirements.

In a separate work, Ewins [20] developed a method based on the symmetry of the mass, stiffness, and damping matrices, to extract complete modal properties from response data with a limited number of excitation locations. Right eigenvectors and complex natural frequencies were used to calculate left eigenvectors. As asymmetry of the stiffness or damping matrix increased, a larger number of columns of the transfer function matrix had to be measured. Even though the method minimized the amount of work for a complete modal solution, in rotating equipment the stiffness and damping matrices are rarely symmetric. Therefore, for the vast majority of systems, at least one column and one row of the transfer function matrix is always required for eigenvector information.



The excitation and measurement location requirements published by Bucher and Ewins, in combination with the limited access to the shaft in operating rotating equipment, make it unlikely that a complete modal solution is attainable for installed equipment operating under normal conditions. However, a number of researchers have reported laboratory methods based on access to many points along the shaft [46], [36], and [37]. In fact, most of the literature details work aimed at producing a complete modal solution.

Marscher [42] proposed a practical method to use the principles of EMA to determine some modal parameters while a piece of rotating equipment is operating normally. An impulse force would be used to excite the shaft and standard accelerometers capture the vibration data. Cumulative time averaging would be used to determine the response due to the impulse force, and the FRF is calculated by dividing the response caused by the impulse force by the cumulative time average of the (input) impulse force spectrum. Marscher specified the use of “standard EMA curve fit / modal synthesis methods” to calculate natural frequencies and associated damping ratios from the FRF. Operational Deflection Shape testing of a boiler feedwater pump was documented in [42], but there is no indication that Marscher’s proposed method was used experimentally.

Redmond [52] analytically investigated methods to quantify hydrodynamic bearing stiffness and damping coefficients. The first method required external excitation of the shaft at several discrete frequencies across the operating speed range of the machine and full knowledge of all shaft displacements and cross-sectional rotations at each bearing. Since this method of excitation and measurement was impractical, Redmond then evaluated the efficacy of unbalance excitation. The method gave acceptable results, but the requirement of knowing the cross-sectional flexural rotations of the shaft at each bearing made the method impractical. Redmond finally focused on a method that used unbalance excitation, ignored the cross-sectional rotations, and only quantified *changes* in the bearing coefficients. Redmond stated that the method produced accurate results if four proximity probes (two more than industry standard) were installed in each bearing. Additionally, evaluation of the method in a high-noise environment was listed as future work.

Santiago and San Andres [56] cited the works of Marscher [42] and Nordmann and

Shollhorn [47] as background for their research on determination of bearing stiffness and damping coefficients through impact testing. The method was developed for nearly rigid shafts and required a special exciter to deliver the impulse to a disk on the rotating shaft. The authors stated that future work would focus on the machine casing as a more practical choice for excitation location. This would remove the requirement for a special exciter, but the analysis would then depend on an accurate model of the support structure.

In 2002, Aenis, Knopf, and Nordmann [1] discussed the use of active magnetic bearings (AMB) for defect identification in rotating equipment. The authors proposed using the AMBs to deliver *and* measure the excitation force required for modal analysis in machinery so equipped. Existing, standard transducers would be used to collect the response data. This multi-purpose use of AMBs would lead to an accurate measurement of the excitation force, a reduction in the level of equipment required for modal analysis, and potential for continuous monitoring. The authors reported acceptable accuracy in analytical testing of model-based fault detection. Experimental work had not been completed.

Bucher and Ewins [10] stated that although AMBs can provide a true multiple-input experimental system, an individual with “considerable” experience is required to run the experiment. Additionally Bucher and Ewins commented that while applying standard excitation methods to a machine’s foundation is simple, extracting meaningful information from the response data is often very difficult.

Bucher and Ewins [10] and Joh and Lee [33] commented on the presence of closely spaced natural frequencies in the frequency response data for rotating structures. Axisymmetry leads to the phenomenon of forward and backward modes. In a forward whirl mode, the rotation of the deflected shaft is in the same direction as shaft rotation, when viewed along the axis of the shaft. In a backward whirl mode, the rotation of the deflected shaft is opposite the shaft rotation. (For both types of modes, shaft deflection is due to transverse vibration.) Typically forward and backward whirl modes appear in pairs, with almost identical natural frequencies. These close natural frequencies usually diverge with increasing rotation rate. Although the motions associated with the modes are unique, the frequency response data for the modes is at least partially overlapped due to the closely

spaced frequencies. Both sets of authors indicated that special techniques are required for accurate discrimination of modes in rotating equipment due to this property. A technique suggested by Joh and Lee is discussed below.

### 2.1.3 Complex Modal Analysis

Lee, Joh, and Kwon developed the directional frequency response function (dFRF) to address this problem [33], [34], and [39]. In this development, displacement and force are broken into two partitions describing motion in two orthogonal planes,  $xy$  and  $xz$  containing the bearing axis  $x$ . The physical transverse displacements and forces are partitioned in the same manner, according to

$$\{\hat{q}\} = \begin{Bmatrix} \{y\} \\ \{z\} \end{Bmatrix}, \quad \{\hat{Q}\} = \begin{Bmatrix} \{Q_y\} \\ \{Q_z\} \end{Bmatrix} \quad (17)$$

The individual partitions are used to define complex time-dependent vectors whose length is half the total number of measured displacements,

$$\{p(t)\} = \{y(t)\} + i\{z(t)\}, \quad \{g\} = \{Q_y\} + i\{Q_z\} \quad (18)$$

A response in which like elements of  $\{y\}$  and  $\{z\}$  oscillate at the same frequency, but with arbitrary amplitude and phase, leads to the elements of  $\{p\}$  being the sum of two phasors of constant length rotating counter-clockwise and clockwise in the complex plane. These phasors correspond to forward and backward whirl at an angular speed that is the oscillation frequency. One of these phasors vanishes if the orbital motion is a synchronous whirl.

The Fourier transform of the complex displacement  $\{p\}$  is denoted as  $\{P(\omega)\}$ , and the Fourier transforms of  $\{g\}$  and  $\{g\}^*$  are denoted as  $\{G(\omega)\}$  and  $\{\hat{G}(\omega)\}$ , respectively, where a caret is used for the latter for the sake of notational convenience. Unlike Fourier transforms of real quantities, these transformed variables are neither conjugate-even nor conjugate-odd, meaning that knowledge of their values for positive frequencies is not sufficient to determine their behavior for negative frequencies. The two-sided directional FRFs are the elements of a transfer function that gives  $\{P(\omega)\}$  in terms of the transformed complex force inputs

$\{G(\omega)\}$ , specifically,

$$\{P(\omega)\} = \begin{bmatrix} [H_{PG}(\omega)] & [H_{P\hat{G}}(\omega)] \end{bmatrix} \begin{Bmatrix} \{G(\omega)\} \\ \{\hat{G}(\omega)\} \end{Bmatrix} \quad (19)$$

The elements of  $[H_{PG}]$  are termed the “normal” dFRF, while  $[H_{P\hat{G}}]$  elements are called the “reverse” dFRF.

Directional FRFs can be expressed in terms of the transfer function for the physical variables. The partitioned form of the definition of  $[H(\omega)]$  is

$$\begin{Bmatrix} \{Y(\omega)\} \\ \{Z(\omega)\} \end{Bmatrix} = \begin{bmatrix} [H_{YY}(\omega)] & [H_{YZ}(\omega)] \\ [H_{ZY}(\omega)] & [H_{ZZ}(\omega)] \end{bmatrix} \begin{Bmatrix} \{F_Y(\omega)\} \\ \{F_Z(\omega)\} \end{Bmatrix} \quad (20)$$

where  $\{Y(\omega)\}$  and  $\{Z(\omega)\}$  are the transforms of  $\{y(t)\}$  and  $\{z(t)\}$ , respectively. Lee [38] showed that the dFRFs may be evaluated from known regular FRFs according to

$$\begin{aligned} 2H_{PG} &= H_{YY} + H_{ZZ} + i(H_{ZY} - H_{YZ}) \\ 2H_{P\hat{G}} &= H_{YY} - H_{ZZ} + i(H_{ZY} + H_{YZ}) \end{aligned} \quad (21)$$

As was mentioned previously, the directional FRFs are not conjugate-even. Consequently, they are considered to be functions covering a range of positive and negative frequencies extending from  $-\omega_{\max}$  to  $\omega_{\max}$ . The loss of conjugate evenness causes the pole-residue form of a dFRF to have a somewhat different representation from that of a regular FRF. Specifically, the consequence of applying Eqs. 21 to Eq. 16 is manifested in a pole-residue form of a directional FRF in which the residue associated with a pole at  $i\omega = \lambda_k^*$  is not the complex conjugate of the residue associated with the pole at  $i\omega = \lambda_k$ . Correspondingly, the conjugate poles are regarded as distinct from their mates, resulting in directional FRFs that are a sum of the contribution of  $2N$  poles and associated residues,

$$dFRF_{jn}(\omega) = \sum_{k=1}^{2N} \left[ \frac{C_{jn,k}}{i\omega - \lambda_k} \right] \quad (22)$$

Like the residues for the standard FRFs, the directional residues  $C_k$  depend solely on the physical displacements in eigensolution  $k$ .

Lee [38] and Joh and Lee [34] discussed the behavior of the normal and reverse dFRFs relative to system isotropy. For an isotropic system, the closely-spaced backward and forward modes commonly associated with rotating structures are completely separated and lie

in the negative and positive frequency ranges, respectively, in the normal dFRF,  $H_{PG}$ . The reverse dFRF,  $H_{P\hat{G}}$ , approaches zero as a slightly anisotropic system approaches isotropy. In an anisotropic system, forward and backward modes are present in both the positive and negative frequency range components of  $H_{PG}$  and  $H_{P\hat{G}}$ .

Mesquita, Dias, and Miranda [44] reviewed FRF and dFRF theory for rotating structures. The researchers employed a finite element representation of a flexible rotor, which was used to evaluate natural frequencies and mode shapes (and directions), as well as FRFs, from which dFRFs were generated. Visual inspection of FRF and dFRF response data was used to illustrate the separation and/or overlapping of backward and forward modes in dFRFs and FRFs of both isotropic and anisotropic systems. EMA algorithm processing of response data was not conducted.

## ***2.2 Bearing Faults and Bearing Fault Detection***

### **2.2.1 Hydrodynamic Bearings**

Hydrodynamic bearings are widely used in rotating equipment such as steam turbines and large centrifugal pumps. Properly designed, installed, and maintained hydrodynamic bearings offer several advantages over rolling element bearings, including no appreciable fatigue concerns and lower radial space requirements.

The stiffness and damping of hydrodynamic bearings are speed-dependent, and the methods used to calculate stiffness and damping coefficients are well-known [13]. The bearing stiffness and damping also depend on the bearing geometry and the lubricant physical properties. Hydrodynamic bearings are subject to abrasive and/or adhesive wear. The overall geometry of the bearing changes long before catastrophic failure [68], so significant changes in the stiffness and damping matrices are present for a relatively long period prior to catastrophic failure of the bearing.

There is limited work on the effects of wear on the stiffness and damping of hydrodynamic bearings. Wu [69] experimentally studied the effects of bearing wear on the performance of a class of reciprocating air compressor with plain journal bearings. New bearings were symmetrically over-bored to simulate bearing wear. A test compressor fitted with bearings

with simulated wear exhibited the same behavior as compressors in the field with actual worn bearings.

As previously mentioned, Redmond [52] performed an analytical evaluation of a method to detect changes in bearing stiffness and damping coefficients due to hydrodynamic bearing wear. Redmond simulated bearing wear by symmetrically increasing the bearing clearance 67% from original in one of two bearings in a mathematical model of an electric motor.

Hashimoto [28], [29] began a detailed analysis by inspecting a number of sets of worn bearings from steam turbines and verified that the bearing wears more directly under the journal's rest position, rather than symmetrically around the entire bearing inner diameter. Hashimoto then developed a mathematical representation of the wear pattern, used finite element analysis to solve for the pressure distribution in the worn bearing, and analytically evaluated the changes in bearing stiffness and damping due to wear. The analytical model was validated by experimental work using bearings CNC-machined to the same wear profile used in the analytical work. Scharrer [59] analytically studied the effects of wear on the stiffness and damping of a hydrostatic journal bearing, using a non-symmetric wear pattern similar to that used by Hashimoto.

Eisenmann [17] defines bearing clearance ratio ( $BCR$ ) as diametral clearance [mills] divided by journal diameter [in]. For properly designed, installed, and maintained horizontal machinery,  $BCR$  is typically between 1.0 and 2.0. Shigley [62] gives guidelines for minimum, average, and maximum bearing clearances in terms of radial bearing clearances. For the prototypical system in the present work, the guidelines are minimum  $BCR = 0.66$ , average  $BCR = 1.5$ , and maximum  $BCR = 2.23$ .

Muszynska [45] conducted analytical and experimental evaluations of the performance of a worn journal bearing in a horizontal machine. In the experimental work, the bearing wear was simulated by symmetrically over-boring the inner diameter of a new bearing. In the analytical work, Muszynska used a simple mathematical model of the rotating shaft based on the first rotor lateral bending mode. The “good” bearing had  $BCR = 13$ , and the “worn” bearing had  $BCR = 133$ . The main thrust of the study was to evaluate the effects of “dead band” (where the journal loses contact with the oil wedge and bearing).

### **2.2.2 Hydrodynamic Bearing Fault Detection**

Oil analysis is a common method for detecting journal bearing wear. The presence of bearing material in the lubricating oil indicates wear. Although on-line oil analysis equipment is available, the most widely-used method to conduct oil analysis is to sample the lubricant, send it to a lab for identification of all solids present, and then evaluate the need for corrective action [9].

Worn hydrodynamic bearings produce a once per revolution (1X) vibration signal. Mass imbalance is the most likely cause of 1X vibration, and another common machinery fault, misalignment, can also produce 1X signals. During diagnosis, orbit analysis (creating a Lissajous pattern by plotting signals from two proximity probes mounted 90 degrees apart in the bearing against one another) is often used to distinguish between imbalance and misalignment. Imbalance typically produces an elliptical orbit, while misalignment produces an orbit that either has a flattened shape or is double-looped. When orbit analysis rules out misalignment, and balance correction does not reduce the 1X vibration, bearing wear is the diagnosis [16].

### **2.2.3 Rolling Element Bearings**

Rolling element bearings are widely used in many types of rotating equipment such as aerospace gas turbine engines and ANSI-specification centrifugal pumps in the power and process industries. Properly installed and maintained rolling element bearings offer lower starting friction, lower axial space requirements, lower sensitivity to lubricant properties, and the ability to carry both radial and thrust loads, when compared with hydrodynamic bearings.

Rolling element bearings have stiffness and damping characteristics considerably different from those of hydrodynamic bearings. Rolling element bearing stiffness depends on bearing preload, geometry and material of construction, and is not speed-dependent. Rolling element bearings have extremely low levels of damping. In fact, analytical rotordynamic models for equipment design and evaluation generally have rolling element bearing damping set equal to zero [16], [13].

The four components of a rolling element bearing are the inner race, the outer race, the rolling elements, and the cage. A defect in any one of the components produces vibration with a unique frequency related to the geometry of the bearing and the operating speed. These fault frequencies are well-known. Damage to the outer race of a bearing is indicated by the “ball pass frequency outer” or BPFO, and damage to the inner race of a bearing is indicated by the “ball pass frequency inner,” or BPFI. The “ball spin frequency” or BSF indicates damage to a rolling element, and the “fundamental train frequency” is associated with damage to the bearing cage. These fault frequencies are much higher than shaft speed [9].

Lee [38], Loparo [41], and many others have published models of rolling element bearing faults as time domain excitation of the system, instead of a change in overall system parameters, as was the case with models for hydrodynamic bearing wear. The bearing stiffness and damping (if included) are assumed to remain constant even though there is a defect on a bearing component. That assumption is valid because of the differences in the types of wear experienced by rolling element bearings and hydrodynamic bearings. Rolling element bearings are subject to fatigue wear where minor surface defects are associated with major subsurface damage. There is almost no change in the overall geometry of the components (and thus the stiffness of the bearing) until there is catastrophic failure.

#### **2.2.4 Rolling Element Bearing Fault Detection**

Diagnostic work on rolling element bearings is most commonly conducted using frequency domain analysis of a vibration signal taken at the bearing. The technology to perform this work is quite mature. Many vendors offer sophisticated software packages that calculate the four fault frequencies for the specific bearings in use, lay them over vibration data taken in the field, and automatically recognize failing bearings.

#### **2.2.5 Comment on the Use of Rolling Element Bearings in the Proposed Work**

The present work does not address fault detection of rolling element bearings. The basic principle of AMI is identifying and detecting changes in system parameters through analysis of system eigenvalues. Rolling element bearing defects manifest themselves as additional



excitations of the system, not as changes in the overall system parameters. An additional excitement produces a system response at the excitation frequency, but system eigenvalues are not modified. The presence of rolling element bearing fault frequencies does not degrade the performance of AMI, so the absence of this type of machine component from proof of concept testing does not rule out the use of AMI on equipment containing rolling element bearings.

## ***2.3 Shaft Cracks and Shaft Crack Detection***

Loaded rotating shafts are susceptible to fatigue cracking, and this susceptibility increases with increasing geometrical complexity and increasing load. Shaft cracking is an ever-present danger to high performance turbomachinery, so there has been significant work done in the areas of analytical modeling of cracks in rotating shafts and development of shaft crack detection methods. Dimarogonas [14] and Wauer [66] both present detailed compilations of this type of work.

### **2.3.1 Breathing Cracks**

The surface of a horizontal rotating shaft is subject to alternating tension and compression due to the weight of the shaft. It is easy to visualize that the effect of this alternating tension and compression on a surface crack is cyclical opening (such that the crack faces are not in contact) and closing (such that the crack faces are in contact) of the crack. A crack exhibiting this behavior is called a breathing crack. As summarized by Casey [12], there are two common methods to analytically model breathing cracks. Either the breathing is defined as a function of displacement perpendicular to the crack edge and the moving  $xyz$  coordinate system is used, or the breathing is defined as a function of the angle of rotation of the shaft and the inertial  $XYZ$  coordinate system is used. Both methods of defining a breathing crack result in elaborate nonlinear analytical models requiring numerical approximation or labor-intensive methods for exact solutions [26]. The response of a breathing crack model consists of the response of a local shaft stiffness asymmetry (1X and 2X effects) plus sub- and/or higher harmonics [15].

### 2.3.2 Gaping Cracks

A gaping crack differs from a breathing crack in that it is always open (the crack faces are never in contact). Therefore, a gaping crack is equivalent to a local stiffness asymmetry in the rotating shaft. This asymmetry is not a function of time when described in the moving  $xyz$  coordinate system. A gaping crack model will accurately describe the response of a cracked shaft if the system vibration amplitudes and static displacements are small [26]. The response of a gaping crack model is equivalent to the response of a local shaft stiffness asymmetry (1X and 2X effects).

### 2.3.3 Stiffness and Damping Effects

In the gaping crack model, the effective cross-sectional area of the shaft is reduced, but there is no contact between the material on either side of the slot. In the breathing crack model, the effective cross-sectional area of the shaft is reduced by the same amount as with a corresponding gaping crack. Additionally, the cyclic loading of the crack causes the rough material on either side of the crack to continually move in and out of contact. Published works [67], [31], [48], discuss the importance to the overall behavior of a crack of the energy loss of this relative motion of rough material during cyclic loading. Neither an analytical gaping crack model, nor a saw-cut slot in an experimental system accounts for the energy loss.

Most researchers have modeled shaft cracks using only stiffness or flexibility. Gasch [22] and Mayes and Davies [43] are examples from the 1970's that use the displacement-based breathing crack model. Both works describe the cracks in terms of additional shaft flexibility (reduced stiffness). In 1998, Wu [70] modeled the behavior of a cracked shaft supported by hydrodynamic bearings. The speed-dependent stiffness and damping of the bearings were taken into account, but the popular stiffness-only breathing crack model was still in use. Dimarogonas [14] lists a large number of crack modeling works based only on flexibility (stiffness).

Relatively few researchers have incorporated both stiffness and damping into shaft crack models. Wauer [67] included the effects of damping in an analytical crack model through

the use of proportional damping. The energy method was used to calculate a stiffness matrix for the continuous prototypical system, and a damping matrix was then created by multiplying the stiffness matrix by the loss factor for the shaft material. Imregun and Sanliturk [31], [58] used a two-part method to develop an analytical model to calculate the equivalent loss factor due to the rubbing action of the two faces of a breathing crack. The first part of the method was to experimentally determine a coefficient of friction across a crack in a sample made from the material of interest. The second part of the method involved an analytical model relating the experimentally determined coefficient of friction, the stress at the crack, the shaft geometry, the crack geometry, the shaft displacement and the increase in damping (loss factor) due to the crack, on a per-mode basis. The crack damping was modeled as Coulomb friction. In comparison with experimental data, the model successfully predicted the effects of changing the crack position and crack depth.

In 2001 Panteliou [48] related crack depth, modal damping factor, and thermodynamic damping in an analytical model derived from first principles. An important result of the analytical work was the determination that modal damping factor increases with increasing crack length.

Zhang [72] conducted experimental work on closure effects on fatigue crack detection using a non-rotating tee section. Closure describes the state where the material on either side of a crack is in contact. Loading may promote closure or prevent closure. Cyclical loading can move the crack in and out of closure during each cycle of motion. Zhang showed that crack closure can obscure the natural frequency changes normally associated with cracked structures (without closure), and that crack closure can accentuate the amount of damping introduced by a crack, when compared to a crack without closure. Zhang also investigated the parametric influence of crack geometry. Zhang defined the frequency range as the original natural frequency minus the new (lower) natural frequency of the cracked structure. The damping ratio and the frequency range increased with increasing crack depth, but the increase was not linear. Also, for increasing load on a structure with a crack of a given size, the frequency range and the damping ratio varied nonlinearly. Zhang concluded from experimental results that analytical crack models need to include

damping effects to accurately approximate physical systems. Furthermore, Zhang agreed with Panteliou’s assertion that damping increases with increasing crack depth.

#### **2.3.4 Shaft Crack Detection**

Crack detection methods can be described as on-line or off-line. In an on-line method, the required excitation and measurement is done with the machine in its normal operating state. Conversely, for an off-line method, the machine is in some state other than normal operation for the excitation and measurement.

Numerous sources discuss analysis of frequency domain vibration data for shaft crack detection. Most researchers point out the importance of the twice per revolution (2X) component in the identification process. The decreased stiffness of the shaft in one direction due to a crack effectively makes the shaft asymmetric. A balanced rotating asymmetric shaft will produce a 2X component [16]. Ehrich [16] went on to say that the 2X component of vibration is often accompanied by “unexplained” high 1X vibration when a cracked shaft is in operation. Huang [30] agreed that the combination of high amplitude 1X and 2X vibration can be an indicator of a cracked shaft. Huang also stated that operating the shaft at one half of the first critical speed optimizes the detection of a cracked shaft using frequency domain data. Green [26] also stressed the importance of the magnitude of the 2X vibration in cracked shaft identification. Green demonstrated that the shaft speed at which the 2X vibration is maximum decreases with increasing crack depth. Lee [39] provided a good summary, in which he stated that it can be difficult to detect cracks with frequency domain techniques because other common machinery faults (misalignment and support nonlinearity) produce similar effects in the vibration frequency spectrum.

Bucher and Shomer [11] developed an on-line method to detect shaft cracks in rotating machinery supported by active magnetic bearings (AMBs). Asynchronous excitation from the AMBs was used to excite the shaft. A peak occurred in the frequency domain response data at a frequency related to both the shaft speed and the frequency of the asynchronous excitation when an asymmetry (a shaft crack) was present. The results showed that the method is reliable for clean (no-noise) signals.

In two related works Garrett *et al.* [7] and Beiryla *et al.* [21] explored the use of on-line torsional vibration analysis to detect shaft cracks. Change in natural frequency was used as the indicator of a crack. Visual inspection of the frequency domain response data was employed to determine natural frequencies. No torsional excitation, other than the machine’s own loading, was used. The authors stated that it was possible that a mode sensitive to a crack could not be excited. The smallest crack detected in the study was 37% relative depth.

Goldman *et al.* [25] presented an on-line method based on lateral and torsional vibration response. Two special pieces of equipment, lateral and torsional nonsynchronous exciters, were used in the perturbation study. Experimental data showed that a crack of 10% relative depth was detectable in a laboratory environment.

Coast down testing is a common off-line method of crack detection [50]. “Coast down” refers to the time while a machine is slowing from normal run speed to a stop after the power source has been removed. The analyst looks for changes in response relative to the previously recorded response of the nominal system. A number of different measures have been presented to quantify the change in response. The magnitude of the vibration, changes in critical speed(s), and changes in the  $Q$  factor [60] are examples.

Often, the vibration data taken during coast down testing is used in conjunction with other data to detect a crack. Sanderson [57] described a typical situation. A propagating crack in a 935 MW turbine-generator set was discovered. The main vibration signature element used in the diagnosis was a large and increasing 1X component. The unit was started and stopped a number of times, and changes in critical speeds of the generator and turbine were also used in the analysis process. Additionally, rotor temperature gradient data was used in the analysis. (The gradient was not normal, indicating the presence of a crack.) Even with all of the available data, and permission to start and stop the machine, the crack reached a relative depth of 25% prior to detection.

Model-based methods have been used for shaft crack detection. The major difficulty with this method is developing an accurate mathematical model for a complex rotating shaft [39]. The rotating shaft is supported by bearings whose stiffness and damping can vary

with speed. Additionally, the interaction of the rotating equipment with the foundation or support on which it rests is important to the overall system dynamics. This interaction is quite difficult to model without extensive field testing of the actual piece of equipment in question [40].

Lee and Kwon [39] and Joh and Lee [34] applied the work on complex modal analysis by Joh and Lee [33], discussed previously, to crack detection. Joh and Lee began to refer to the two-sided FRF as the Directional Frequency Response Function (dFRF). In Equation 19, the  $H_{PG}(\omega)$  term was termed the normal dFRF, and the  $H_{P\hat{G}}(\omega)$  term was called the *reverse* dFRF. The authors used the dFRF to test for anisotropy and asymmetry in rotating systems. Anisotropy referred to nonaxisymmetric properties of the nonrotating elements (bearings, seals, etc.) and asymmetry referred to nonaxisymmetric properties of the rotating shaft (due to cracks, geometry, etc.). The main premise of the method was to compare a fixed reference frame dFRF to the same dFRF in a moving reference frame. Joh and Lee showed experimentally that the method detects the presence of anisotropy and asymmetry, but that a fairly accurate analytical or experimental system model is required to determine the degree of anisotropy or asymmetry.

Lee and Kwon [39] expanded the work on complex modal analysis. By visual inspection of response data generated with an analytical model, the authors demonstrated that the magnitude of the reverse dFRF increased proportional to crack growth and that the phase is shifted by twice the crack opening angular position (relative to some angular reference).

Sabnavis *et al.* [54] compiled a comprehensive list of post-1990 works on the subject of shaft crack detection. The methods were categorized as vibration-based, modal, or other, and off-line methods were differentiated from on-line methods.

## 2.4 *Algorithm of Mode Isolation*

The Algorithm of Mode Isolation (AMI) is a two-phase, frequency domain technique that extracts the modal parameters of identified modes from an FRF in an iterative search. Application of the procedure to several test problems has indicated that the method is accurate, robust in the treatment of noisy data, and does not require an initial guess of the

number of significant modes present. A full explanation of the algorithm and its application is provided by Ginsberg and Allen [24] and Allen and Ginsberg [2].

In the Subtraction Phase of AMI, the most dominant peak in the FRF is identified. In the vicinity of this peak, the FRF is taken to be

$$H(\omega) \approx \frac{A_k}{i\omega - \lambda_k} + \frac{A_k^*}{i\omega - \lambda_k^*}. \quad (23)$$

Single degree of freedom (SDOF) estimates of the corresponding mode's eigenvalue,  $\lambda_k$ , and residue,  $A_k$ , are obtained through a curve-fitting process. These modal parameters are used to subtract that modal contribution from the FRF, which brings the next most dominant peak in the original FRF into prominence. This process is continued until no significant modal content remains in the FRF. In the Isolation Phase, the current estimates of all modal properties, other than the one in focus, are used to subtract the contributions of those modes from the FRF. This leaves the mode in focus as the dominant contributor to the residual FRF. An updated SDOF estimate for that mode is then calculated, using the residual FRF. Each mode identified in the Subtraction Phase is processed sequentially in the same manner. The procedure continues until convergence criteria are met. At the conclusion of Isolation, each mode identified in the FRF is quantified by an eigenvalue - residue pair. The undamped natural frequency,  $\Omega_k$ , modal damping ratio,  $\zeta_k$ , and mode shape,  $\psi_k$ , can be extracted from the eigenvalue and corresponding residue using the following relationships.

$$\Omega_k = |\lambda_k|, \quad \zeta_k = -\text{Re}(\lambda_k) / |\lambda_k| \quad (24)$$

$$A_{jk} = \lambda_k \Psi_{jk}^R \Psi_{Pk}^L \quad (25)$$

#### 2.4.1 Comment on the Use of AMI

For nonrotating (conservative) systems, AMI determines system eigenvalues and eigenvectors by fitting input FRF data to the relationship defined in Eq. 23. The key to getting accurate eigenvector information is the ability to either excite the system or measure system response at a number of points on the system. As discussed previously, access to the rotating shaft on installed equipment for data collection during normal operation is limited

to axial positions corresponding to bearing housings. The same limitation is placed on the analytical models of the prototypical system used in the present work. Consequently, few FRFs are available for processing by AMI. Past experience showed that although AMI's eigenvalue identification performance degraded somewhat as the number of available FRFs decreases, the algorithm identified eigenvalues with acceptable accuracy. However, the same was not true for eigenvectors. The low number of available FRFs resulted in an undersampled eigenvector estimation. Therefore, in the work presented here, AMI is used only to determine system eigenvalues. Eigenvectors are not considered.

Additionally, it is understood that the possibility of missing a mode increases as the number of measurement locations decreases. If a mode's contribution to an FRF is below the noise level, AMI is not able to detect it. The work presented here relies on the assumption that a given defect affects at least one mode that has a nonzero response at one or more of the measurement locations, and that some of these eigenvalues are sensitive to defects.



## CHAPTER III

### PROTOTYPICAL SYSTEM

#### *3.1 Introduction*

The majority of the analyses presented in this thesis are conducted on a specific rotordynamic system, consisting of a shaft, attached disk, and supporting bearings. Two mathematical models are used to represent this prototypical system. The first model, termed the simplified model, is taken directly from the literature [73]. The chapter opens with a summary of this model. The second model, termed the standard model, is a new version of the simplified model, modified to include a shaft crack. The development of the representation of the shaft crack is discussed in the following. Both models of the prototypical system incorporate the short-bearing approximation, and one section of the chapter is devoted to this subject. A representation of bearing wear, applicable to the bearings in both the simplified and standard models, is also developed. Additionally, the conversion between fixed coordinate system data and moving coordinate system data is discussed.

#### *3.2 System Parameters*

The prototypical system is a circular shaft, supported by plain journal bearings at its ends, with a transversely mounted disk. The system's circular steel shaft has a span between bearings of 1 meter and is 80 mm in diameter. The 45 kg disk is mounted 433 mm from Bearing 1. The disk has a polar moment of inertia  $I_{xx} = 0.298 \text{ kg}\cdot\text{m}^2$ , and a transverse moment of inertia  $I_{yy} = 0.245 \text{ kg}\cdot\text{m}^2$ . Identical journal bearings, with length to diameter ratio  $L_b/D_b = 1/4$ , nominal clearance ratio  $c_b/R_b = 1.25 \times 10^{-3}$ , and fluid viscosity  $\nu = 7 \times 10^{-3} \text{ N}\cdot\text{s}/\text{m}^2$ , support the shaft at each end. The system's first two critical speeds are 73 rad/s and 230 rad/s, respectively.

The system parameters were taken from [73] and used without modification. In both analytical models of the system, the connection of the disk to the shaft is modeled as a

point attachment. Although the polar and transverse moments of inertia suggest a thick disk, point attachment of the disk to the shaft could be accommodated through the use of a thin web.

### ***3.3 Brief Description of Models***

The simplified model of the prototypical system and the standard model of the prototypical system are both based on the system parameters described in the previous section. These linear models are used to reproduce physical phenomena, but they are not intended to be faithful to any specific system. The following statements apply to both models. Orthogonal shaft flexural displacements and the associated shaft cross-sectional rotations describe the system's response. The shaft and disk are perfectly aligned and balanced, and the disk is rigid. The deformation of the shaft is represented by Ritz series in conjunction with Timoshenko beam theory, generalized to include gyroscopic effects. (Both the transverse shear and the rotary inertia of the shaft are considered.) The disk's connection to the shaft is modeled as a point attachment. Plain hydrodynamic bearings (modeled with the short-bearing approximation) support the shaft.

The simplified model represents the prototypical system with an uncracked shaft. The simplified model uses one Ritz series, defined along the entire length of the shaft, to describe each response variable.

The standard model represents the prototypical system with a gaping (always open) shaft crack at midspan. Translational and torsional springs, representing the reduced shaft stiffness associated with the crack, join two undamaged shaft sections. Each response variable is described by two Ritz series, one for each undamaged shaft section. No continuity conditions for any response variable are specified across the crack. Crack damping is not considered.

The effects of bearing wear are investigated using both models. Wear of the plain hydrodynamic bearing is modeled as a symmetric increase in bearing inner diameter. Changes in lubricant temperature and viscosity due to increased clearance are assumed negligible.

### 3.4 *Simplified Model of Prototypical System (Uncracked Shaft)*

#### 3.4.1 Description

Zirkelback and Ginsberg originally presented this model [73]. The shaft and disk are perfectly aligned and balanced, and disk flexibility is considered negligible. The deformation of the shaft is represented by Ritz series in conjunction with Timoshenko beam theory, generalized to include gyroscopic effects. The disk's displacement and rotation are related to the motion of the shaft's cross-section at the attachment point. Vance [65] and Lee [38] presented the stiffness and damping coefficients of plain hydrodynamic bearings using the short-bearing approximation, and these are used as given.

The system is shown in Figure 1. The shaft executes general motion within a fixed reference frame  $XYZ$ . The  $x$ -axis of the moving reference frame  $Oxyz$  coincides with the deformed centroidal axis of the shaft, as shown in Figure 2. Shaft flexural displacements  $v$  and  $w$  are in the  $Y$  and  $Z$  directions. Rotations  $\alpha$  and  $\beta$  are the Eulerian angles relative to the  $Y$  and  $Z$  directions. The following vector of displacements and rotations is used

$$\{\eta\} = [v, \alpha, w, \beta]^T. \quad (26)$$

#### 3.4.2 Ritz Series Analysis

The shaft displacements and rotations are represented by the following Ritz series,

$$\begin{aligned} v &= \sum_{j=1}^N \psi_j^{(\text{disp})}(x) q_j^{(v)}(t), & w &= \sum_{j=1}^N \psi_j^{(\text{disp})}(x) q_j^{(w)}(t) \\ \alpha &= \sum_{j=1}^N \psi_j^{(\text{rot})}(x) q_j^{(\alpha)}(t), & \beta &= \sum_{j=1}^N \psi_j^{(\text{rot})}(x) q_j^{(\beta)}(t) \end{aligned} \quad (27)$$

Zirkelback and Ginsberg developed expressions for the kinetic and potential energies of the prototypical system, as well as an expression for the virtual work done by the bearings. (This virtual work incorporated the bearing effects through the use of the bearing stiffness and damping coefficients.) All energy and work relationships were written in terms of the shaft displacements and rotations. The Ritz series representations of  $v$ ,  $\alpha$ ,  $w$ , and  $\beta$  in Eq. 27 were substituted into the kinetic energy expression. The resulting quadratic sum contained system inertia matrix coefficients accounting for both displacement and rotation

effects. This quadratic sum also contained system gyroscopic matrix coefficients. Next, the Ritz series representations of the variables were substituted into the potential energy expression. The resulting quadratic sum provided the system stiffness matrix coefficients describing the shaft stiffness effects. Finally, the Ritz series were used to represent the displacements and rotations in the virtual work expression. The result was a set of generalized forces that depended linearly on the various Ritz series coefficients and their time derivatives. The elements of the system stiffness and damping matrices, related to bearing stiffness and damping, were taken from this. A detailed discussion of the Ritz series analysis of Zirkelback and Ginsberg's model is contained in [73].

The simplified model was dimensionless in the original definition, and the same nondimensionalization is retained in the present work. The shaft length  $L$  is the length scaling factor. Time is scaled by  $\tau = (\rho AL^4/EI)^{1/2}$ . Here,  $\rho$  is the density of the shaft material,  $A$  is shaft cross-sectional area,  $E$  is the shaft material modulus of elasticity, and  $I$  is the shaft area moment of inertia. The factor  $EI/L$  scales the energies. In the present work, the time scale is applied to frequency to give nondimensional frequency units. All frequency domain response data generated with the simplified and standard models of the prototypical system is plotted against nondimensional frequency units. In other words, if  $\Omega$  is a nondimensional frequency, the dimensional value is  $(EI/\rho AL^4)^{1/2}\Omega$ .

### 3.4.3 Equations of Motion

The inertial ( $XYZ$ ) equations of motion for a general axisymmetric rotor are given in Eq. 2. Applying these equations to the prototypical system operating in its nominal (undamaged) condition in the  $XYZ$  reference frame yields

$$[M] \{\ddot{q}\} + [[C_B(\Omega)] + [G](\Omega)] \{\dot{q}\} + [K_B(\Omega) + K_S] \{q\} = \{Q\}. \quad (28)$$

Here,  $[C_B]$  is the bearing damping matrix,  $[K_B]$  is the bearing stiffness matrix, and  $[K_S]$  is the shaft stiffness matrix. The bearing stiffness and damping matrices are nonsymmetric, due to the characteristics of the journal bearings and are functions of shaft speed,  $\Omega$ . The shaft is isotropic when the system is in the nominal condition, so the shaft stiffness is constant in the  $XYZ$  frame. The damping of the shaft material is negligible in the

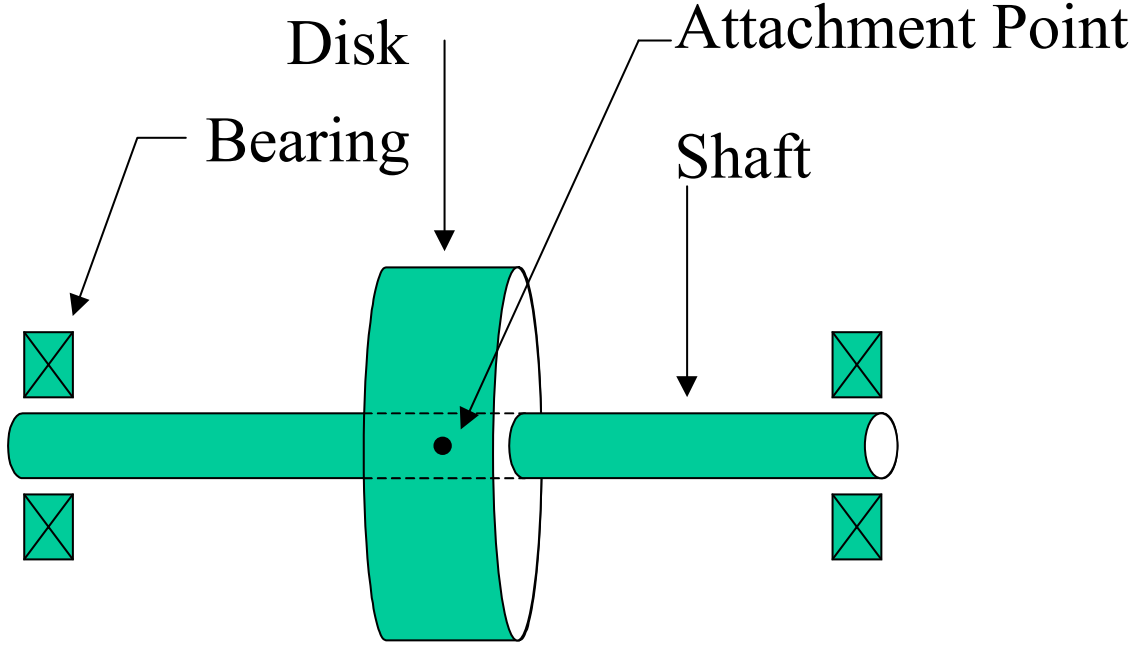


**Figure 1:** Prototypical System.

prototypical system, so there is no  $[C_S]$  matrix. When bearing wear is introduced, the form of the equations of motion remains unchanged, although elements of the  $[C_B]$  and  $[K_B]$  matrices assume different values.

#### 3.4.4 Model Use

Preliminary studies detailed in the next two chapters were conducted to evaluate the performance of a new version of AMI and to investigate new bearing wear detection methods. No crack was introduced to the prototypical system's shaft in those studies, which directly used the simplified model.

### 3.5 Use of Short-Bearing Model

The short-bearing approximation is used to calculate the coefficients for the plain journal bearings supporting the prototypical system. These well-known values are presented in many references. (See Appendix A.) In the short-bearing approximation, it is assumed that couples induced by cross-sectional rotation of the shaft in the bearing are negligible. Shaft

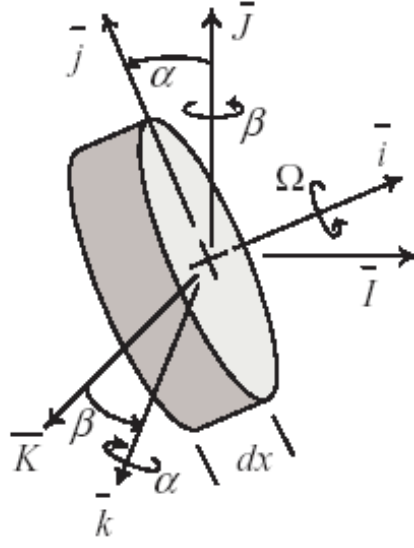


**Figure 2:** Relationships between axes and rotations for a differential shaft element.

cross-sectional rotations  $\alpha$  and  $\beta$  are two of the four response variables of the prototypical system.

An analysis was conducted to determine if the short-bearing approximation was appropriate for the present work. The short-bearing approximation provides the standard 8-coefficient bearing model, which relates transverse forces to translational displacements. For the displacement vector  $\{\eta\} = [v, \alpha, w, \beta]^T$ , the stiffness coefficients for the 8-coefficient bearing model are

$$K_8 = \begin{bmatrix} K_{VV} & 0 & K_{VW} & 0 \\ 0 & 0 & 0 & 0 \\ K_{WV} & 0 & K_{WW} & 0 \\ 0 & 0 & 0 & 0 \end{bmatrix}. \quad (29)$$

These coefficients, plus the four corresponding damping coefficients, lead to the term “8-coefficient model.” The 16-coefficient model provides the next level of detail. Kikuchi [35] used the short-bearing approximation to develop this model to simulate a flexible shaft supported by plain journal bearings. The model adds rotation-rotation effects to the

displacement-displacement effects in the 8-coefficient model. The stiffness coefficients are

$$K_{16} = \begin{bmatrix} K_{VV} & 0 & K_{VW} & 0 \\ 0 & K_{\alpha\alpha} & 0 & K_{\alpha\beta} \\ K_{WV} & 0 & K_{WW} & 0 \\ 0 & K_{\beta\alpha} & 0 & K_{\beta\beta} \end{bmatrix}. \quad (30)$$

Kikuchi analyzed a system over a range of decreasing bearing clearances. The results showed that using the 16-coefficient model produced a decrease in maximum whirl amplitude, compared with using the 8-coefficient model. (Note that the study addressed displacement of the disk mounted near midspan of the shaft, not shaft displacement in or near a bearing.) Although not stated explicitly, the reduction in amplitude is approximately 35% for a bearing with  $c_b/R_b = 1.0 \times 10^{-3}$ . The amplitude differences decreased as bearing clearance increased. No effects on resonant frequency, due to bearing model choice, were reported. The bearing used in Kikuchi's work had  $L_b/D_b = 0.6$ , as opposed to the  $L_b/D_b = 0.25$  bearings in the prototypical system.

Zachariadis [71] surveyed existing work on short bearings used to support flexible shafts in the introduction to his paper detailing the 32-coefficient model for a step bearing incorporating an annular ring. The 32-coefficient model included rotation-displacement and displacement-rotation effects, such that all terms in the stiffness and damping matrices were nonzero. Other than the Zachariadis study and papers by Jakeman [32], and San Andres [55], there are very few examples of 32-coefficient models in the literature. Zachariadis showed that critical speeds were influenced very little when evaluated with the 8-coefficient model, the 16-coefficient model, and the 32-coefficient model. Rao [51] stated that including rotation-rotation effects through the use of moment coefficients had a negligible effect on system properties. Subbiah [63] compared his 16-coefficient model of a finite bearing with Kikuchi's 16-coefficient model of a short bearing and the standard 8-coefficient model of a short bearing. Subbiah found less than 8% difference in critical speeds and concluded that the 8-coefficient model was a good approximation. He went on to state that "it is generally noted that the effects of rotational fluid film coefficients have very little influence on the response of simple rotor systems."

The prototypical system was analyzed in the frequency domain with the 8-coefficient short-bearing model and with the Kikuchi 16-coefficient short-bearing model coefficients at a shaft speed of 1.35 nondimensional frequency units. The eigenvalues in the frequency range of interest for the two cases are shown in Table 1. For the underdamped modes, the eigenvalues calculated with the 16-coefficient model and the corresponding eigenvalues calculated with the 8-coefficient model differed by less than 1%. The  $-0.16891 + i5.4845$  and  $-0.6070 + i33.1100$  modes dominated the system response. The eigenvectors of these two modes calculated with the 16-coefficient model both differed by less than 5% with the corresponding eigenvectors calculated from the 8-coefficient model. The relatively small change resulting from incorporating a bearing model more complex than the 8-coefficient short-bearing model does not justify the time required to implement such a model.

**Table 1:** Comparison of prototypical system eigenvalues for the 8-coefficient and 16-coefficient short bearing models.

	16-coefficient Model		8-coefficient Model	
Mode	$\text{Re}(\lambda)$	$\text{Im}(\lambda)$	$\text{Re}(\lambda)$	$\text{Im}(\lambda)$
overdamped	-218.1	2.45E-13	-218.12	5.86E-13
overdamped	-3148.6	1.19E-11	-3572	4.86E-12
1	-1.4226	1.1098	-1.4225	1.1097
2	-1.4755	1.2591	-1.4755	1.2591
3	-1.186	5.0535	-1.1856	5.0518
4	-0.16891	5.4845	-0.11025	5.4871
5	-0.60696	33.11	-0.46183	33.114
6	-4.5651	33.689	-4.5685	33.686
7	-1.1952	65.656	-0.8387	65.68
8	-8.3431	67.89	-8.3494	67.882
9	-1.6203	110.03	-1.2695	110.04
10	-11.866	114.48	-11.874	114.48

### 3.6 Bearing Wear Description

Hydrodynamic bearing wear is modeled with a symmetric increase in the bearing inner diameter, in the same manner as Wu [69], Redmond [52], and Muszynska [45]. The states of bearing wear analyzed are within the *BCR* guidelines given by Shigley [62]. The methods used by Hashimoto [28], [29] and Scharrer [59], which incorporate the asymmetric nature of



bearing wear, are more accurate, but add a level of complexity not required in this study. (The referenced methods are discussed in Section 2 of Chapter *II*.) Modeling bearing wear as a symmetric increase in the inner diameter leads to changes in bearing properties that approximate (in magnitude and sign) the property changes calculated with the more complex, non-symmetric models. The present work focuses on the use of AMI in a new application: detection of defects in rotating equipment. An elementary bearing wear model, proven to provide a reasonable simulation of the phenomenon, is sufficient for this proof of concept testing.

### ***3.7 Conversion Between Fixed And Moving Coordinate Systems***

The overwhelming majority of sensors used to monitor installed industrial or aerospace rotating equipment for changes in vibration signature are either permanently or temporarily mounted on a nonrotating part, and return displacement, velocity, or acceleration data relative to the fixed *XYZ* coordinate system. Consequently, the time domain response data generated by the mathematical models of the prototypical system in the present work are also expressed in the fixed coordinate system. As discussed previously, the fixed *XYZ* coordinate system is appropriate for the detection of bearing defects, but the moving *xyz* coordinate system has benefits in the detection of shaft cracks [23], [26], and [34]. Converting response data from the fixed reference frame to the moving reference frame is done by a coordinate transformation,

$$\begin{Bmatrix} v_{moving} \\ w_{moving} \end{Bmatrix} = \begin{bmatrix} \cos(\Omega t) & \sin(\Omega t) \\ -\sin(\Omega t) & \cos(\Omega t) \end{bmatrix} \begin{Bmatrix} v_{fixed} \\ w_{fixed} \end{Bmatrix} \quad (31)$$

where,  $\Omega$  is the shaft speed. A similar transformation applies to the Eulerian angles describing the cross-sectional rotations.

The frequency domain responses of a simple system in the fixed and moving coordinate systems are compared to develop an understanding of the effects of converting to the moving coordinate system. A rigid rotor supported by identical isotropic bearings, presented in [38], is used in this simple analysis. The model, defined in the fixed *XYZ* coordinate

system, is solved in the time domain at constant speed. The moving coordinate system frequency response at that rotation rate is calculated from the fixed coordinate data, and the two data sets are compared visually. (Note that this rigid rotor model is completely described in Chapter IV, where it is used in a detailed study comparing the FRF and the dFRF.)

The system model has four response variables, and the behavior of each variable, with respect to the conversion from the fixed coordinate system to the moving coordinate system, is similar. The relationship between the frequencies at resonant peaks for both the FRF and dFRF data formats is shown in Table 2.

For the FRF data format, a single peak in the fixed coordinate system frequency response plot produces two peaks in the moving coordinate system frequency response plot. Assume  $v_{fixed}$  and  $w_{fixed}$  in Eq. 31 are harmonic at frequency  $\omega$ , and express them in complex exponential notation.

$$\begin{aligned} v_{fixed} &= \frac{1}{2} (Ae^{i\omega t} + A^*e^{-i\omega t}) \\ w_{fixed} &= \frac{1}{2} (Be^{i\omega t} + B^*e^{-i\omega t}) \end{aligned} \quad (32)$$

Here,  $A$  and  $B$  are amplitudes, and the  $*$  represents complex conjugate. The corresponding representations of  $\cos(\Omega t)$  and  $\sin(\Omega t)$  are

$$\begin{aligned} \cos(\Omega t) &= \frac{1}{2} (e^{i\Omega t} + e^{-i\Omega t}) \\ \sin(\Omega t) &= \frac{1}{2i} (e^{i\Omega t} - e^{-i\Omega t}) \end{aligned} \quad (33)$$

Substitute  $v_{fixed}$  and  $w_{fixed}$  in Eq. 32 and  $\cos(\Omega t)$  and  $\sin(\Omega t)$  in Eq. 33 into Eq. 31. The characteristics of  $v_{moving}$  and  $w_{moving}$  are similar, so only one will be presented. The resulting expression for  $v_{moving}$  is

$$\begin{aligned} v_{moving} &= \frac{1}{4} [(e^{i\Omega t} + e^{-i\Omega t}) (Ae^{i\omega t} + A^*e^{-i\omega t}) + \\ &\quad \frac{1}{i} (e^{i\Omega t} - e^{-i\Omega t}) (Be^{i\omega t} + B^*e^{-i\omega t})] \end{aligned} \quad (34)$$

Perform the multiplication and combine like terms. The simplified expression for  $v_{moving}$  is

$$v_{moving} = \frac{1}{2} \left( (A - iB)e^{i(\Omega+\omega)t} + (A + iB)e^{i(-\Omega+\omega)t} \right) \quad (35)$$

The complex exponents describe how the frequencies of the two new moving coordinate system peaks are related to the frequency of the original fixed coordinate system peak,  $\omega_i$ ,

and the shaft speed,  $\Omega$ . The results of processing the data obtained from the rigid rotor model agreed with Eq. 35.

Lee and Joh developed the corresponding theory for the dFRF in [34]. For both the normal dFRF and the reverse dFRF, the same number of peaks is present in response data for both coordinate systems, but the frequency of the new moving coordinate system data peak is shifted from the frequency of the original fixed coordinate system data peak by shaft speed, as shown in Table 2. The results of the analysis using the rigid rotor model agreed with the theory published in [34] for both types of dFRFs.

**Table 2:** Frequency domain comparison: effects of converting FRF and dFRF data from fixed to moving coordinate system.

Coordinate System	Approximate Frequency for Peak
<i>FRF</i> (eg. $H_{ZZ}$ )	
Fixed	$\omega_i$
Moving	$ \Omega - \omega_i $ and $\Omega + \omega_i$
<i>Normal dFRF</i> ( $H_{PG}$ )	
Fixed	$\omega_i$
Moving	$\omega_i - \Omega$
<i>Reverse dFRF</i> ( $H_{PG}$ )	
Fixed	$\omega_i$
Moving	$\omega_i + \Omega$

### 3.8 Standard Model of Prototypical System (Cracked Shaft)

The simplified model of the prototypical system is the starting point in the development of the standard model. The shaft and disk are still assumed to be perfectly aligned and balanced, and disk flexibility is again ignored. The simplified model's method of nondimensionalization is used. Orthogonal shaft flexural displacements and the associated cross-sectional rotations are again used as response variables.

#### 3.8.1 Type of Crack Model

The gaping crack model is used to account for the decreased shaft stiffness due to a crack. The incremental increased faithfulness of the analytical response data that would result from inclusion of the crack breathing phenomenon is not warranted for this proof of concept

analysis. Furthermore, modal analysis of nonlinear systems can be problematic. It has been shown that a gaping crack model produces acceptably accurate results while requiring considerably less computational effort than a breathing crack model [26].

### 3.8.2 Modification of Shaft Model

The reduced stiffness associated with a gaping crack is modeled in the same manner as Wauer [67]. The shaft is considered to be made up of two undamaged shaft sections joined by translational and torsional springs, representing the crack. Each displacement variable is described by two Ritz series, one for each undamaged section, and no continuity conditions for either the flexural displacement variables ( $v$  and  $w$ ) or the rotational variables ( $\alpha$  and  $\beta$ ) are defined across the crack. The superscripts  $r$  and  $l$  are used to denote which shaft section a response variable describes. The “left” section runs from Bearing 1, past the disk, to the crack. The “right” section runs from the crack to Bearing 2. Bearing 1 is the only bearing in which wear occurs.

The potential energy expression (in nondimensional form) for the two undamaged sections of the shaft has the same form as the strain energy used in the simplified model [73].

$$V_k = \frac{1}{2} \int_0^1 \left\{ \left( \frac{\partial \alpha}{\partial s} \right)^2 + \left( \frac{\partial \beta}{\partial s} \right)^2 + \kappa' \left[ \left( \frac{\partial v}{\partial s} - \alpha \right)^2 + \left( \frac{\partial w}{\partial s} + \beta \right)^2 \right] \right\} ds \quad (36)$$

The kinetic energy expression from the simplified model is also used. (Note that only the left segment of the shaft has an attached disk.) The following response vectors (in the fixed  $XYZ$  coordinate system) are used in the development of the standard model of the prototypical system.

$$\begin{aligned} \{\eta^l\} &= [v^l, \alpha^l, w^l, \beta^l]^T \\ \{\eta^r\} &= [v^r, \alpha^r, w^r, \beta^r]^T \end{aligned} \quad (37)$$

The flexural displacement and rotational variables contained in the vectors  $\{\eta^l\}$  and  $\{\eta^r\}$  describe the response of the left and right shaft sections. Unsubscripted response variables shall correspond to the fixed coordinate system. Taking into account the left and right sections of the shaft, the complete response vector becomes

$$\{\eta\} = \left[ \{\eta^l\}, \{\eta^r\} \right]^T = [v^l, \alpha^l, w^l, \beta^l, v^r, \alpha^r, w^r, \beta^r]^T \quad (38)$$

To simplify notation in the development of the crack model,  $\{\eta_C\}$ , the difference of the left response vector and the right response vector, both evaluated at the location of the shaft crack, is defined.

$$\{\eta_C\} = \left[ \{\eta^l\}|_{x=crack} - \{\eta^r\}|_{x=crack} \right] \quad (39)$$

Following Wauer, the potential energy expression for the cracked section, in the moving  $xyz$  coordinate, system is

$$(V_{crack}) = \frac{1}{2} \{\eta_C\}_m^T [K_{crack,moving}] \{\eta_C\}_m \quad (40)$$

Here  $[K_{crack,moving}]$  is a symmetric  $4 \times 4$  stiffness matrix incorporating the reduction in shaft stiffness due to the presence of the crack, and the  $m$  subscript on  $\{\eta_C\}$  denotes the moving coordinate system. (In the remainder of the discussion,  $[K_{crack}]$  is the fixed coordinate system representation of the matrix and  $[K_{crack,moving}]$  is the moving coordinate system representation.)

Wauer defined the form of the  $[K_{crack,moving}]$  matrix in [67]. Papadopoulos and Dimarogonas [49] originally developed a  $6 \times 6$  compliance matrix for a cracked shaft by including axial displacement and torsion in addition to  $v_m$ ,  $\alpha_m$ ,  $w_m$ , and  $\beta_m$ . Wauer only considered the four variables used in the present analysis. Furthermore, Wauer assumed that the crack edge was parallel to the  $\bar{k}$  axis in Fig 2. The symmetry associated with this assumption decouples the bending described by  $v_m$  and  $\alpha_m$  from the bending described by  $w_m$  and  $\beta_m$  [67] and [27]. The resulting form of the matrix is

$$K_{crack,moving} = \begin{bmatrix} K_{22} & 0 & 0 & 0 \\ 0 & K_{44} & 0 & 0 \\ 0 & 0 & K_{33} & 0 \\ 0 & 0 & 0 & K_{55} \end{bmatrix}. \quad (41)$$

The elements of this matrix (in the form of dimensionless compliance) were reported by Papadopoulos and Dimarogonas [49]. The subscripts in Eq. 41 follow the convention defined in [49]. The potential energy expression for the crack is used to derive the expression for  $[K_{crack}]$ . For the  $\{\eta_C\}$  vector in Eq. 39, the inverse form of Eq. 31 is

$$\{\eta_C\} = \begin{bmatrix} \cos(\Omega t) & 0 & -\sin(\Omega t) & 0 \\ 0 & \cos(\Omega t) & 0 & -\sin(\Omega t) \\ \sin(\Omega t) & 0 & \cos(\Omega t) & 0 \\ 0 & \sin(\Omega t) & 0 & \cos(\Omega t) \end{bmatrix} \{\eta_C\}_m. \quad (42)$$

Defining the matrix  $[R]$  as

$$[R] = \begin{bmatrix} \cos(\Omega t) & 0 & -\sin(\Omega t) & 0 \\ 0 & \cos(\Omega t) & 0 & -\sin(\Omega t) \\ \sin(\Omega t) & 0 & \cos(\Omega t) & 0 \\ 0 & \sin(\Omega t) & 0 & \cos(\Omega t) \end{bmatrix} \quad (43)$$

simplifies Eq. 42 to

$$\{\eta_C\} = [R] \{\eta_C\}_m. \quad (44)$$

The expression for the moving coordinate system vector is

$$\{\eta_C\}_m = [R]^T \{\eta_C\}. \quad (45)$$

Substituting the right side of Eq. 45 in for  $\{\eta_C\}_m$  in Eq. 40 gives another form of the crack potential energy expression.

$$(V_{crack}) = \frac{1}{2} \left\{ [R]^T \{\eta_C\} \right\}^T [K_{crack,moving}] \left\{ [R]^T \{\eta_C\} \right\}. \quad (46)$$

Expanding this equation leads to the fixed coordinate system expression for  $V_{crack}$ ,

$$(V_{crack}) = \frac{1}{2} \{\eta_C\}^T [K_{crack}] \{\eta_C\}. \quad (47)$$

Here,  $[K_{crack}]$  is the product of  $[R]$ ,  $[K_{crack,moving}]$ , and the transpose of  $[R]$ .

$$[K_{crack}] = [R] [K_{crack,moving}] [R]^T \quad (48)$$

The  $[K_{crack}]$  matrix is calculated by substituting the expressions for  $[R]$  (Eq. 43) and  $[K_{crack,moving}]$  (Eq. 41) into Eq. 48. The form of  $[K_{crack}]$  is

$$K_{crack} = \begin{bmatrix} a & 0 & b & 0 \\ 0 & c & 0 & d \\ b & 0 & f & 0 \\ 0 & d & 0 & h \end{bmatrix}, \quad (49)$$

and the elements of the matrix are

$$\begin{aligned} a &= K_{22} \cos^2(\Omega t) + K_{33} \sin^2(\Omega t) \\ b &= K_{22} \cos(\Omega t) \sin(\Omega t) - K_{33} \cos(\Omega t) \sin(\Omega t) \\ c &= K_{44} \cos^2(\Omega t) + K_{55} \sin^2(\Omega t) \\ d &= K_{44} \cos(\Omega t) \sin(\Omega t) - K_{55} \cos(\Omega t) \sin(\Omega t) \\ f &= K_{22} \cos^2(\Omega t) + K_{33} \sin^2(\Omega t) \\ h &= K_{44} \sin^2(\Omega t) + K_{55} \cos^2(\Omega t). \end{aligned} \quad (50)$$

With respect to the fixed  $XYZ$  coordinate system, the stiffness of a cracked, rotating shaft is a function of time. If the moving  $xyz$  coordinate system is chosen for use, the shaft stiffness is time-invariant. When there are no other factors to consider, it is preferable to model a cracked shaft system in the moving coordinate system to simplify the analysis. The bearings of the prototypical system have stiffness and damping that is time-invariant with respect to the fixed coordinate system. Therefore, the standard model (cracked shaft) of the prototypical system is time-varying in both coordinate systems. To align the research with current industrial and aerospace vibration sensor technology, and to make use of an existing system model, the crack model is developed for use in the  $XYZ$  coordinate system. The time-varying nature of the standard model of the prototypical system is fully addressed in Section 1 of Chapter *II*.

### 3.8.3 Ritz Series Analysis

Ritz series analysis is conducted to calculate the elements of the  $[K_C]$  matrix, which describes the effect of the shaft crack on the overall system stiffness matrix,  $[K]$ . A Ritz series expansion consists of a sum of products of time-dependent generalized coordinates  $q_j$  and kinematically admissible basis functions  $\psi_j$ . The orthogonal displacement fields  $(v, w)$  and

the rotation angles  $(\alpha, \beta)$  of the differential shaft element are described individually by Ritz series expansions of the form

$$\begin{aligned} v^l &= \sum_{j=1}^N \psi_j^{(\text{disp}^l)} \left( \frac{x}{L_l} \right) q_j^{(v^l)}(t), \quad w^l = \sum_{j=1}^N \psi_j^{(\text{disp}^l)} \left( \frac{x}{L_l} \right) q_j^{(w^l)}(t) \\ \alpha^l &= \sum_{j=1}^N \psi_j^{(\text{rot}^l)} \left( \frac{x}{L_l} \right) q_j^{(\alpha^l)}(t), \quad \beta^l = \sum_{j=1}^N \psi_j^{(\text{rot}^l)} \left( \frac{x}{L_l} \right) q_j^{(\beta^l)}(t). \end{aligned} \quad (51)$$

Basis functions associated with a free-free beam are employed because there are no geometric boundary conditions to satisfy for hydrodynamic bearings. These forms describe the segment to the left of the crack. Replacing each  $l$  with an  $r$  generates the similar forms that apply to the segment to the right of the crack. The series for each variable is taken to be the same length  $N$  as a matter of convenience.

The left and right segment response vectors (Eq. 37) and the fixed coordinate system form of  $[K_{crack}]$  (Eq. 49) are substituted into the potential energy expression for the cracked section (Eq. 40). Expansion of the resulting equation leads to

$$\begin{aligned} V_{crack} = & \frac{1}{2} \left[ a \left( (v^l)^2 - 2v^r v^l + (v^r)^2 \right) + b \left( w^l v^l - w^l v^r - w^r v^l + w^r v^r \right) \right. \\ & + c \left( (\alpha^l)^2 - 2\alpha^r \alpha^l + (\alpha^r)^2 \right) + d \left( \beta^l \alpha^l - \beta^l \alpha^r - \beta^r \alpha^l + \beta^r \alpha^r \right) \\ & + f \left( (w^l)^2 - 2w^r w^l + (w^r)^2 \right) + b \left( w^l v^l - w^l v^r - w^r v^l + w^r v^r \right) \\ & \left. + h \left( (\beta^l)^2 - 2\beta^r \beta^l + (\beta^r)^2 \right) + d \left( \beta^l \alpha^l - \beta^l \alpha^r - \beta^r \alpha^l + \beta^r \alpha^r \right) \right] \end{aligned} \quad (52)$$

The Ritz series representations of the response variables (the left segment forms are shown in Eq. 51) are then substituted into Eq. 52.

$$\begin{aligned} V_{crack} = & \frac{1}{2} a \left[ \left( \sum_{j=1}^N \psi_j^{(\text{disp}^l)} q_j^{(v^l)} \right) \left( \sum_{n=1}^N \psi_n^{(\text{disp}^l)} q_n^{(v^l)} \right) - 2 \sum_{j=1}^N \psi_j^{(\text{disp}^r)} q_j^{(v^r)} \sum_{n=1}^N \psi_n^{(\text{disp}^l)} q_n^{(v^l)} \right. \\ & \left. + \left( \sum_{j=1}^N \psi_j^{(\text{disp}^r)} q_j^{(v^r)} \right) \left( \sum_{n=1}^N \psi_n^{(\text{disp}^r)} q_n^{(v^r)} \right) \right] \\ & + \frac{1}{2} b \left[ \sum_{j=1}^N \psi_j^{(\text{disp}^l)} q_j^{(w^l)} \sum_{n=1}^N \psi_n^{(\text{disp}^l)} q_n^{(v^l)} - \sum_{j=1}^N \psi_j^{(\text{disp}^l)} q_j^{(w^l)} \sum_{n=1}^N \psi_n^{(\text{disp}^r)} q_n^{(v^r)} \right. \\ & \left. - \sum_{j=1}^N \psi_j^{(\text{disp}^r)} q_j^{(w^r)} \sum_{n=1}^N \psi_n^{(\text{disp}^l)} q_n^{(v^l)} + \sum_{j=1}^N \psi_j^{(\text{disp}^r)} q_j^{(w^r)} \sum_{n=1}^N \psi_n^{(\text{disp}^r)} q_n^{(v^r)} \right] + \dots \end{aligned} \quad (53)$$

Due to the number of terms in the full expansion, only the first line of Eq. 52 (the  $a$  and  $b$  terms) is shown in Eq. 53. The expansions of the other three lines in Eq. 52 (the  $c$  and



$d$  terms, the  $f$  and  $b$  terms, and the  $h$  and  $d$  terms) follow the same form. Only the  $a$  and  $b$  terms will be shown explicitly in the intermediate portion of the development. In order to facilitate presentation, the  $(x/L_l)$  notation, indicating that the basis function is a function of space, and the  $(t)$  notation, indicating that the generalized coordinate is a function of time, are not shown in this and subsequent equations in this section. Expanding the squared terms in Eq. 53 and bringing the summations outside the expression yields

$$V_{crack} = \frac{1}{2} \sum_{j=1}^N \sum_{n=1}^N \left\{ \begin{aligned} & a \left[ \psi_j^{(\text{disp}^l)} \psi_n^{(\text{disp}^l)} q_j^{(v^l)} q_n^{(v^l)} - 2\psi_j^{(\text{disp}^r)} \psi_n^{(\text{disp}^l)} q_j^{(v^r)} q_n^{(v^l)} \right. \\ & \quad \left. + \psi_j^{(\text{disp}^r)} \psi_n^{(\text{disp}^r)} q_j^{(v^r)} q_n^{(v^r)} \right] \\ & + b \left[ \psi_j^{(\text{disp}^l)} \psi_n^{(\text{disp}^l)} q_j^{(w^l)} q_n^{(v^l)} - \psi_j^{(\text{disp}^l)} \psi_n^{(\text{disp}^r)} q_j^{(w^l)} q_n^{(v^r)} \right. \\ & \quad \left. - \psi_j^{(\text{disp}^r)} \psi_n^{(\text{disp}^l)} q_j^{(w^r)} q_n^{(v^l)} + \psi_j^{(\text{disp}^r)} \psi_n^{(\text{disp}^r)} q_j^{(w^r)} q_n^{(v^r)} \right] \end{aligned} \right\} \quad (54)$$

The general definition for potential energy in the Ritz formulation [23] is

$$V = \frac{1}{2} \sum_{j=1}^N \sum_{n=1}^N K_{jn} q_j q_n. \quad (55)$$

Equation 54 and the similarly expanded third line of Eq. 52 ( $f$  and  $b$  terms) are combined. To identify the stiffness coefficients in the  $K_C$  matrix, the terms in this combined quadratic sum are individually set equal to the right hand side of Eq. 55, with the appropriate generalized coordinates in place. For example,

$$\frac{1}{2} \sum_{j=1}^N \sum_{n=1}^N K_{Cjn} q_j^{(v^l)} q_n^{(v^l)} = \frac{1}{2} a \sum_{j=1}^N \sum_{n=1}^N \psi_j^{(\text{disp}^l)} \psi_n^{(\text{disp}^l)} q_j^{(v^l)} q_n^{(v^l)} \quad (56)$$

results in the definition of the stiffness coefficient for the  $v$  displacement in the left segment of the shaft,

$$K_{Cjn}^{(v^l v^l)} = a \psi_j^{(\text{disp}^l)} \psi_n^{(\text{disp}^l)}. \quad (57)$$

This is repeated to account for the contributions of all displacements. The second ( $c$  and  $d$ ) and fourth ( $h$  and  $d$ ) lines of Eq. 52 are also expanded and combined, and the rotational

stiffness coefficients in the  $K_C$  matrix are determined in the manner previously described.

$$\begin{aligned}
\begin{bmatrix} K_{Cjn}^{(v^l v^l)} \end{bmatrix} &= a \psi_j^{(\text{disp}^l)} \psi_n^{(\text{disp}^l)} \\
\begin{bmatrix} K_{Cjn}^{(w^l w^l)} \end{bmatrix} &= f \psi_j^{(\text{disp}^l)} \psi_n^{(\text{disp}^l)} \\
\begin{bmatrix} K_{Cjn}^{(\alpha^l \alpha^l)} \end{bmatrix} &= c \psi_j^{(\text{rot}^l)} \psi_n^{(\text{rot}^l)} \\
\begin{bmatrix} K_{Cjn}^{(\beta^l \beta^l)} \end{bmatrix} &= h \psi_j^{(\text{rot}^l)} \psi_n^{(\text{rot}^l)} \\
\begin{bmatrix} K_{Cjn}^{(w^l v^l)} \end{bmatrix} &= b \psi_j^{(\text{disp}^l)} \psi_n^{(\text{disp}^l)} \\
\begin{bmatrix} K_{Cjn}^{(\beta^l \alpha^l)} \end{bmatrix} &= d \psi_j^{(\text{rot}^l)} \psi_n^{(\text{rot}^l)} \\
\begin{bmatrix} K_{Cjn}^{(v^l v^r)} \end{bmatrix} &= -a \psi_j^{(\text{disp}^l)} \psi_n^{(\text{disp}^r)} \\
\begin{bmatrix} K_{Cjn}^{(w^l w^r)} \end{bmatrix} &= -f \psi_j^{(\text{disp}^l)} \psi_n^{(\text{disp}^r)} \\
\begin{bmatrix} K_{Cjn}^{(\alpha^l \alpha^r)} \end{bmatrix} &= -c \psi_j^{(\text{rot}^l)} \psi_n^{(\text{rot}^r)} \\
\begin{bmatrix} K_{Cjn}^{(\beta^l \beta^r)} \end{bmatrix} &= -h \psi_j^{(\text{rot}^l)} \psi_n^{(\text{rot}^r)} \\
\begin{bmatrix} K_{Cjn}^{(w^r v^l)} \end{bmatrix} &= -b \psi_j^{(\text{disp}^r)} \psi_n^{(\text{disp}^l)} \\
\begin{bmatrix} K_{Cjn}^{(\beta^r \alpha^l)} \end{bmatrix} &= -d \psi_j^{(\text{rot}^r)} \psi_n^{(\text{rot}^l)}
\end{aligned} \tag{58}$$

(Coefficients  $a$ ,  $b$ ,  $c$ ,  $d$ ,  $f$ , and  $h$  are defined in Eq. 50.) The terms for the right section can be obtained by replacing  $l$  with  $r$  in the first six equations. Regarding the basis functions, the most general form of the equations would have two translational basis functions,  $\psi_j^{(v)}$  and  $\psi_j^{(w)}$ , and two rotational basis functions,  $\psi_j^{(\alpha)}$  and  $\psi_j^{(\beta)}$ . However,  $\psi_j^{(v)} = \psi_j^{(w)}$  and  $\psi_j^{(\alpha)} = \psi_j^{(\beta)}$  for the present work, so one translational basis function,  $\psi_j^{(\text{disp})}$ , and one rotational basis function,  $\psi_j^{(\text{rot})}$ , are used.

The resulting general form of the  $[K_C]$  matrix is

$$K_C = \begin{bmatrix} [K_{cl}] & [K_{clr}] \\ [K_{clr}]^T & [K_{cr}] \end{bmatrix}, \tag{59}$$

where  $[K_{cl}]$  represents stiffness associated with the left section,  $[K_{cr}]$  represents the right section, and  $[K_{clr}]$  accounts for coupling effects.

### 3.8.4 Equations of Motion

The introduction of a shaft crack changes the form of the equations shown for the simplified model in Eq. 28. In the  $XYZ$  frame, the equations of motion of the prototypical system with a cracked shaft are

$$[M] \{\ddot{q}\} + [[C_B(\Omega)] + [G(\Omega)]] \{\dot{q}\} + [K(\Omega, t)] \{q\} = \{Q\}. \quad (60)$$

The stiffness matrix is written as

$$[K(\Omega, t)] = [[K_S] + [K_B(\Omega)] + [K_C(t)]] . \quad (61)$$

The  $S$ ,  $B$ , and  $C$  subscripts denote shaft, bearings, and crack, respectively. Consistent with the definition of the response vector in Eq. 38, the vector of generalized coordinates is defined in terms of subvectors to be

$$\{q\} = \left[ \left\{ q^{(v^l)} \right\}^T \left\{ q^{(\alpha^l)} \right\}^T \left\{ q^{(w^l)} \right\}^T \left\{ q^{(\beta^l)} \right\}^T \left\{ q^{(v^r)} \right\}^T \left\{ q^{(\alpha^r)} \right\}^T \left\{ q^{(w^r)} \right\}^T \left\{ q^{(\beta^r)} \right\}^T \right]^T . \quad (62)$$

The  $[K_{cl}]$  and  $[K_{clr}]$  submatrices in Eq. 59 can be written as

$$K_{cl} = \begin{bmatrix} [K_C^{(v^l v^l)}] & [0] & [K_C^{(w^l v^l)}]^T & [0] \\ [0] & [K_C^{(\alpha^l \alpha^l)}] & [0] & [K_C^{(\beta^l \alpha^l)}]^T \\ [K_C^{(w^l v^l)}] & [0] & [K_C^{(w^l w^l)}] & [0] \\ [0] & [K_C^{(\beta^l \alpha^l)}] & [0] & [K_C^{(\beta^l \beta^l)}] \end{bmatrix} \quad (63)$$

$$K_{clr} = \begin{bmatrix} [K_C^{(v^l v^r)}] & [0] & [K_C^{(v^l w^r)}] & [0] \\ [0] & [K_C^{(\alpha^l \alpha^r)}] & [0] & [K_C^{(\alpha^l \beta^r)}] \\ [K_C^{(v^l w^r)}]^T & [0] & [K_C^{(w^l w^r)}] & [0] \\ [0] & [K_C^{(\alpha^l \beta^r)}]^T & [0] & [K_C^{(\beta^l \beta^r)}] \end{bmatrix} \quad (64)$$

The expression for  $[K_{cr}]$  is obtained by substituting an  $r$  for each  $l$  in Eq. 63. Substituting the stiffness coefficients in Eq. 58 into these expressions for  $[K_{cl}]$ ,  $[K_{cr}]$ , and  $[K_{clr}]$  fully defines the  $8N \times 8N$   $[K_C]$  matrix in Eq. 59.

The submatrices making up the inertia, gyroscopic, and damping matrices in the equations of motion (Eq. 60) are calculated using the same logic used in the development of the

simplified model. Based on the defined vector of generalized coordinates, these matrices are  $8N \times 8N$  in the standard model of the prototypical system, instead of  $4N \times 4N$ , as in the simplified model. The inertia matrix is used to illustrate the general process. The inertia matrix for the standard model can be written

$$[M] = \begin{bmatrix} [M^l] & [0] \\ [0] & [M^r] \end{bmatrix} \quad (65)$$

Here, the  $[M^l]$  submatrix is a  $4N \times 4N$  matrix representing the left shaft segment, and the  $[M^r]$  submatrix is another  $4N \times 4N$  matrix for the right shaft segment. The elements of the  $[M^l]$  and  $[M^r]$  come from a Ritz series analysis of the form discussed in the section on the simplified model and in [73]. The  $[M^l]$  submatrix is

$$[M^l] = \begin{bmatrix} [M^{(v^l v^l)}] & [0] & [0] & [0] \\ [0] & [M^{(\alpha^l \alpha^l)}] & [0] & [0] \\ [0] & [0] & [M^{(w^l w^l)}] & [0] \\ [0] & [0] & [0] & [M^{(\beta^l \beta^l)}] \end{bmatrix} \quad (66)$$

### 3.8.5 Crack Damping

Initially the crack model was to incorporate damping effects, as well as stiffness effects. The relatively sparse coverage of the subject in published literature suggested this might be a significant, yet overlooked, effect. In combination with AMI's demonstrated ability to accurately detect changes in the real part of the eigenvalue for non-rotating structures, exploration of the idea seemed appealing. Wauer's [67] method of representing the crack's damping through the use of proportional damping was employed. In this method, the crack damping matrix,  $[C_{crack}]$ , is calculated as follows (see Eq. 49).

$$[C_{crack}] = d_i [K_{crack}] \quad (67)$$

While there are other acceptable methods to determine the proportionality constant, Wauer set  $d_i$  equal to the loss factor of the shaft material. The application of the  $[C_{crack}]$  matrix to the model of the prototypical system involves the results of the Ritz series analysis described above. Using the scale factors required by the model's nondimensionalization

and the proper  $d_i$  for the shaft material, a  $[C_C]$  matrix of the form of the  $[K_C]$  matrix (Eq. 59) is calculated. The overall system damping matrix incorporates the damping of the bearings and the crack

$$[C] = [C_B] + [C_C] \quad (68)$$

The form of the  $[C_C]$  matrix led to numerical difficulties for the integrators of the MATLAB ODE Suite. (See Section 6.5 of Chapter VI for a more detailed description of the solution method.) Increases in the time required for computation of at least a factor of 100 were seen. Several integrators in the ODE Suite were used in trials, and testing was conducted to find the optimum values of many of the internal parameters governing integrator performance. No measure appreciably sped up the integration. To identify the source of the difficulty, all nonzero elements of the crack damping matrix were set to a value of  $10^{-10}$ , yet no decrease in required processing time was evident. It was concluded that the form of the crack damping matrix, not the magnitude of its elements, was the source of the problem. Due to the number of system responses required for the crack detection study, it was decided that it would not be feasible to include the effects of crack damping and complete this project in a timely manner. Therefore, the effects of crack damping are not included in the response of any system configuration involving a shaft crack. This follows the majority of the works cited in the shaft crack modeling literature review.

### **3.8.6 Model Use**

The studies described in Chapters VI and VII were conducted to investigate a new shaft crack detection method. In these studies, the prototypical system was operated in the cracked configuration, and the standard model of the prototypical system was used in each case. The standard model is suitable for the time domain solutions employed in these studies.

## CHAPTER IV

# EVALUATION OF THE DIRECTIONAL FREQUENCY RESPONSE FUNCTION (DFRF)

### *4.1 Introduction*

In the course of its development, AMI had been applied to identify the modes of systems whose generalized coordinates are measured relative to a static equilibrium position. The conjugate-even property of the FRFs for such systems made it possible to fit simultaneously a pole and its complex conjugate to the data at each stage where an SDOF estimate was sought. Thus, the standard version of AMI could be applied to the normal FRFs of rotordynamic system, but not the dFRFs.

This chapter opens with a description of the conversion of standard AMI into Two-Sided AMI, which can process dFRFs. Three analyses are then conducted to verify the performance of the new algorithm. First, response data from a simple isotropic rigid rotor system is processed. Second, anisotropy is introduced into the rigid rotor system, and the analysis is repeated. Finally, response data of the simplified model of the prototypical system (in nominal condition) is processed. In addition to demonstrating that Two-Sided AMI functions properly, the studies of the rigid anisotropic system and the prototypical system explore the effects of system anisotropy on the dFRF.

### *4.2 Development of Two-Sided AMI to Process dFRFs*

Two-Sided AMI retains the basic structure of the original AMI. The general concepts of the Subtraction and Isolation phases are unchanged. During FRF processing, the original version of AMI takes advantage of the conjugate evenness of the FRF by only processing data in the positive frequency range. Since the dFRF is not conjugate-even, Two-Sided AMI must employ different logic. The iterative search for dominant peaks in the dFRF during the Subtraction Phase is conducted over the entire  $-\omega_{\max}$  to  $\omega_{\max}$  frequency range.

In both the Subtraction and Isolation Phases of the original version of AMI, the FRF data is fit to an analytical representation associated with a single index in Eq. 16,

$$H \approx \frac{A_k}{i\omega - \lambda_k} + \frac{A_k^*}{i\omega - \lambda_k^*} \quad (69)$$

In Two-Sided AMI, the dFRF data is fit to the single term pole-residue form associated with a single index in Eq. 22. In the vicinity of an identified peak, the dFRF is approximated as

$$H \approx \frac{C_k}{i\omega - \lambda_k} \quad (70)$$

Cross multiplying and arranging terms gives

$$i\omega H - \lambda_k H = C_k \quad (71)$$

Further manipulation of the variables leads to a form suitable for a linear least squares implementation.

$$\begin{bmatrix} \{1\} & \{H\} \end{bmatrix} \begin{Bmatrix} C_k \\ \lambda_k \end{Bmatrix} = \{i\omega H\} \quad (72)$$

In these equations, the  $\{1\}$ ,  $\{H\}$ , and  $\{i\omega H\}$  column vectors have length corresponding to the length of the frequency vector  $\{\omega\}$  defining the frequency range to be analyzed around an identified peak. The number of such points must exceed two, so Eq. 72 represents an overdetermined set of equations for the two coefficients,  $C_k$  and  $\lambda_k$ . The data for this fit are selected based on the criterion that

$$|H(\omega_i)| \geq \frac{1}{2} |H_{peak}|, \quad (73)$$

which corresponds to points inside the quarter-power points for a lightly damped resonance. Two-Sided AMI's curve fitter uses a linear least squares complex variable routine to identify the values of  $\lambda_k$  and  $C_k$  that best fit Eq. 72 at the frequencies satisfying Eq. 73.

In the Subtraction Phase of the original AMI, the residual FRF is set to zero inside the bandwidth of each identified eigenvalue before the next mode is considered. This is done because subtraction of the identified mode's contribution from the FRF data gives the residual FRF the appearance of an anti-resonance, the shoulders of which would appear

to be peaks that AMI would try to fit. Similarly, in Two-Sided AMI, the portion of the residual dFRF inside the bandwidth of the identified eigenvalue is set to zero. However, Two-Sided AMI does not zero the portion of the residual dFRF inside the bandwidth of the complex conjugate of the identified eigenvalue, because the complex conjugate value is considered to be a distinct eigenvalue.

### 4.3 *Two-Sided AMI Testing with Rigid Rotor System*

#### 4.3.1 Analytical Model Description

Two versions of an analytical model of a simple system are used to begin the assessment of the performance of Two-Sided AMI. In the first analysis, the isotropic system defined by Lee [38] is used without modification, whereas the second analysis modifies the system to feature anisotropy. The system consists of a rigid rotor supported by two identical bearings, as shown in Figure 3. The total mass of the system is  $m = 7.0$  kg. Each bearing has identical properties, consisting of damping coefficients  $c_{yy} = c_{zz} = 330$  N·s/m, and  $c_{yz} = c_{zy} = 20$  N·s/m, and stiffness coefficients  $k_{yy} = k_{zz} = 4 \times 10^6$  N/m and  $k_{yz} = k_{zy} = 7 \times 10^4$  N/m. The dimensionless bearing locations (defined as  $l_i = L_i/L$ ) are  $l_1 = l_2 = 0.5$ . The overall length of the shaft,  $L$ , factors out of the equations of motion, and is not defined in the reference. The dimensionless polar and transverse mass moments of inertia are  $i_t = 0.6$  and  $i_p = 0.15$ , respectively. The shaft speed is held constant at  $\Omega = 1 \times 10^4$  RPM. The four generalized coordinates for this system are the  $Y$ -direction and  $Z$ -direction displacements at Bearings 1 and 2. This definition of generalized coordinates matches the physical displacements, so that  $\{\hat{q}\} = \{q\}$  (see Eq. 5). For the second analysis, system anisotropy is included in the analytical model by changing the relationships between bearing stiffness and damping coefficients to be  $k_{yy} = 0.8k_{zz} = 3.2 \times 10^6$  N/m and  $c_{yy} = 0.8c_{zz} = 264$  N·s/m. No other parameters are changed.

Eq. 4 is solved in the frequency domain to obtain the FRFs  $H_{YY}$ ,  $H_{ZZ}$ ,  $H_{ZY}$ , and  $H_{YZ}$  at Bearing 1. Eqs. 21 are used to calculate the dFRFs  $H_{PG}$  and  $H_{P\hat{G}}$ . The maximum frequency,  $\omega_{\max}$ , for the calculations is 3000 rad/s. Standard one-sided FRFs are processed by the original version of AMI. Two-sided FRFs (a standard FRF with the



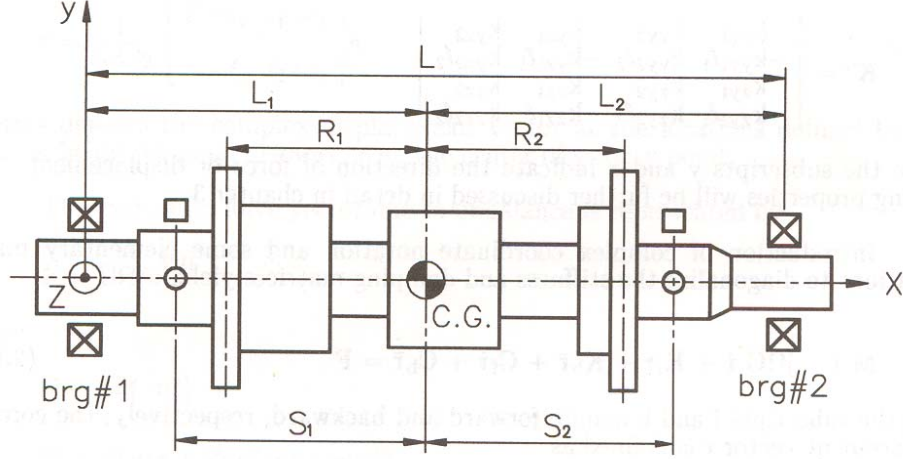


**Figure 3:** Rigid rotor system [38].

complex conjugate in the negative frequency range) and dFRFs are processed by Two-Sided AMI. Although such processing yields modal displacements at the bearings, only the eigenvalues are examined here. Lee [38] and Joh and Lee [34] showed that the reverse dFRF,  $H_{P\hat{G}}$ , approaches zero as a system approaches isotropy. For the isotropic system used in the first analysis, the amplitude of  $H_{P\hat{G}}$  is on the order of  $10^{-22}$ . Therefore, only the normal dFRF,  $H_{PG}$ , is processed in the first analysis.

### 4.3.2 Results

#### 4.3.2.1 Isotropic System

The FRFs  $H_{YY}$  and  $H_{ZY}$  and the dFRF  $H_{PG}$ , all at Bearing 1, are shown in Figures 4, 5, and 6. The actual eigenvalues are known from solution of the state-space equations at the specified operating condition. The solution consists of four underdamped modes whose eigenvalues are shown in Tables 3 and 4. Modal damping ratios (Eq. 15) increase from 4% to 8% with increasing mode number. The exact eigenvalues, the eigenvalues obtained from original and Two-Sided AMI processing of  $H_{YY}$ , and the eigenvalues obtained from Two-Sided AMI processing of  $H_{PG}$  are shown in Tables 3 and 4, along with associated error values. (Percent error is calculated in the standard manner relative to the exact solution for the mode's eigenvalue.) Values marked as “n/a” correspond to modes that

were not identified. In Tables 1 through 4, a designator precedes each value of  $\text{Im}(\lambda_i)$  estimated by Two-Sided AMI. A (+) indicates that the mode was detected in the positive frequency range, a (-) indicates that the mode was detected in the negative frequency range, and a ( $\pm$ ) indicates that an average value is reported because the mode was detected in both frequency ranges. Two-Sided AMI processing of the dFRF data produced an estimate for the eigenvalue of each of the four modes in the exact solution, while processing standard FRF data with both the original AMI and Two-Sided AMI yielded estimates for two modes. The bandwidth of a resonance is approximately  $-2\text{Re}(\lambda_n)$ . Thus the modes that were missed overlap substantially with the ones that were identified. The absolute value of the percent error of the eigenvalues estimated by Two-Sided AMI processing of the dFRF ranged from 0% to 17% for the real part, and from 0.5% to 8% for the imaginary part. The absolute value of the error of the eigenvalues estimated by AMI processing of the FRF ranged from 23% to 74% for the real part, and from 0.1% to 1% for the imaginary part. The corresponding errors when Two-Sided AMI processed the FRF data ranged from 24% to 85% for the real part, and from 0.03% to 2% for the imaginary part.

**Table 3:** Rigid rotor system; isotropic case. Analytical eigenvalues, Two-Sided AMI estimated eigenvalues, AMI estimated eigenvalues, and percent error for modes 1 and 2 of isotropic system. (+) = detected in positive frequency range, (-) = detected in negative frequency range, and (+/-) = detected in both ranges with average value reported.

	$\text{Re}(\lambda_1)$	$\text{Im}(\lambda_1)$	$\text{Re}(\lambda_2)$	$\text{Im}(\lambda_2)$
<i>Analytical Sol.</i>	-37.9061	1065.1916	-56.3796	1070.9059
<i>2-Sided AMI <math>H_{PG}</math>.</i>	-37.9061	(+)1070.9059	-56.3796	(-)1065.1917
<i>% Error</i>	0.00	0.54	0.00	-0.53
<i>AMI <math>H_{YY}</math></i>	n/a	n/a	-43.3660	1070.1474
<i>% Error</i>	n/a	n/a	-23.08	-0.07
<i>2-Sided AMI <math>H_{YY}</math></i>	n/a	n/a	-43.0623	( $\pm$ )1070.5418
<i>% Error</i>	n/a	n/a	-23.62	-0.03

#### 4.3.2.2 Anisotropic System

The FRFs  $H_{YY}$  and  $H_{ZY}$  for the response in the anisotropic case at Bearing 1 are shown in Figures 7 and 8. The dFRFs  $H_{PG}$  and  $H_{P\hat{G}}$  for this case are shown in Figure 9. The actual eigenvalues, corresponding to four underdamped modes, are listed in Tables 5 and 6. Modal damping ratios are comparable to those for the isotropic system. The exact

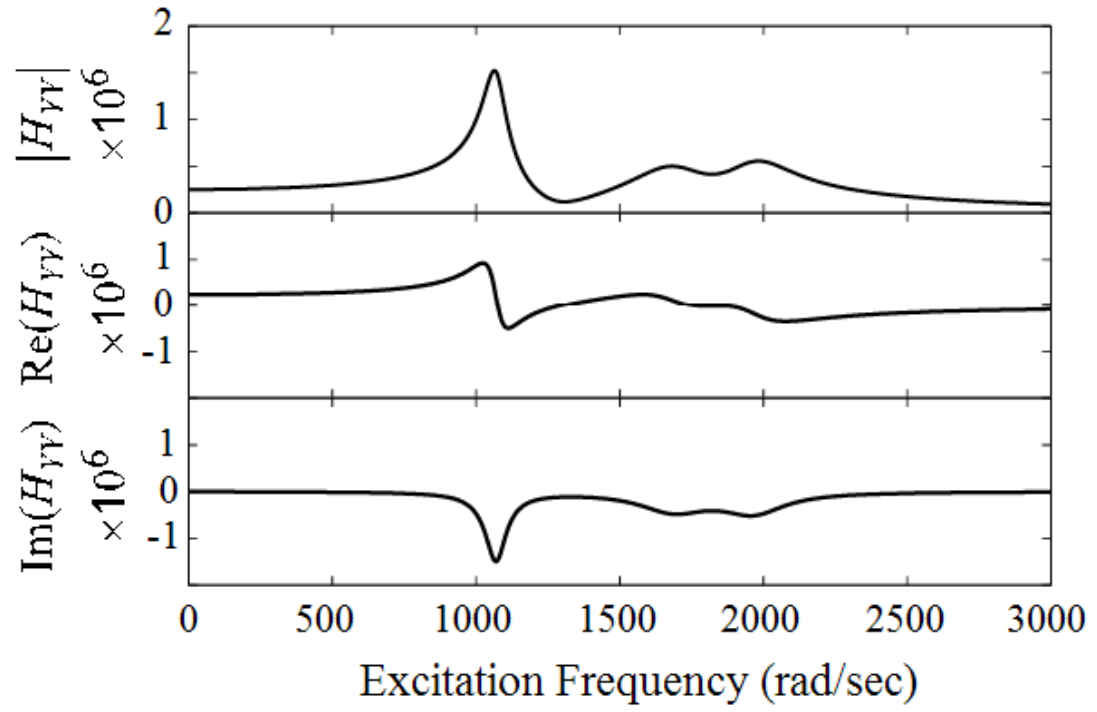


**Figure 4:** Rigid rotor system; isotropic case. FRF  $H_{YV}$  at bearing 1.

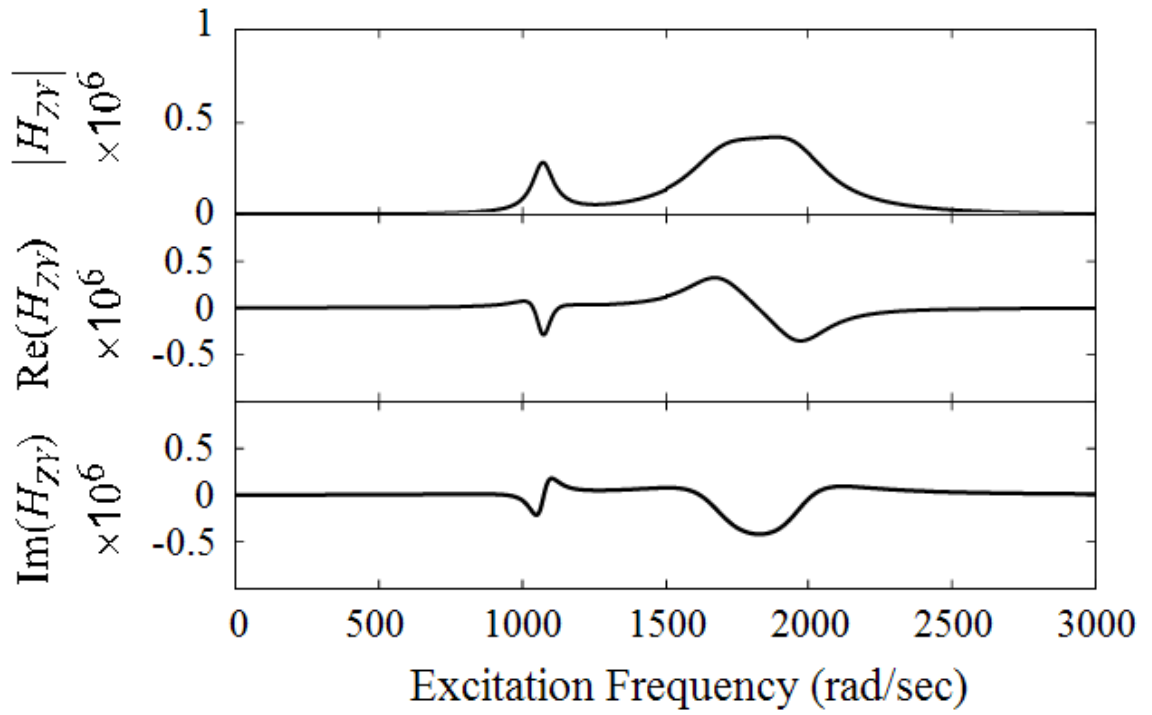


**Figure 5:** Rigid rotor system; isotropic case. FRF  $H_{ZY}$  at bearing 1.

**Table 4:** Rigid rotor system; isotropic case. Analytical eigenvalues, Two-Sided AMI estimated eigenvalues, AMI estimated eigenvalues, and percent error for modes 3 and 4 of isotropic system. (+) = detected in positive frequency range, (-) = detected in negative frequency range, and (+/-) = detected in both ranges with average value reported.

	$\text{Re}(\lambda_3)$	$\text{Im}(\lambda_3)$	$\text{Re}(\lambda_4)$	$\text{Im}(\lambda_4)$
<i>Analytical Sol.</i>	-122.0999	1812.4321	-152.9000	1828.8487
<i>2-Sided AMI <math>H_{PG}</math>.</i>	-142.9889	(-)1686.6485	-132.0110	(+)1965.1144
<i>% Error</i>	17.11	-6.94	-13.66	7.45
<i>AMI <math>H_{YY}</math></i>	n/a	n/a	-267.2982	1852.9996
<i>% Error</i>	n/a	n/a	74.81	1.32
<i>2-Sided AMI <math>H_{YY}</math></i>	n/a	n/a	-282.8052	( $\pm$ )1868.2299
<i>% Error</i>	n/a	n/a	84.96	2.15

eigenvalues, the eigenvalues obtained from original and Two-Sided AMI processing of  $H_{YY}$ , and the eigenvalues obtained from Two-Sided AMI processing of  $H_{PG}$  and  $H_{PG}$  are shown in Tables 5 and 6, along with associated error values. Two-Sided AMI yielded estimates of four modes for  $H_{PG}$  data, and of three modes for  $H_{PG}$  data. Original and Two-Sided AMI processing of  $H_{YY}$  both yielded estimates for three modes. The absolute value of the error of the eigenvalues identified by Two-Sided AMI from the dFRFs ranged from 0.4% to 11% for the real part, and from 0.04% to 5% for the imaginary part. These are essentially the same as the errors when Two-Sided AMI processed the FRF data, which ranged from 0.4% to 8% for the real part, and from 0.01% to 4% for the imaginary part. Furthermore, the errors in the eigenvalues extracted from the FRFs, which ranged from 0.5% to 8% for the real part, and from 0.1% to 4% for the imaginary part, differ little from those associated with using Two-Sided AMI.

### 4.3.3 Discussion

#### 4.3.3.1 Isotropic System

For the isotropic analytical model, Two-Sided AMI processing of dFRF data generated estimates of the eigenvalues for every mode in the analytical solution, while original and Two-Sided AMI processing of standard FRF data both yielded estimates for only half the modes. Lee [38] showed that the closely-spaced backward and forward modes commonly associated with rotating structures are completely separated and put into the negative and positive frequency ranges, respectively, of the normal dFRF,  $H_{PG}$ , for an isotropic system.

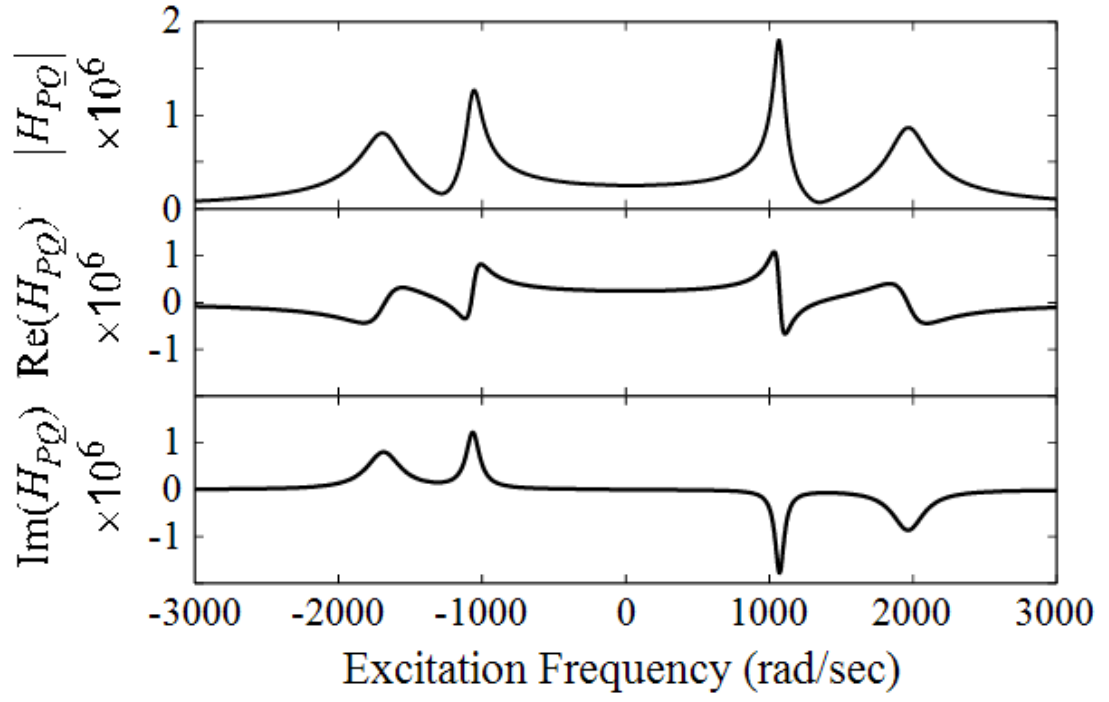


**Figure 6:** Rigid rotor system; isotropic case. dFRF  $H_{PG}$  at bearing 1.

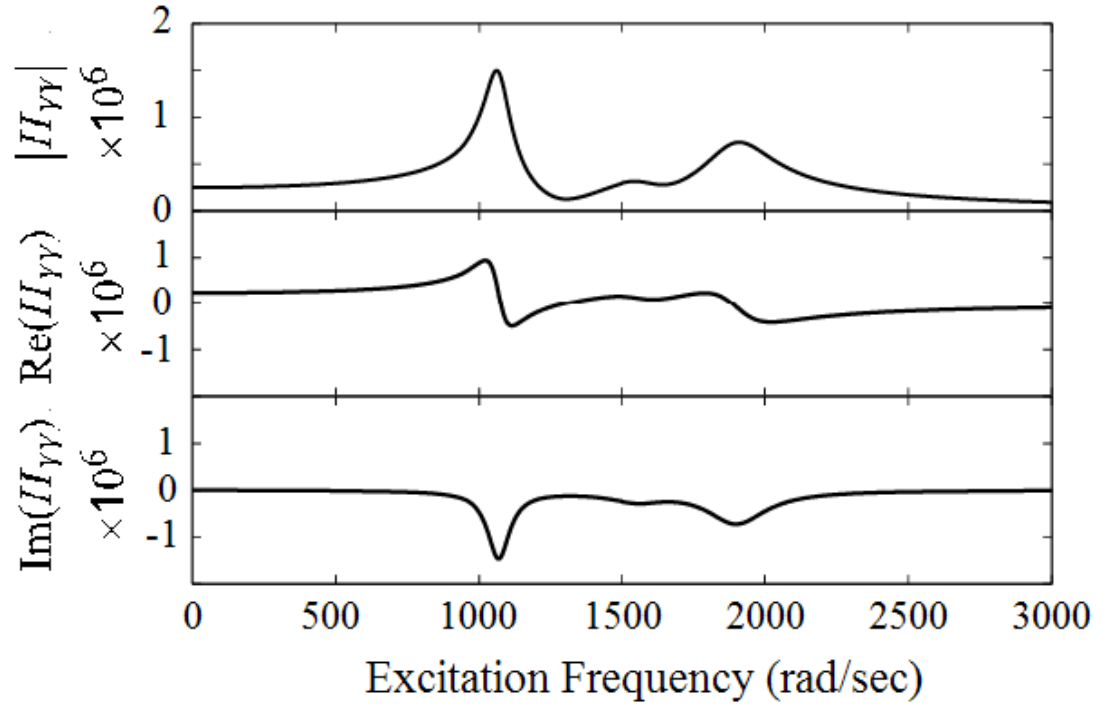


**Figure 7:** Rigid rotor system; anisotropic case. FRF  $H_{YY}$  at bearing 1.

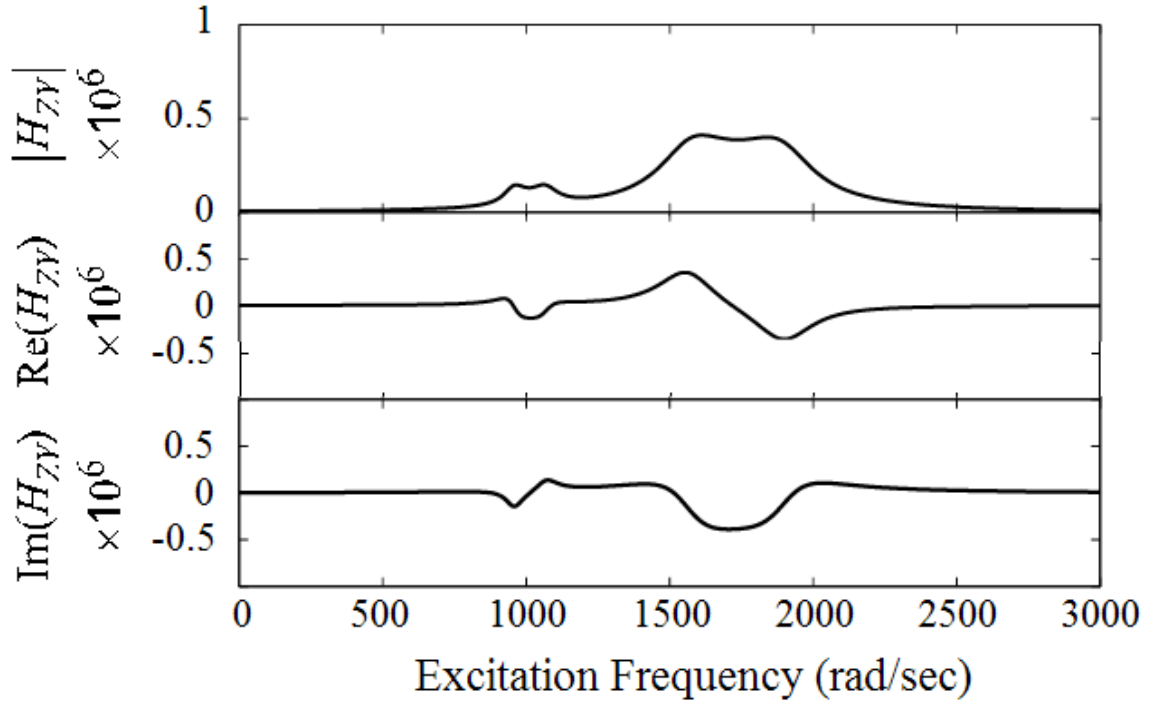


**Figure 8:** Rigid rotor system; anisotropic case. FRF  $H_{ZY}$  at bearing 1.

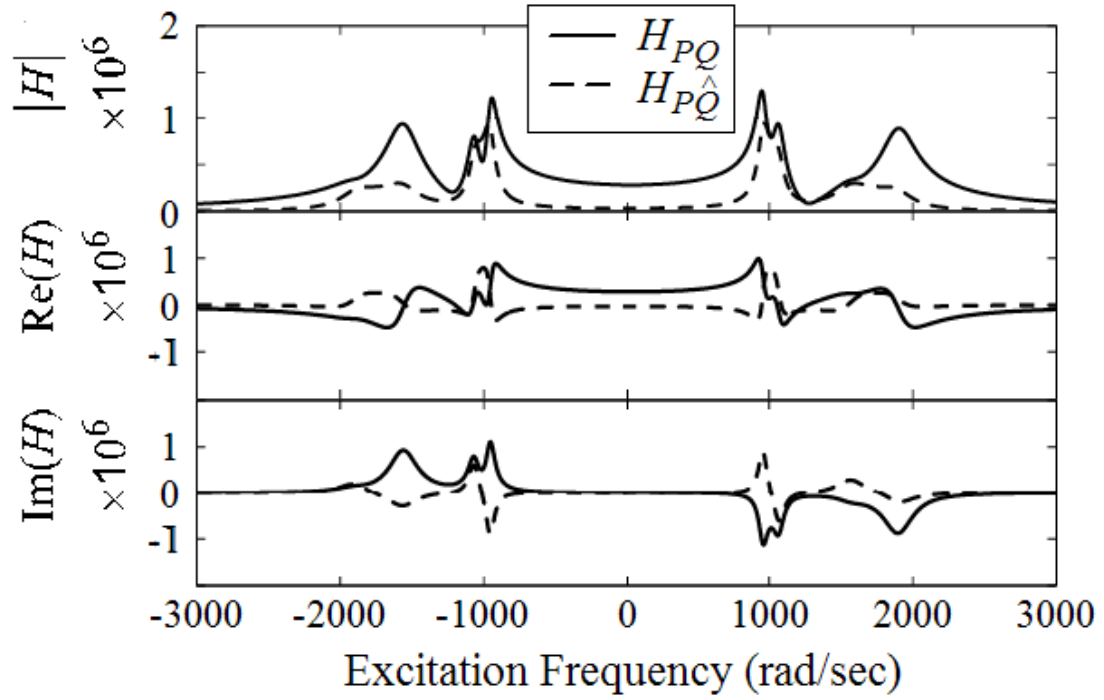


**Figure 9:** Rigid rotor system; anisotropic case. dFRFs  $H_{PG}$  (solid) and  $H_{\hat{PG}}$  (dashed) at bearing 1.

**Table 5:** Rigid rotor system; anisotropic case. Analytical eigenvalues, Two-Sided AMI estimated eigenvalues, AMI estimated eigenvalues, and percent error for modes 1 and 2 of anisotropic System. (+) = detected in positive frequency range, (-) = detected in negative frequency range, and (+/-) = detected in both ranges with average value reported.

	$\text{Re}(\lambda_1)$	$\text{Im}(\lambda_1)$	$\text{Re}(\lambda_2)$	$\text{Im}(\lambda_2)$
<i>Analytical Sol.</i>	-38.1479	956.3078	-46.7091	1067.2385
<i>2-Sided AMI <math>H_{PG}</math>.</i>	-38.9109	( $\pm$ )955.8842	-45.9612	( $\pm$ )1066.2020
<i>% Error</i>	2.00	-0.04	-1.60	-0.10
<i>2-Sided AMI <math>H_{P\hat{G}}</math>.</i>	-42.0632	( $\pm$ )956.7178	-50.3972	( $\pm$ )1065.7674
<i>% Error</i>	10.26	0.04	7.90	-0.14
<i>AMI <math>H_{YY}</math></i>	n/a	n/a	-46.4710	1066.6758
<i>% Error</i>	n/a	n/a	-0.51	-0.05
<i>2-Sided AMI <math>H_{YY}</math></i>	n/a	n/a	-46.5064	( $\pm$ )1067.0891
<i>% Error</i>	n/a	n/a	-0.43	-0.01

**Table 6:** Rigid rotor system; anisotropic case. Analytical eigenvalues, Two-Sided AMI estimated eigenvalues, AMI estimated eigenvalues, and percent error for modes 3 and 4 of anisotropic system. (+) = detected in positive frequency range, (-) = detected in negative frequency range, and (+/-) = detected in both ranges with average value reported.

	$\text{Re}(\lambda_3)$	$\text{Im}(\lambda_3)$	$\text{Re}(\lambda_4)$	$\text{Im}(\lambda_4)$
<i>Analytical Sol.</i>	-111.2414	1630.6042	-136.2585	1819.4306
<i>2-Sided AMI <math>H_{PG}</math>.</i>	-123.0010	(-)1557.3899	-130.6804	(+)1902.6735
<i>% Error</i>	10.57	-4.49	-4.09	4.58
<i>2-Sided AMI <math>H_{P\hat{G}}</math>.</i>	-111.6492	( $\pm$ )1687.8668	n/a	n/a
<i>% Error</i>	0.37	3.51	n/a	n/a
<i>AMI <math>H_{YY}</math></i>	-120.2780	1561.4463	-125.6849	1898.6377
<i>% Error</i>	8.12	-4.24	-7.76	4.35
<i>2-Sided AMI <math>H_{YY}</math></i>	-120.4768	( $\pm$ )1561.9604	-125.6941	( $\pm$ )1898.9813
<i>% Error</i>	8.30	-4.21	-7.75	4.37

The present analysis confirms this assertion, and points to the benefit of processing dFRF data for isotropic systems. Original and Two-Sided AMI processing of the regular FRF,  $H_{YY}$ , yielded only two modes due to the overlapping of forward and backward modes in the standard FRF.

Overall, the estimates for the imaginary parts of the eigenvalues of the isotropic system were more accurate than the estimates for the real parts for both FRF and dFRF data. However, the error of the estimates of the real parts of mode 1 ( $-37.9061 + i1065.1916$ ) and mode 2 ( $-56.3796 + i1070.9059$ ) for the dFRF data were extremely small. The Two-Sided AMI estimates for the real parts of the eigenvalues extracted from dFRF data were

considerably more accurate than the estimates obtained when the original AMI and Two-Sided AMI were applied to standard FRF data. The overlapping of the backward and forward modes in an FRF was the cause.

#### *4.3.3.2 Anisotropic System*

For the anisotropic analytical model, Two-Sided AMI processing of the normal dFRF still identified four modes, but both original and Two-Sided AMI processing of standard FRFs yielded three modes. Two-Sided AMI processing of a reverse dFRF also returned three modes. Unlike the behavior of the dFRFs in the case of an isotropic system, forward and backward modes appeared in both frequency ranges of the normal and reverse dFRF. Because the backward and forward modes were not completely split into the negative and positive frequency ranges, the standard FRF and both dFRFs were subject to overlapping of forward and backward modes for anisotropic systems.

Processing of both FRF and dFRF data for the anisotropic system yielded estimates of the imaginary parts of the eigenvalues that were more accurate than the estimated real parts. Although the Two-Sided AMI estimates of the real parts of the eigenvalues obtained from dFRF data were still slightly more accurate than the corresponding original AMI and Two-Sided AMI estimates from FRF data, none of the estimates for the real part of the eigenvalues in the anisotropic case featured the accuracy sometimes attained in the isotropic case. The overlapping of forward and backward modes in both the dFRF and the FRF for an anisotropic system was the cause.

#### *4.3.3.3 General*

Increased damping typically raises the difficulty of mode estimation in EMA. This was the situation in the present analysis. Errors in estimates of the real and imaginary parts of the eigenvalues for both systems typically increased with increasing damping.

Finally, it was observed that processing a specific standard FRF data set with original AMI and Two-Sided AMI yielded estimates of eigenvalues that followed the same trends, and were comparable in accuracy. For the systems investigated here, there was no benefit, in either number of modes detected or accuracy, in choosing one algorithm over the other



for processing standard FRF data.

#### 4.4 *Two-Sided AMI Testing with Prototypical System (Simplified Model)*

The simplified model of the prototypical system (Chapter III) is used to continue the assessment of the performance of Two-Sided AMI. In independent tests, the system, in its nominal configuration, is excited harmonically with unit amplitude forces ( $Y$ -direction force in the first test and  $Z$ -direction force in the second test) acting at the bearing closer to the disk (Bearing 1). FRFs in the  $Y$ -direction and  $Z$ -direction are calculated at Bearing 1 and Bearing 2 by a direct frequency domain solution of the equations for the Ritz series coefficients. The FRFs are then used to calculate the corresponding dFRFs at both bearings. Two-sided FRFs, composed of the standard FRF in the positive frequency range and the conjugate of the standard FRF in the negative frequency range, are also constructed. The maximum frequency,  $\omega_{\max}$ , for the FRF and dFRF calculations is 120 nondimensional frequency units. The FRF and dFRF data sets are processed independently by AMI and Two-Sided AMI. Although such processing yielded modal displacements at the bearings, only the eigenvalues are examined here.

##### 4.4.1 Results

Four representative data sets processed by AMI, the FRFs  $H_{YY}$  and  $H_{ZY}$  and the dFRFs  $H_{PG}$  and  $H_{P\hat{G}}$  at Bearing 1, are shown in Figures 10, 11, 12 and 13, respectively. It is evident that modes become less responsive as their natural frequency increases. The actual eigenvalues are known from solution of the state-space equations at the specified operating conditions. There are ten underdamped modes whose natural frequency lies in the frequency interval for processing,  $\omega < \omega_{\max}$ . (The graphs are cut off at frequency  $\omega = 80$  nondimensional frequency units to increase visual resolution, because analysis showed very little response between  $\omega = 80$  and  $\omega = 120$  nondimensional frequency units.) The system also has four overdamped modes,  $\lambda = -218.12 + 0i$ ,  $\lambda = -223.27 + 0i$ ,  $\lambda = -3148.2 + 0i$ , and  $\lambda = -3572.1 + 0i$ .

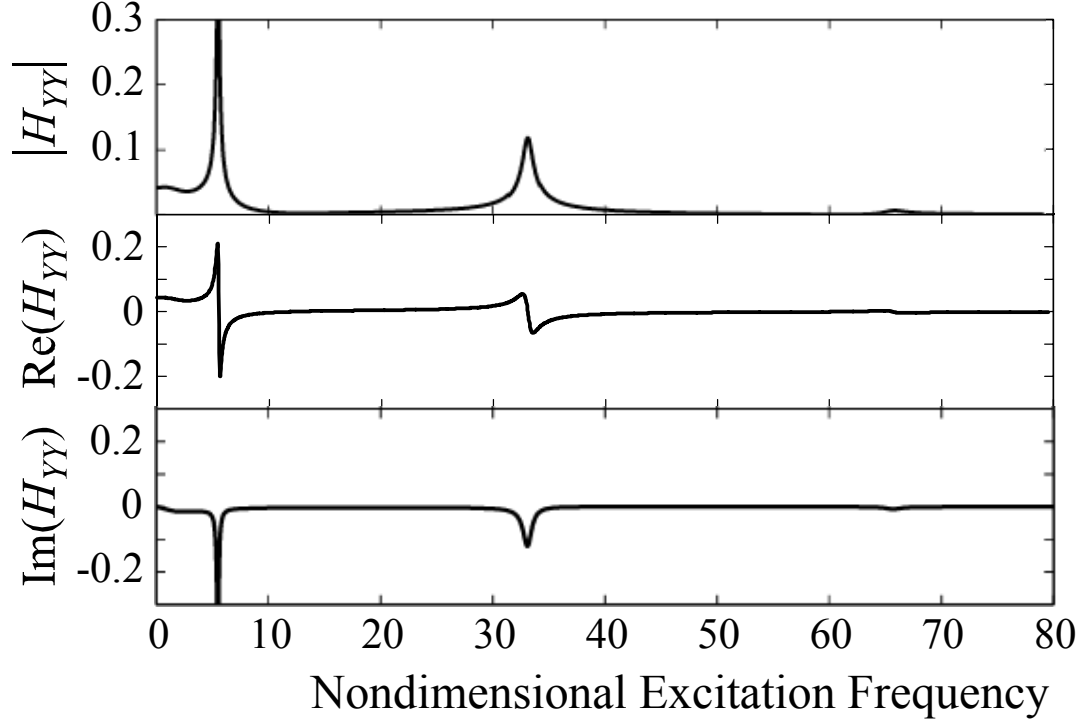
The analytical eigenvalues and damping ratios for the underdamped modes are shown in

Table 7. The combination of processing the FRF and dFRF data led to the identification of four modes. The real and imaginary parts of the eigenvalues obtained from AMI and Two-Sided AMI processing of the FRFs are shown in Tables 8 and 9, and the eigenvalues from Two-Sided AMI processing of the dFRFs are shown in Tables 10 and 11. In Tables 2 through 5, values marked as “n/a” correspond to modes that were not identified. A designator precedes each value of  $\text{Im}(\lambda_i)$  estimated by Two-Sided AMI: a (+) indicates that the mode was detected in the positive frequency range, a (−) indicates that the mode was detected in the negative frequency range, and a (±) indicates that an average value is reported because the mode was detected in both frequency ranges. Percent error is calculated in the standard manner relative to the exact solution.

The modes  $\lambda = -1.2569 + 5.4871i$  and  $\lambda = -1.2695 + 33.1138i$  were detected in each FRF and dFRF. Processing FRFs with the original AMI, and dFRFs with Two-Sided AMI, yielded acceptable estimates for the detected mode having the lowest frequency,  $\lambda = -0.8387 + 1.1097i$ . However, Two-Sided AMI processing of the FRF data led to estimates of this mode in which the imaginary part of the eigenvalue converged to zero. The high damping of this mode (60%), coupled with the low frequency and the conjugate-even property of the FRF, caused Two-Sided AMI to behave as though the two wide peaks, which are symmetrically placed close to zero frequency as a consequence of the conjugate-even property, represented one peak centered at zero. The mode  $\lambda = -1.4755 + 65.6800i$  was only detected when  $H_{YY}$  was processed by AMI and Two-Sided AMI. Processing  $H_{YY}$  at Bearings 1 and 2 yielded four detected modes, while the other FRFs each yielded two detected modes. Each dFRF yielded estimates of either two or three modes.

#### 4.4.2 Discussion

The analytical solution gives ten underdamped modes below  $\omega_{\max}$ , but the most modes detected by AMI processing of any one data set was four. Two major factors contribute to this. First, in order to emulate an actual piece of rotating equipment, the excitation and measurement locations were limited to the bearings. Most modes present in the analytical solution give extremely small responses with these excitation-measurement point



**Figure 10:** Prototypical system (simplified model); nominal condition. Magnitude, real part, and imaginary part of FRF  $H_{YY}$  at bearing 1.

pairs. Second, the high level of damping associated with the system's hydrodynamic bearings makes mode identification difficult. The modal damping ratios for the identified modes are quite large, ranging from 2% to 60%. (In addition, four modes are overdamped.) In the Subtraction Phase of AMI, an estimate for the identified mode is subtracted from the FRF (or dFRF) to bring the next largest peak into prominence. Since the estimate is not an exact representation of the mode, some modal content near the most dominant peak may be inadvertently subtracted from the FRF. This phenomenon is more likely with highly damped modes, because the estimate of the mode subtracted from the FRF covers a wider frequency range. The closely-spaced forward and backward modes associated with rotating structures overlap in the FRF, further compounding the problem. Furthermore, a dFRF is not immune to the difficulties resulting from overlapping of highly damped forward and backward modes, because dependence on the direction of the dead load makes the bearing behave anisotropically. Consequently, the forward and backward modes were

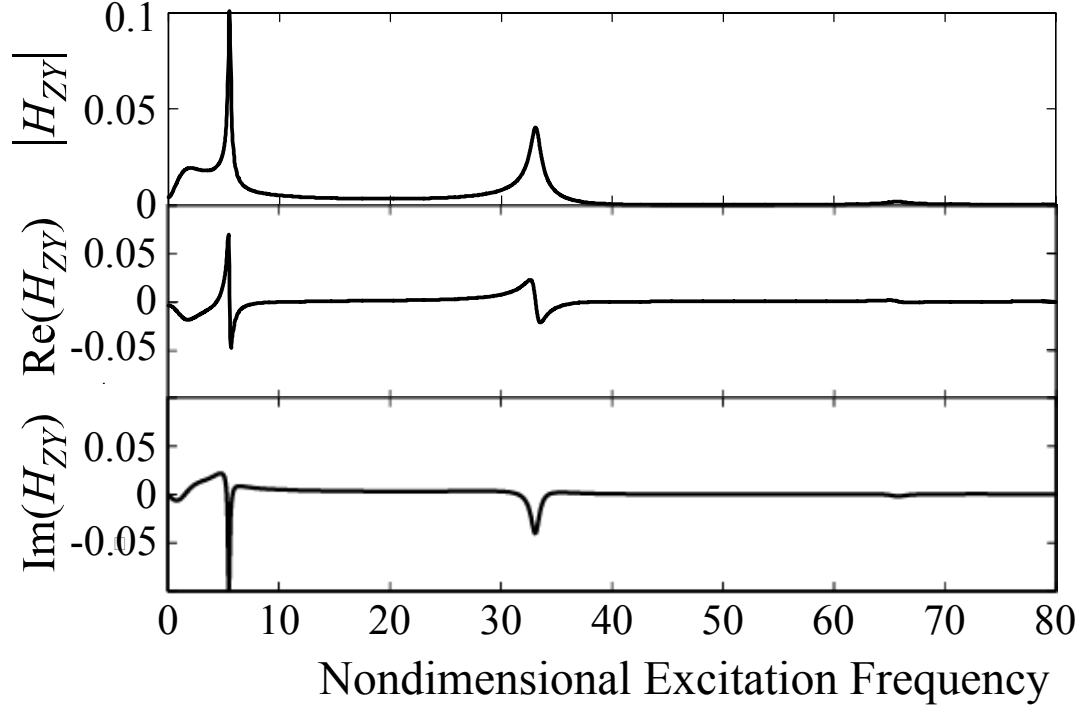


**Figure 11:** Prototypical system (simplified model); nominal condition. Magnitude, real part, and imaginary part of FRF  $H_{ZY}$  at bearing 1.

not completely separated into the positive and negative frequency ranges in the dFRFs.

Two-Sided AMI processing of FRF data was as accurate as AMI processing of FRF data for the two dominant modes ( $\lambda = -1.2569 + 5.4871i$  and  $\lambda = -1.2695 + 33.1138i$ ). For the highest frequency mode that was detected ( $\lambda = -1.4755 + 65.6800i$ ), the Two-Sided AMI estimates of the real part of the eigenvalue were only half as accurate as the corresponding AMI estimates, although both algorithms' estimates for the imaginary part of that eigenvalue had equal accuracy. Two-Sided AMI yielded poor estimates for the eigenvalue associated with the lowest frequency mode that was detected ( $\lambda = -0.8387 + 1.1097i$ ). This is a consequence of the conjugate-even property of a low-frequency, low Q mode, as explained in the preceding section. Overall, for the system in question, AMI delivered performance superior to that of Two-Sided AMI when applied to FRF data.

Approximately the same number of modes was detected from the FRFs and the dFRFs. However, half of the standard FRF data sets processed by AMI yielded the maximum number of detected modes (four), while the best performing dFRF and two-sided FRF data

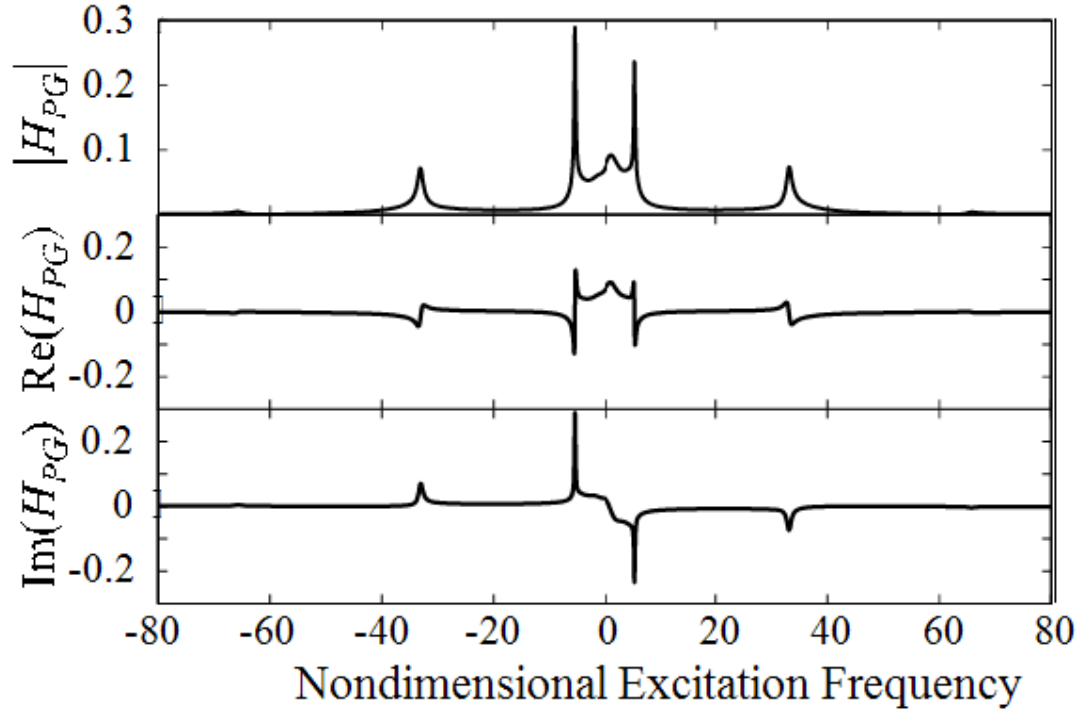


**Figure 12:** Prototypical system (simplified model); nominal condition. Magnitude, real part, and imaginary part of dFRF  $H_{PG}$  at bearing 1.

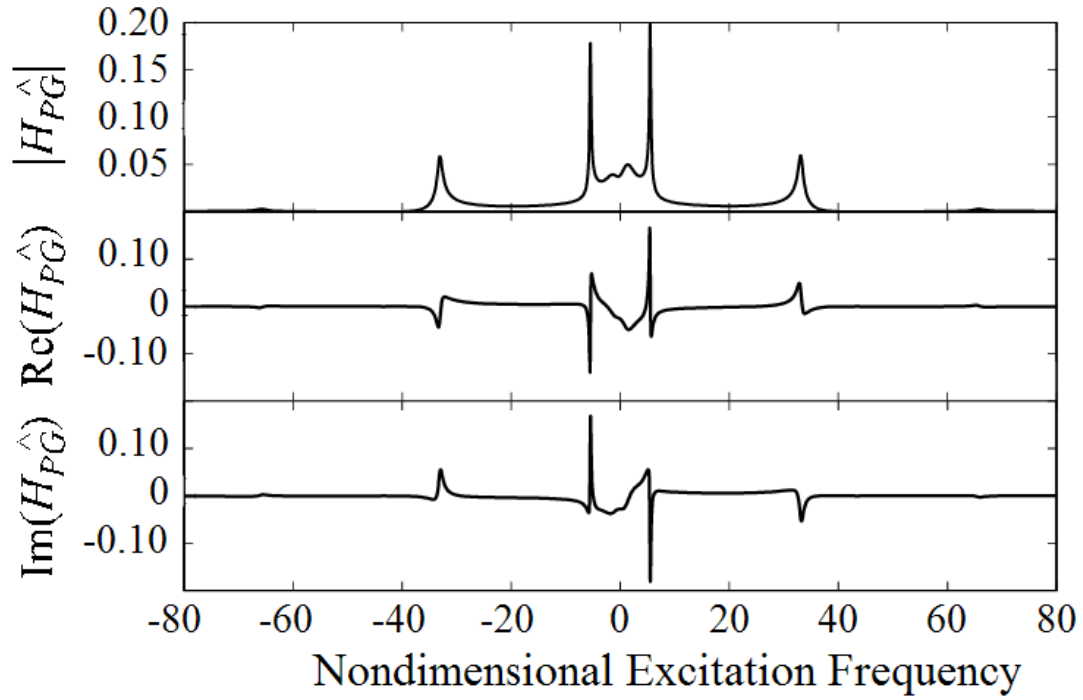


**Figure 13:** Prototypical system (simplified model); nominal condition. Magnitude, real part, and imaginary part of dFRF  $\hat{H}_{PG}$  at bearing 1.

**Table 7:** Prototypical system; nominal condition. Analytical eigenvalues and damping ratios for all underdamped modes below 120 nondimensional frequency units.

Mode	$\text{Re}(\lambda_k)$	$\text{Im}(\lambda_k)$	Damping Ratio
1	-0.8387	1.1097	0.6030
2	-0.8740	1.2591	0.5702
3	-1.1856	5.0518	0.2285
4	-1.2569	5.4871	0.2233
5	-1.2695	33.1138	0.0383
6	-1.4225	33.6863	0.0422
7	-1.4755	65.6800	0.0225
8	-1.9183	67.8824	0.0282
9	-2.0419	110.0420	0.0186
10	-2.7791	114.4801	0.0243

sets yielded only three modes. Furthermore, the highest frequency detected mode was only found by processing FRF data. The estimates for the imaginary part of the eigenvalues were considerably more accurate than the estimates for the real part of the eigenvalues for both FRF and dFRF data. Also, the estimates of the imaginary part of the eigenvalue extracted from the FRF data were more accurate than their dFRF counterparts. For the two dominant modes, the estimates of the real part of the eigenvalues from dFRF data were only slightly more accurate than those from FRF data.

For the highly damped, anisotropic system investigated here, there was no benefit to processing dFRF data in addition to FRF data. It is conjectured, however, that the best approach in the analysis of a rotordynamic system of unknown characteristics is to capture response data in the FRF format, construct the corresponding dFRFs, separately process the FRFs with AMI and the dFRFs with Two-Sided AMI, and then merge both resulting sets of modal properties.

**Table 8:** Prototypical system (simplified model); nominal condition. Analytical eigenvalues, eigenvalues estimated by AMI processing of FRF, and eigenvalues estimated by Two-Sided AMI processing of FRF for two lower-frequency detected modes. (+) = detected in positive frequency range, (-) = detected in negative frequency range, and (+/-) = detected in both ranges with average value reported.

	Re( $\lambda$ )	Im( $\lambda$ )	Re( $\lambda$ )	Im( $\lambda$ )
<i>Analytical Solution</i>	-0.8387	1.1097	-1.2569	5.4871
<i>AMI <math>H_{YY}</math>@1</i>	-1.5585	1.1198	-0.1110	5.4883
<i>% Error</i>	85.83	0.91	-91.17	0.02
<i>AMI <math>H_{YY}</math>@2</i>	-1.8332	1.3230	-0.1109	5.4884
<i>% Error</i>	118.58	19.22	-91.18	0.02
<i>AMI <math>H_{ZY}</math>@1</i>	n/a	n/a	-.0800	5.4836
<i>% Error</i>	n/a	n/a	-93.64	-0.06
<i>AMI <math>H_{ZY}</math>@2</i>	n/a	n/a	-0.0872	5.4804
<i>% Error</i>	n/a	n/a	-93.06	-0.12
<i>2-Sided AMI <math>H_{YY}</math>@1</i>	-2.1598	0.0000	-0.1105	( $\pm$ )5.4887
<i>% Error</i>	-357.52	-100	-91.20	0.03
<i>2-Sided AMI <math>H_{YY}</math>@2</i>	-2.3105	(-)0.0029	-0.1106	( $\pm$ )5.4885
<i>% Error</i>	-375.50	-100.27	-91.20	0.03
<i>2-Sided AMI <math>H_{ZY}</math>@1</i>	n/a	n/a	-0.0857	( $\pm$ )5.4838
<i>% Error</i>	n/a	n/a	-93.18	-0.06
<i>2-Sided AMI <math>H_{ZY}</math>@2</i>	n/a	n/a	-0.0916	( $\pm$ )5.4813
<i>% Error</i>	n/a	n/a	-92.71	-0.11

**Table 9:** Prototypical system (simplified model); nominal condition. Analytical eigenvalues, eigenvalues estimated by AMI processing of FRF, and eigenvalues estimated by Two-Sided AMI processing of FRF for two higher-frequency detected modes. (+) = detected in positive frequency range, (-) = detected in negative frequency range, and (+/-) = detected in both ranges with average value reported.

	Re( $\lambda$ )	Im( $\lambda$ )	Re( $\lambda$ )	Im( $\lambda$ )
<i>Analytical Solution</i>	-1.2695	33.1138	-1.4755	65.6800
<i>AMI <math>H_{YY}</math>@1</i>	-0.4636	33.1186	-0.8005	65.6635
<i>% Error</i>	-63.48	0.01	-45.75	-0.03
<i>AMI <math>H_{YY}</math>@2</i>	-0.4641	33.1165	-0.8119	65.6680
<i>% Error</i>	-63.44	0.01	-44.97	-0.02
<i>AMI <math>H_{ZY}</math>@1</i>	-0.3911	33.0664	n/a	n/a
<i>% Error</i>	-69.19	-0.14	n/a	n/a
<i>AMI <math>H_{ZY}</math>@2</i>	-0.3929	33.0832	n/a	n/a
<i>% Error</i>	-69.05	-0.09	n/a	n/a
<i>2-Sided AMI <math>H_{YY}</math>@1</i>	-0.4620	( $\pm$ )33.1182	-0.7804	( $\pm$ )65.6672
<i>% Error</i>	-63.61	0.01	-152.87	-0.02
<i>2-Sided AMI <math>H_{YY}</math>@2</i>	-0.4625	( $\pm$ )33.1164	-0.7995	( $\pm$ )65.6711
<i>% Error</i>	-63.57	0.01	-154.18	-0.01
<i>2-Sided AMI <math>H_{ZY}</math>@1</i>	-0.4024	( $\pm$ )33.0723	n/a	n/a
<i>% Error</i>	-68.30	-0.13	n/a	n/a
<i>2-Sided AMI <math>H_{ZY}</math>@2</i>	-0.4018	( $\pm$ )33.0887	n/a	n/a
<i>% Error</i>	-68.35	-0.08	n/a	n/a

**Table 10:** Prototypical system (simplified model); nominal condition. Analytical eigenvalues and eigenvalues estimated by Two-Sided AMI processing of dFRF for two lower-frequency detected modes. (+) = detected in positive frequency range, (-) = detected in negative frequency range, and (+/-) = detected in both ranges with average value reported.

	Re( $\lambda$ )	Im( $\lambda$ )	Re( $\lambda$ )	Im( $\lambda$ )
<i>Analytical Solution</i>	-0.8387	1.1097	-1.2569	5.4871
<i>2-Sided AMI <math>H_{PG}</math>@1</i>	-1.9748	(+)1.3534	-0.1200	( $\pm$ )5.4944
<i>% Error</i>	-335.46	21.97	-90.46	0.13
<i>2-Sided AMI <math>H_{PG}</math>@2</i>	n/a	n/a	-0.1303	( $\pm$ )5.4938
<i>% Error</i>	n/a	n/a	-89.63	0.04
<i>2-Sided AMI <math>H_{P\hat{G}}</math>@1</i>	-2.9134	(-)1.1479	-0.1051	( $\pm$ )5.4742
<i>% Error</i>	-447.37	3.45	-91.64	-0.24
<i>2-Sided AMI <math>H_{P\hat{G}}</math>@2</i>	-3.3726	(-)0.8660	-0.1061	( $\pm$ )5.4733
<i>% Error</i>	-502.12	-21.96	-91.56	-0.25



**Table 11:** Prototypical system (simplified model); nominal condition. Analytical eigenvalues and eigenvalues estimated by Two-Sided AMI processing of dFRF for two higher-frequency modes. (+) = detected in positive frequency range, (-) = detected in negative frequency range, and (+/-) = detected in both ranges with average value reported.

	Re( $\lambda$ )	Im( $\lambda$ )	Re( $\lambda$ )	Im( $\lambda$ )
<i>Analytical Solution</i>	-1.2695	33.1138	-1.4755	65.6800
<i>2-Sided AMI <math>H_{PG}@1</math></i>	-0.496	( $\pm$ )33.1551	n/a	n/a
<i>% Error</i>	-60.93	0.12	n/a	n/a
<i>2-Sided AMI <math>H_{PG}@2</math></i>	-0.5251	( $\pm$ )33.1344	n/a	n/a
<i>% Error</i>	-58.64	0.06	n/a	n/a
<i>2-Sided AMI <math>H_{P\hat{G}}@1</math></i>	-0.4552	( $\pm$ )33.0590	n/a	n/a
<i>% Error</i>	-64.14	-0.17	n/a	n/a
<i>2-Sided AMI <math>H_{P\hat{G}}@2</math></i>	-0.4503	( $\pm$ )33.0761	n/a	n/a
<i>% Error</i>	-64.53	-0.11	n/a	n/a

## CHAPTER V

### EVALUATION OF EIGENVALUES AND RESIDUES FOR USE IN DETECTION OF A WORN BEARING

This chapter continues the analysis of the prototypical system. One worn bearing is the defect investigated. The shaft remains intact, so the simplified model of the prototypical system (Chapter III) is employed. As in the previous chapter, the standard frequency response function (FRF) form of the response data is processed with AMI, and the directional frequency response functions (dFRF) data is processed with Two-Sided AMI. Both analyses return estimates for system modal properties represented by poles (system eigenvalues) and associated residues, which depend on the modal displacements at the excitation and measurement locations. Four metrics are evaluated for both the eigenvalue and the residue: percent change in the real part, percent change in the imaginary part, percent change in the magnitude, and change in the phase. FRF and dFRF response data for a range of bearing clearances are processed, the proposed damage metrics are calculated, and a comparison with analytical data is used to determine if the metrics detect the known defect.

#### *5.1 Potential Damage Metrics*

The frequency domain responses extracted from the analytical model are the horizontal  $Y$  and vertical  $Z$  FRFs at both bearings resulting from separate, independent  $Y$ - and  $Z$ -direction excitations at the bearing whose clearance is varied. Forward and reverse dFRFs for each bearing are computed from this data. In the terminology of EMA the eigenvalues and residues are obtained by following a SISO (single input-single output) protocol. Each of the four FRFs are individually processed by the original AMI, while the four dFRFs are processed by Two-Sided AMI. Processing of each FRF yields a set of eigenvalues  $\lambda_k$ , and residues  $A_k$ . The former are system properties. Thus, if a specific mode is identified from more than one FRF, the overlapping values are averaged. Processing of each dFRF

leads to another set of eigenvalues, as well as residues  $C_k$ . The eigenvalues obtained from the dFRFs also are averaged, but they are not combined with the values obtained from the FRFs in order to track the merits of using each type of response function. Because the residues depend on the modal response at the drive and measurement locations, the residues associated with each FRF or dFRF are independent values.

The frequency response functions are evaluated for a sequence of bearing clearances. This yields a set of eigenvalues and residues as a function of frequency. Because overlapping eigenvalues are averaged, the number of eigenvalues that are tracked in this manner is the ensemble of the number of modes identified from the full set of four FRFs or dFRFs. In contrast, because the residues are distinct, the maximum number of residues that could be tracked is the total number of times modes are extracted from the FRFs or dFRFs. However, because each mode is not identified from each FRF or dFRF, the number of residues is less than four times the number of modes.

Damage metrics are obtained from each eigenvalue and residue that is extracted by AMI. The first four metrics are drawn from the eigenvalues, whose magnitude is analogous to the natural frequency of a single degree of freedom system, and whose real part is analogous to the free vibration decay rate of such a system. These metrics are percent change in the real part of the eigenvalue ( $\text{Re}(\lambda_k)$ ), percent change in the imaginary part of the eigenvalue ( $\text{Im}(\lambda_k)$ ), percent change in the magnitude of the eigenvalue ( $|\lambda_k|$ ), and change in the phase of the eigenvalue ( $\arg(\lambda_k)$ ). The remaining metrics are the corresponding types of quantities drawn from each residue.

### 5.1.1 Detectability

For a system defect to be detectable with a specific damage metric, the introduction of the defect into the system must result in a measurable change in that metric. Specifically, to be useful, a metric must have an uncertainty in its value that is less than the change in its value due to a system defect. In the present work this translates to a criterion that the increased bearing clearance is “detectable” with a specified metric if the change in that metric relative to its nominal value is greater than the error in the AMI estimate of that parameter at the

increased clearance. Because an analytical model is used to generate response data, the actual eigenvalues and residues are known from solution of the state-space equations at the specified operating condition. (The analytical eigenvalues and damping ratios for the first ten underdamped modes of the prototypical system in the nominal condition are shown in Table 7.) Hence, the errors in the AMI estimates of the modal properties are calculable.

The detectability determination is done graphically. For each eigenvalue or residue metric, two data sets are compiled and plotted as a function of bearing clearance: the change in the value relative to its value at the nominal clearance, and the error in the AMI estimation of that metric. The change in the metric is obviously zero at the reference state. If the metric is sufficiently sensitive, the amount by which it changes will exceed the estimation error at some bearing clearance within the range of interest. If only one such intersection exists, so that the change in the metric exceeds the error for bearing clearance beyond the intersection, then the intersection indicates the minimum bearing clearance at which bearing wear is detectable with the specific metric for the mode in question. This is the threshold of detectability. As will be seen, such an intersection does not necessarily occur. It also is possible that increase of the clearance beyond the intersection leads to an error that again exceeds the change in the metric, although that behavior was not observed. In either event, the metric would not serve as an indicator of wear.

## ***5.2 Analysis Method***

The system is operated at a constant rotation rate of 1.35 nondimensional frequency units, which is between the first two critical speeds, 0.73 and 2.30 nondimensional frequency units. The system is excited in separate, independent tests with  $Y$ -direction and  $Z$ -direction unit amplitude harmonic forces at the bearing closer to the disk (Bearing 1). FRFs in the  $Y$ -direction and  $Z$ -direction are calculated at Bearing 1 and Bearing 2, and are then used to calculate the corresponding dFRFs at both bearings. The maximum frequency,  $\omega_{\max}$ , for the calculations is 120 nondimensional frequency units. The FRF and dFRF data sets are processed independently by AMI and Two-Sided AMI.

The nominal radial clearance in the bearings is  $5 \times 10^{-5}$  m. The radial clearance of

Bearing 1 is increased to simulate bearing wear, while the clearance of Bearing 2 is held constant. At each clearance value, the complex frequency response is generated with the analytical model, and the damage metrics are calculated from the modal parameters estimated by AMI and Two-Sided AMI. The bearing clearances used in the investigation are shown in Table 12. The intent of this work is to develop metrics sensitive enough to detect small defects while the system is still operating normally. Thus, bearing clearances outside the close-running H8 fit class are not investigated.

**Table 12:** Bearing radial clearances used to simulate wear of Bearing 1.

Description	Clearance ( $\mu m$ )
nominal	50
10% increase	55
20% increase	60
30% increase	65
40% increase	70
60% increase	80
79% increase (Max H8)	89.5

### 5.3 Results

Over the course of the entire analysis, many FRFs and dFRFs are processed with original AMI and Two-Sided AMI, respectively. In every case, Two-Sided AMI identified three modes ( $\lambda = -0.8387 + 1.1097i$ ,  $\lambda = -1.2569 + 5.4871i$ , and  $\lambda = -1.2695 + 33.1138i$ ) from the dFRF data, and original AMI identified four system modes ( $\lambda = -1.4755 + 65.6800i$ , and the three modes listed above) from the FRF data. Note that the maximum possible number of identified modes is ten, since there are ten analytical modes in the frequency range of interest, as shown in Table 7.

Eigenvalues are global system quantities, and, as such, eigenvalues that are identified in separate FRFs, but represent the same mode, can be averaged. The residues associated with eigenvalues, on the other hand, are local quantities, because they depend on the modal displacements at the location the FRF is measured. As a result, a residue identified in one FRF can not be averaged with a residue identified in another FRF.

At a specific bearing clearance, a set of four FRFs ( $H_{YY}$  and  $H_{ZY}$  at Bearings 1 and 2)

is processed by original AMI. A set of four dFRFs ( $H_{PG}$  and  $H_{P\hat{G}}$  at Bearings 1 and 2) is calculated from FRFs and processed by Two-Sided AMI. Representative data for response of the nominal system at Bearing 1 are shown in the previously discussed Fig. 10 through Fig. 13. For each identified mode, the four eigenvalue-based damage metrics are calculated using the average of the mode's eigenvalues from the data set. For each identified mode, the four residue-based metrics are calculated for each residue returned from the data set. This process is repeated for each clearance value in Table 12.

The detectability evaluation is then conducted graphically. For each mode identified by original AMI (or Two-Sided AMI), the four eigenvalue-based metrics are plotted as functions of bearing clearance. Figure 14 illustrates this assessment regarding the eigenvalue-based metrics *percent change in  $\text{Re}(\lambda_k)$*  and *percent change in  $\text{Im}(\lambda_k)$* . The eigenvalue for this figure is  $\lambda = -1.2695 + 33.1138i$  in the nominal state. Figure 14 shows that the error in the AMI estimation of  $\text{Re}(\lambda_k)$  and  $\text{Im}(\lambda_k)$  is greater than the changes in these metrics for each increased clearance. Thus no amount of increased bearing wear can be detected by monitoring  $\text{Re}(\lambda_k)$  and  $\text{Im}(\lambda_k)$  for this mode.

The four residue-based metrics are also plotted as functions of bearing clearance for every residue identified from the input data. Figure 15 shows the data used in the evaluation of the metrics *percent change in  $\text{Re}(A_k)$*  and *percent change in  $\text{Im}(A_k)$*  for the residue identified by original AMI from  $H_{YY}$  at Bearing 1 corresponding to the nominal system mode  $\lambda = -1.2695 + 33.1138i$ . At a sufficiently large bearing clearance, *percent change in  $\text{Re}(A_k)$*  and *percent change in  $\text{Im}(A_k)$*  exceed the error in their estimation. The thresholds of detectability are a 30% clearance increase for *percent change in  $\text{Re}(A_k)$*  and a 10% clearance increase for *percent change in  $\text{Im}(A_k)$* .

### 5.3.1 Detectability Using Eigenvalues

The performance of the eigenvalue-based metrics is presented in Table 13. The results obtained by identifying modes from FRFs are followed by the comparable information derived from dFRFs. The row header for each type of data indicates the total number of modes

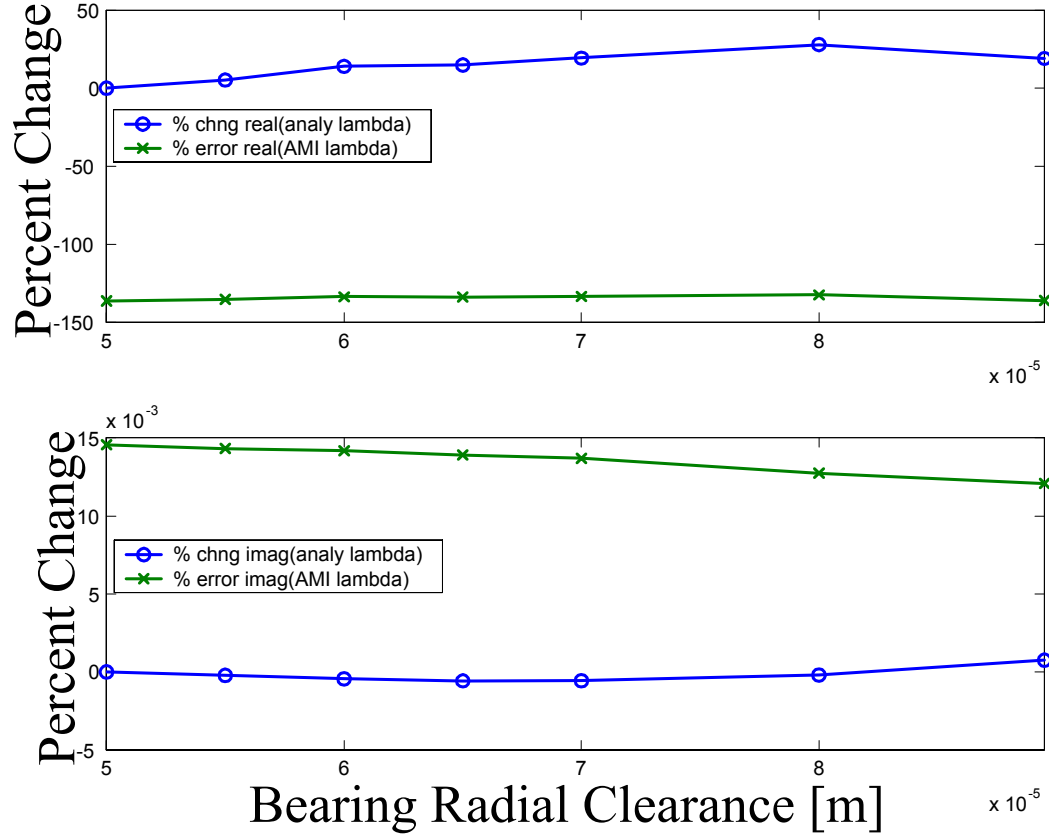


**Figure 14:** Detectability of eigenvalue properties using percent change  $\text{Re}(\lambda)$  and percent change  $\text{Im}(\lambda)$  for the nominal  $\lambda = -1.2695 + 33.1138i$  mode.

that were identified. Below that, the first entry, “Number/% of Modes Meeting Detectability Criterion,” quantifies how many times the type of metric indicated at the top of the column met the detectability criterion described previously. The second entry, “Average Clearance Change for Detectable Wear,” is derived only from the modes listed as meeting the detectability criterion. This number is the average of the bearing clearances at which the change in the associated metric exceeded the error in the identification of that metric.

No value of increased bearing clearance was detectable with the metrics *percent change in  $\text{Re}(\lambda_k)$* , *percent change in  $|\lambda_k|$* , and *change in  $\arg(\lambda_k)$*  for FRF data. The *percent change in  $\text{Im}(\lambda_k)$*  metric detected increased bearing clearance in the nominal system modes  $\lambda = -1.2569 + 5.4871i$  at 10% increase from nominal clearance, and  $\lambda = -0.8387 + 1.1097i$  at 60% clearance increase. Thus, the average clearance increase required for detectable wear

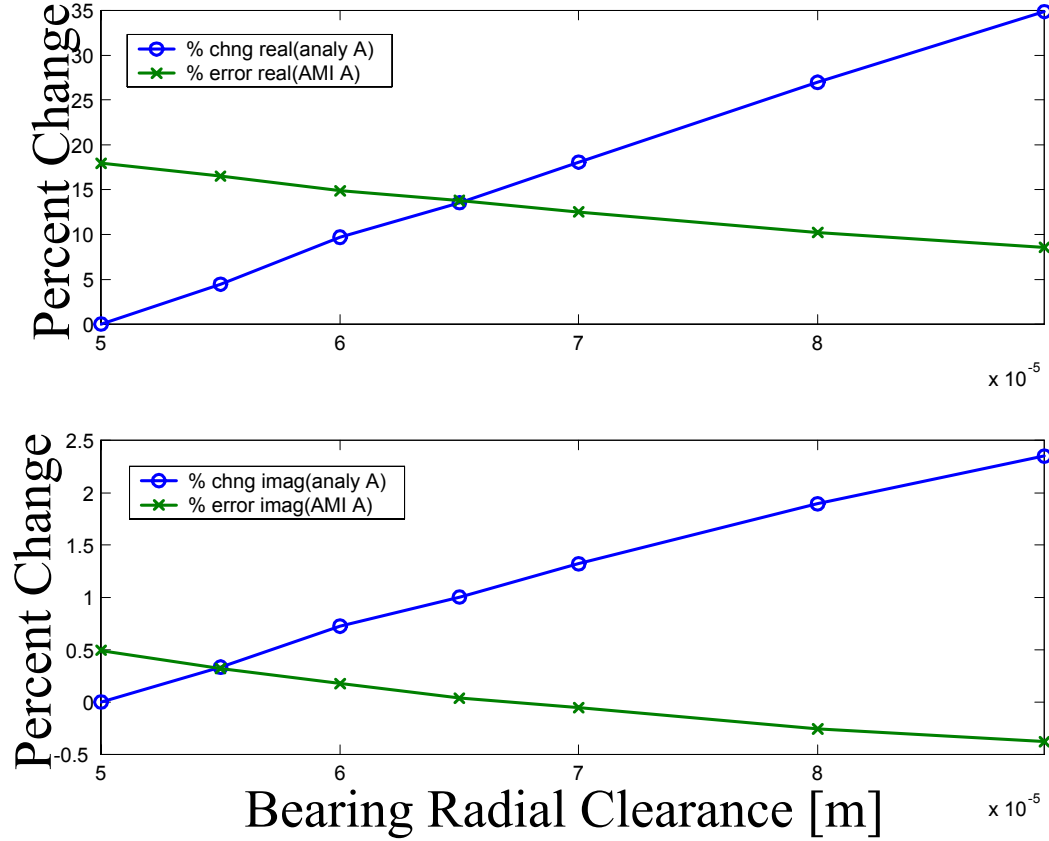


**Figure 15:** Detectability of residue properties using percent change  $\text{Re}(A)$  and percent change  $\text{Im}(A)$  with the nominal  $\lambda = -1.2695 + 33.1138i$  mode identified from  $H_{YY}$  at bearing 1.

with this metric was 35%. For dFRF data, no value of increased bearing clearance was detectable with the metrics *percent change in  $\text{Re}(\lambda_k)$* , *percent change in  $|\lambda_k|$* , and *change in  $\arg(\lambda_k)$* . The *percent change in  $\text{Im}(\lambda_k)$*  metric detected increased bearing clearance in the nominal system mode  $\lambda = -1.2569 + 5.4871i$  at 20% increase from nominal.

### 5.3.2 Detectability Using Residues

Table 14 displays the performance of the four residue-based damage metrics. As was done for the eigenvalues, the performance of metrics extracted from the FRFs is followed by the same information for dFRFs. The row header for each type of data gives how many residues were obtained from the full set of response functions. This is the sum of the number of times any mode is identified from each FRF. The maximum possible value of this quantity



**Table 13:** Performance of eigenvalue-based damage metrics for FRF and dFRF data.

Damage Metric	%Chng $\text{Re}(\lambda_k)$	%Chng $\text{Im}(\lambda_k)$	%Chng $ \lambda_k $	Chng $\arg(\lambda_k)$
<b>FRF Processing</b> (4 identified modes)				
Number/% of Modes Meeting Detectability Criterion	0	2/50%	0	0
Ave. Clearance Change for Detectable Wear	n/a	35%	n/a	n/a
<b>dFRF Processing</b> (3 identified modes)				
Number/% of Modes Meeting Detectability Criterion	0	1/33%	0	0
Ave. Clearance Change for Detectable Wear	n/a	20%	n/a	n/a

is forty, which is the ten underdamped modes in the analytical solution times the four FRFs or dFRFs in one complete data set. (This represents the situation in which every mode in the analytical situation is identified by AMI from each of the four FRFs.) The first entry below the row header, “Number/% of Modes Meeting Detectability Criterion,” is analogous to the first entry in Table 13 for the eigenvalue-based metrics, as described above. The second entry, “Number/% of Modes Meeting Detectability Criterion” refers to the number of residues identified from the full set of response functions for which the metric at the top of the column meets the detectability criterion. The third entry, “Average Clearance Change for Detectable Wear,” is analogous to the corresponding entry in the table giving results for the eigenvalue-based metrics. Each average is taken over the threshold values obtained from all residues that met the detectability criterion.

In addition to the fact that a different number of modes is identified from the FRFs and dFRFs, the nature of a dFRF and features of the analytical model make the number of residues obtained from the dFRF data different from that for FRF data. The dFRF has meaningful, non-repetitive data over the whole  $-\omega_{\max}$  to  $\omega_{\max}$  frequency range. For an isotropic system, forward and backward modes are separated into the positive and negative frequency ranges, respectively, of the dFRF. Lee [38] and Joh and Lee [34] showed that for

**Table 14:** Performance of residue-based damage metrics for FRF and dFRF data.

Damage Metric	%Chng $\text{Re}(A_k)$	%Chng $\text{Im}(A_k)$	%Chng $ A_k $	Chng $\arg(A_k)$
<b>FRF Processing</b> (12 identified residues for 4 modes)				
Number/% of Modes Meeting Detectability Criterion	4/100%	2/50%	3/75%	2/50%
Number/% of Metrics Meeting Detectability Criterion	6/50%	7/58%	8/67%	5/42%
Ave. Clearance Change for Detectable Wear	39%	37%	27%	48%
<b>dFRF Processing</b> (19 identified residues for 3 modes)				
Number/% of Modes Meeting Detectability Criterion	1/33%	3/100%	2/67%	2/67%
Number/% of Metrics Meeting Detectability Criterion	5/26%	7/37%	4/21%	4/21%
Ave. Clearance Change for Detectable Wear	52%	46%	39%	61%

an anisotropic system, forward and backward modes make evident contributions in both the positive and negative frequency range of dFRFs. The system studied here is anisotropic due to the characteristics of the bearings. Modes that appear only once in the FRF are present twice in the dFRF, once each in the positive and negative frequency ranges. Consequently, the number of residues obtained from a complete set of input data will be greater for dFRF data than for the corresponding FRF data, even though the total number of discrete system modes identified is fewer for the dFRF data in this study.

For FRF data, the *percent change in  $\text{Re}(A_k)$*  metric detected increased clearance with each of the four modes identified by AMI. The metric detected increased bearing clearance with six of the twelve total residues identified. The average increase in bearing clearance required for detection was 39%. For dFRF data, the metric detected increased clearance only with the nominal system mode  $\lambda = -1.2569 + 5.4871i$ . Five of the nineteen separate residues estimated by AMI exhibited detectable wear. The average value of clearance increase from nominal for detection was 52%.

The *percent change in  $\text{Im}(A_k)$*  metric for FRF data detected wear with two of the four

modes identified by AMI. Seven of the twelve AMI-estimated residues showed detectable wear. A 37% increase in bearing clearance was the average required for detection. The same metric for dFRF data detected wear with all three of the modes detected by Two-Sided AMI processing, and there were seven occurrences of detectable wear in the nineteen identified residues. The average value of clearance increase required for detection was 46%.

With FRF data, the *percent change in  $|A_k|$*  metric detected wear with three of the four modes AMI processing of the FRF data returned. An average increase in clearance of 27% was required for detection. Eight of the twelve residues identified by AMI showed detectable wear. The corresponding dFRF data results for this metric indicated wear with two of the three modes found by Two-Sided AMI, at a 39% average increase in clearance. There were only four occurrences of detectable wear from the 19 total residues identified.

The fourth metric, *change in  $\arg(A_k)$* , detected wear with two of the four AMI modes returned from FRF data. Five of the twelve AMI-identified residues exhibited detectable wear. For dFRF data, this metric detected wear with two of three modes, and four of the nineteen total residues showed detectable wear. The average increases in bearing clearance required for defect detection with the metric were 48% for FRF data and 61% for dFRF data.

## 5.4 Discussion

The frequency domain response, in the forms of both standard frequency response functions (FRFs) and directional frequency response functions (dFRFs), was used to investigate the performance of eight damage metrics. The response described a mathematical model of a rotordynamic system comprised of one disk on a flexible shaft supported by plain journal bearings. Experimental modal analysis of the response data using the Algorithm of Mode Isolation (AMI) for FRF data and Two-Sided AMI for dFRF data yielded system modal parameters in terms of eigenvalues and associated residues. Four metrics described the behavior of the modal eigenvalues: percent change in the real part of the eigenvalue ( $\text{Re } \lambda_k$ ), percent change in the imaginary part of the eigenvalue ( $\text{Im}(\lambda_k)$ ), percent change in the magnitude of the eigenvalue ( $|\lambda_k|$ ), and change in the phase of the eigenvalue ( $\arg(\lambda_k)$ ).

The other metrics were the corresponding quantities based on modal residue factors ( $A_k$ ). These depend on the modal properties of the drive and measurement locations, so each mode might have several residue factors that indicate bearing wear. A system defect was said to be detectable with a metric if the change in the metric due to the presence of the defect was greater than the error in the AMI estimate of the metric. Bearing wear, modeled by axisymmetric clearance increase, was the defect examined, and the complete analysis was conducted at seven clearance values within the H8 close-running fit class. For each clearance value, a set of four FRFs and a set of four dFRFs were processed by AMI and Two-Sided AMI, respectively. Eigenvalues estimated from different FRFs in a data set for one clearance level, but describing the same mode, were averaged. Residues associated with each mode obtained from the various FRFs and dFRFs were tracked individually because their values for different drive / measurement locations are not the same.

The analytical solution of the model gave ten underdamped modes in the frequency range of interest. Application of original AMI or Two-Sided AMI to a specific FRF or dFRF data set led to identification of four or less modes, with the result that processing all data sets only indicated the presence of four modes. The high damping provided by the hydrodynamic bearings and the use of the bearing locations, at which many modes are unresponsive, as the only excitation and measurement points made it difficult to identify the other modes. The eigenvalue-based metrics performed poorly with the small set of identified modes. The maximum bearing clearance change was not detectable with three of the four eigenvalue-based metrics for both FRF and dFRF data. For the *percent change in*  $\text{Im}(\lambda_k)$  metric, increased clearance was detectable with two modes using FRF data. The same metric only detected increased clearance with the one mode that dominated system response, using dFRF data. In comparison, increased bearing clearance was detectable with all four of the residue-based metrics. These metrics detected wear from a greater number of modes than the eigenvalue-based metrics. For highly damped rotordynamic systems, such as the one investigated here, the residue-based metrics show promise due to the consistency with which the whole group of metrics detects bearing wear. This counters the slightly lower sensitivity of these metrics, as compared to the *percent change in*  $\text{Im}(\lambda_k)$

metric.

The residue-based metrics constructed with modal parameters estimated by AMI processing of FRF data were more sensitive, overall, than the corresponding metrics based on dFRF data. For the prototypical system, when bearing clearance was increased to a value 48% greater than nominal, all residue-based metrics detected the wear with FRF data. However, when processing dFRF data, the bearing clearance had to be increased to 60% greater than nominal for all metrics to detect the change. Furthermore, the most sensitive residue-based metric, *percent change in  $|A_k|$* , detected the clearance change at 26% increase in clearance with FRF data and at 39% increase with dFRF data. In this analysis no advantage was gained by using the dFRF-derived, residue-based damage metrics in addition to those residue-based metrics constructed from FRF data.

## CHAPTER VI

# EVALUATION OF EIGENVALUES AND RESIDUES FOR USE IN DETECTION OF A SHAFT CRACK

### 6.1 *Introduction*

EMA is a procedure that estimates modal parameters by processing experimentally measured response data of a time-invariant system. An idea central to EMA is that a system's response can be represented as a summation of the actions of the system's individual modes of vibration. Time-invariant systems have discrete modes, which are expressed in terms of eigenvalues and eigenvectors, so their responses can be represented in the form on which EMA routines are based. Conversely, eigenvalues and eigenvectors do not exist for the direct response of a time-varying system, although Floquet theory [53] indicates that there is an underlying mathematical structure that has a modal component. Response data from a properly-excited time-invariant system will be termed "modal" data, and response data from a time-varying system will be termed "non-modal."

This chapter explores the usage of EMA concepts for fault detection when the data that is processed is non-modal, taken from the prototypical system. Chapter IV employed EMA to identify the prototypical system, while Chapter V evaluated a scheme for bearing wear detection. In both cases, system response was measured in such a way as to ensure that the system was time-invariant, thereby providing valid data to the EMA routine AMI. The bearings supporting the rotor of the prototypical system are anisotropic, and the undamaged shaft is isotropic. Thus, the bearing stiffness and damping are constant, relative to the fixed ( $XYZ$ ) coordinate system, and the shaft stiffness is constant relative to both the fixed and the moving ( $xyz$ ) coordinate systems. Therefore, modal data, relative to the fixed coordinate system, was the only type of data processed in the studies. The presence of a shaft crack changes the characteristics of the prototypical system. The hydrodynamic

bearings remain anisotropic, and the cracked shaft becomes so. Relative to the fixed coordinate system, the shaft stiffness is a function of time. Relative to the moving coordinate system, the bearing stiffness and damping are functions of time. Consequently, the system properties are inherently time-dependent, so non-modal response data results from the choice of either coordinate system to measure response data.

Although it is recognized that the data are non-modal, the analysis proceeds in essentially the same fashion as those in the previous chapters. This means that EMA is performed on the non-modal response data of a time-varying system, in order to ascertain whether performing EMA on non-modal response data provides any worthwhile information for shaft crack detection. Extension of EMA to this type of data can be justified. Consider a system with an infinitesimally small shaft crack. Its response should be quite similar to that of the system in the uncracked configuration, for which the system is time-invariant from the perspective of the fixed coordinate system. As the shaft crack grows, the nature of the system is altered. The goal of the work is to develop a method for early detection of small cracks. It is reasonable to expect that the response data of a system with a small, but detectable, crack will have similar characteristics to the response data of an uncracked system.

Further justification of the work in this chapter comes from consideration of the operation of installed equipment. With a piece of equipment in its nominal condition, EMA processing of fixed coordinate system response data provides useful information and does not violate the requirements of the analysis method. If some counterpart to EMA, designed to process non-modal data, was available, the analyst monitoring the equipment would need to know when to swap algorithms. The introduction of the crack would, of course, signal the need to swap. The only way to know when the crack appears in the system would be to understand the effects the crack has on the response data and AMI output. Finally, it is useful to consider the actions that would be taken by most equipment operators if EMA processing of response data of a time-varying system were to become abnormal because the rotating shaft was cracked. Even if some non-modal analog of EMA existed, most equipment would be shut down for repair, due to the catastrophic potential of a shaft failure.

It is unlikely that equipment operators would swap to a different data processing method, continue to run the equipment, and monitor the size of the crack, once a shaft crack had been detected.

## 6.2 *Method Overview*

As a consequence of the time-varying nature of the system in the cracked shaft configuration, peaks in a frequency domain plot of the system’s response do not represent modes. However, AMI and Two-Sided AMI process all frequency domain data in the same manner, regardless of whether the data are modal or non-modal. In the following work, when EMA is conducted on non-modal data, care is taken to refer to prominent segments of a frequency response plot to which AMI fits data as “identified peaks” instead of “modes.” Note that the results of AMI and Two-Sided AMI processing of non-modal data are still referred to as “eigenvalues” and “residues” because that is what the algorithm addresses. The use of other terms would further complicate the presentation.

Six of the eight quantities used to construct damage metrics in Chapter V are also used in this analysis. The magnitude of the eigenvalue ( $|\lambda_k|$ ) and the phase of the eigenvalue ( $\arg(\lambda_k)$ ) are not used. The real and imaginary parts of the eigenvalue are most strongly affected by two unrelated properties: the relative size of stiffness and mass for the latter, and energy dissipation for the former. The quantities  $|\lambda_k|$  and  $\arg(\lambda_k)$  combine the independent effects of changes in  $\text{Re}(\lambda_k)$  and  $\text{Im}(\lambda_k)$ , and therefore may mask small changes in one quantity and add unnecessary complexity to the analysis. The real and imaginary parts of the residue, on the other hand, are not proportional to any system properties. New insight may be gained through the study of changes in  $|A_k|$  and  $\arg(A_k)$  in addition to changes in  $\text{Re}(A_k)$  and  $\text{Im}(A_k)$ .

The prototypical system is configured with a single shaft crack at midspan. The time domain response due to impulse excitation at one bearing is used to generate FRF and dFRF response data sets. These data sets are processed with AMI and Two-Sided AMI, respectively. A determination of detectability of the crack is made by comparing AMI’s output from processing the nominal condition data set and the cracked condition data set.



An important difference between the work in this chapter and the work presented in the previous chapters lies in this comparison of results for nominal and damaged cases. Previously, the prototypical system in the nominal condition was time-invariant in the fixed ( $XYZ$ ) coordinate system. AMI was used to process the response of the nominal system and provide estimates of the system eigenvalues and associated residues. To gain a measure of AMI's accuracy, the AMI-estimated eigenvalues and residues were compared with the analytical values of these quantities, available from the solution of the state space eigenvalue problem. In contrast, because the prototypical system in a cracked configuration is time-varying in both the fixed and moving ( $xyz$ ) coordinate systems, no analytical modal properties are available for comparison. This requires that the detectability analysis be altered.

The modification assumes that the accuracy of AMI remains constant throughout the analysis of a certain data type (clean, fixed coordinate system data, for example). AMI's accuracy for each damage metric is quantified from the response data of the system in the nominal condition. This yields estimates for eigenvalues and residues, according to AMI, for the uncracked case of the model. Because the model in the uncracked condition is time-invariant (in terms of body-fixed displacements), the analytical eigenvalues and residues of the nominal system can be computed. The absolute AMI estimation error for each damage metric (the difference between the quantity calculated with the analytical value and the quantity calculated with the AMI-estimated value) is averaged over all identified modes. The average estimation error is used to bound a range of absolute change in the quantity. If the presence of a defect produces a change in the quantity outside the area bounded by the average estimation error, the defect is termed detectable with that particular damage metric. If the resulting change in the quantity is inside the bounded area, the defect is not detectable with that metric. The Detectability Concepts section below explains this idea in greater detail. The four data types used in testing are: clean, fixed coordinate system data; noisy, fixed coordinate system data; and both clean and noisy moving coordinate system data. The specific calculations required to convert the clean, fixed coordinate system data analytical eigenvalues and residues to those associated with another data type are also

detailed in the Detectability Concepts section.

Analysis is conducted with clean data over a range of relative crack depths. The analysis is repeated with noisy data. Both FRF and dFRF data are evaluated.

### ***6.3 Detectability Concepts***

Graphical detectability analysis, like the procedure used in the bearing wear study with the simplified version of the prototypical system, is employed here also. A sample detectability plot is shown in Figure 16. The “quantity” ( $\text{Im}(\lambda_k)$ , for example) and the metric (change in the “quantity”) are plotted against relative crack depth in the same figure with different vertical axes. A “detectability band,” representing the uncertainty in the AMI estimate of the metric, is overlaid on the plot. For a defect to be “detectable,” the absolute change in the quantity due to the presence of a defect must be greater than the uncertainty in the AMI estimate of the quantity, as represented by the detectability band. The point at which the change exceeds the uncertainty is the threshold of detectability. A further condition of detectability enforced in the present work is that the plot of the change in the quantity must remain outside of, and trend away from, the detectability band as the magnitude of the defect increases.

#### **6.3.1 Calculation of Detectability Bands**

##### *6.3.1.1 Clean Data*

In order to provide a measure of defect detectability for the investigation of the effects of a shaft crack, the performance of AMI in the estimation of eigenvalues and residues for the prototypical system in the nominal condition is considered. The error in the AMI estimation of the quantities associated with the six damage metrics evaluated in the study is quantified as follows. AMI is used to extract eigenvalues and residues from the clean, fixed coordinate system response data of the nominal system. The absolute difference between an AMI-derived value and the corresponding analytical value is calculated for each quantity. (For example, the phase of the analytical residue is compared with the phase of the AMI-estimated residue.) These absolute differences are averaged over the number of identified modes, and the average values are used to bound the detectability bands. The

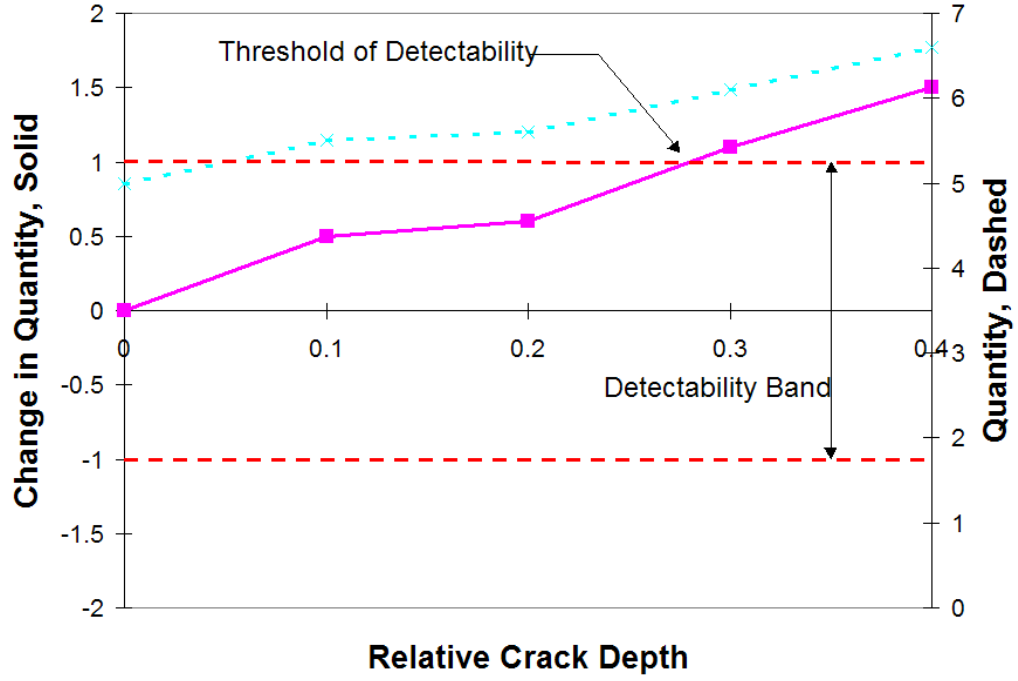


**Figure 16:** Sample detectability plot.

clean, fixed coordinate system values are shown in Table 15. The detectability bands for the damage metric related to a specific quantity appear as horizontal lines plotted on the “change in quantity” axis, at the values of + and – the average absolute estimation error values, as illustrated in Figure 16. For the analysis of shaft cracks of all relative depths, it is assumed that the accuracy of AMI is independent of crack depth.

The AMI estimation error for moving reference frame  $xyz$  data is calculated in the same manner, but the moving reference frame analytical eigenvalues and residues are used. To generate these moving reference frame analytical quantities, Bengisu’s [8] frequency domain mathematical relationship between the fixed reference frame FRFs and the moving reference frame FRFs is used.

$$\left\{ \begin{array}{c} H_{zz}(\omega) \\ H_{yz}(\omega) \end{array} \right\}_{move} = 1/2 \begin{bmatrix} 1 & 1 & -i & i \\ 1 & 1 & i & -i \end{bmatrix} \left\{ \begin{array}{c} H_{ZZ}(\omega - \Omega) \\ H_{ZZ}(\omega + \Omega) \\ H_{YZ}(\omega - \Omega) \\ H_{YZ}(\omega + \Omega) \end{array} \right\}_{fix} \quad (74)$$

The shaft speed is represented by  $\Omega$ . The fixed reference frame analytical frequency domain expression for the FRF (Eq. 16) is substituted into Eq. 74 to calculate the moving reference frame expressions for the FRF. The two-sided moving reference frame expression for the contribution of a single eigensolution to  $H_{zz}$  is given below for illustration.

$$H_{zz,move} = 1/2 \left[ \frac{A_{ZZ} - iA_{YZ}}{i(\omega - \Omega) - \lambda} + \frac{A_{ZZ}^* - iA_{YZ}^*}{i(\omega - \Omega) - \lambda^*} + \frac{A_{ZZ} + iA_{YZ}}{i(\omega + \Omega) - \lambda} + \frac{A_{ZZ}^* + iA_{YZ}^*}{i(\omega + \Omega) - \lambda^*} \right] \quad (75)$$

Substituting the known fixed reference frame analytical eigenvalues and residues into the right side of Eq. 75 yields the moving reference frame poles and residues. (Note that because  $\Omega$  is real, the poles are seen to shift by  $\pm\Omega$  parallel to the real axis.)

The moving reference frame analytical poles and residues for the dFRFs are calculated in a similar manner. Equation 21 demonstrates that the frequency domain expressions for the dFRFs can be calculated directly from the frequency domain expressions for the FRFs. This equation applies equally to fixed and moving reference frame values. Substituting the right side of Eq. 74 into Eq. 21 to represent the moving reference frame FRFs yields this equation for the moving reference frame dFRFs

$$\left\{ \begin{array}{c} H_{PG}(\omega) \\ H_{P\hat{G}}(\omega) \end{array} \right\}_{move} = 1/4 [T] \left\{ \begin{array}{c} H_{ZZ}(\omega - \Omega) \\ H_{ZZ}(\omega + \Omega) \\ H_{YZ}(\omega - \Omega) \\ H_{YZ}(\omega + \Omega) \\ H_{ZY}(\omega - \Omega) \\ H_{ZY}(\omega + \Omega) \\ H_{YY}(\omega - \Omega) \\ H_{YY}(\omega + \Omega) \end{array} \right\}_{move} \quad (76)$$

The matrix  $T$  is given by

$$T = \begin{bmatrix} 1-i & 1-i & 1-i & -1+i & 1+i & 1+i & 1+i & -1-i \\ -1+i & -1+i & -1+i & 1-i & 1+i & 1+i & 1+i & -1-i \end{bmatrix}. \quad (77)$$

Two manipulations of Eq. 76 are now required. First, substitute the pole-residue form of the FRF (Eq. 16), constructed with the moving reference frame analytical eigenvalues and

residues, for the FRFs on the right side of Eq. 76. Then, substitute the pole-residue form of the dFRF (Eq. 22) for  $H_{PG}$  and  $H_{P\hat{G}}$  on the left side of Eq. 76 to calculate the moving reference frame expressions for the dFRFs. The expression for  $H_{PG}$  is given below.

$$\begin{aligned}
H_{PG,move} = & \frac{1}{4} \left[ \frac{1}{i(\omega - \Omega) - \lambda} ((1 - i)(A_{ZZ} + A_{YZ}) + (1 + i)(A_{ZY} + A_{YY})) \right. \\
& + \frac{1}{i(\omega - \Omega) - \lambda^*} ((1 - i)(A_{ZZ}^* + A_{YZ}^*) + (1 + i)(A_{ZY}^* + A_{YY}^*)) \\
& + \frac{1}{i(\omega + \Omega) - \lambda} ((1 - i)A_{ZZ} + (-1 + i)A_{YZ} + (1 + i)A_{ZY} + (-1 - i)A_{YY}) \\
& \left. + \frac{1}{i(\omega + \Omega) - \lambda^*} ((1 - i)A_{ZZ}^* + (-1 + i)A_{YZ}^* + (1 + i)A_{ZY}^* + (-1 - i)A_{YY}^*) \right] \quad (78)
\end{aligned}$$

The known fixed reference frame analytical eigenvalues and residues are substituted into Eq. 78 to determine the moving reference frame poles and residues in the manner described previously for the FRF.

For each peak identified in AMI processing, the analytical eigenvalues and residues are compared with the AMI-estimated eigenvalues and residues for moving reference frame FRF and dFRF response data from the nominal system. The detectability band values (average absolute AMI estimation errors in the six damage metrics), for clean data signals in the moving  $xyz$  reference frame, are shown in Table 15. To indicate the magnitude of the quantity used in each damage metric, the absolute value of the analytical value of the quantity is averaged over the identified peaks and displayed in the “Mean of Absolute Analytical Value” columns.

### 6.3.1.2 Noisy Data

The same logic described above is used in the calculation of the detectability bands for noisy data. For the nominal system, the corresponding analytical and AMI-estimated values of the quantities associated with each of the six damage metrics are compared to develop a measure of the AMI estimation error. The fixed frame and moving frame analytical eigenvalues and residues, used in the clean data calculations, are also valid for the noisy data calculations. The AMI-estimated eigenvalues and residues come from processing frequency response data generated from nominal system time response data contaminated with Gaussian white noise. As before, the absolute AMI estimation errors are averaged

**Table 15:** Clean data detectability band values (estimation error of AMI and Two-Sided AMI for prototypical system in uncracked condition). Error values and absolute values of analytical quantities averaged over the identified peaks.

<i>Clean Data</i>	Fixed <i>XYZ</i>		Moving <i>xyz</i>	
Quantity	Detectability Band Values	Mean of Absolute Analytical Value	Detectability Band Values	Mean of Absolute Analytical Value
<i>AMI</i>				
$\text{Re}(\lambda_k)$	0.9	0.67	2.39	0.60
$\text{Im}(\lambda_k)$	0.38	19.78	0.95	14.57
$\text{Re}(A_k)$	0.17	0.12	0.19	0.06
$\text{Im}(A_k)$	0.15	0.05	0.32	0.05
$ A_k $	0.19	0.13	0.27	0.08
$\arg(A_k)$	1.4	1.5	1.32	2.1
<i>Two-Sided AMI</i>				
$\text{Re}(\lambda_k)$	3.1	0.67	2.8	0.67
$\text{Im}(\lambda_k)$	0.8	19.77	0.58	19.77
$\text{Re}(C_k)$	1.1	0.80	1.23	0.42
$\text{Im}(C_k)$	0.41	0.34	0.69	0.35
$ C_k $	0.43	0.88	0.56	0.52
$\arg(C_k)$	1.6	1.63	1.6	1.5

over all the identified modes in the frequency range of valid model performance.

Note that the presence of noise could lead to an individual estimate that is closer to the analytical value. To decrease the likelihood of the results being specific to the noise signature used, a noise confidence interval was calculated. With the prototypical system configured with a crack of 0.3 relative depth, the time domain response for an impulse was separately contaminated with two independent white noise signatures (termed *noise 1* and *noise 2*) to produce two sets of noisy response data. The resulting FRFs were independently processed with AMI, and the two associated sets of dFRFs were independently processed with Two-Sided AMI. The estimates for eigenvalues and residues were used to calculate two sets of the quantities associated with the damage metrics. The differences in the two sets of these quantities were then only related to the noise signature used to contaminate the time domain data. These absolute differences were averaged over the identified peaks and termed the noise confidence interval. The noise confidence interval is added to the average absolute estimation error calculated using the nominal system analytical eigenvalues and residues and

the noisy-signal AMI estimates of the nominal system eigenvalues and residues.

Due to the time consuming nature of the computations, only one additional noise signature, *noise* 2, was evaluated. Properly, these operations should have to be repeated for a statistically-significant number of noise signatures for one to be certain that the results are not related to the characteristics of a specific noise signature. It is possible that this simple method is greatly overestimating the effects of noise. The worst-case overestimation of the effects of noise is illustrated by the following non-rigorous example. The noise profiles have an average,  $\bar{x}$ , and a standard deviation,  $\sigma$ . If *noise* 1 is represented by  $\bar{x} + \sigma$ , the estimation error due to the presence of *noise* 1 is  $\bar{x} + \sigma$ . If *noise* 2 is represented by  $\bar{x} - \sigma$ , the difference in estimation error due to the differences in the noise profiles is  $(\bar{x} + \sigma) - (\bar{x} - \sigma) = 2\sigma$ . The detectability band resulting from the addition of the estimation error due to the presence of *noise* 1 ( $\bar{x} + \sigma$ ) to the noise confidence interval ( $2\sigma$ ) would then be  $\bar{x} + 3\sigma$ .

In summary, the steps performed to reduce the chances that the results are specific to a particular noise profile were

- Calculate the average absolute estimation error for each metric.
- Calculate the noise confidence interval for each metric.
- Add the two to get the detectability band values for each metric.

These resulting detectability band values for noisy data signals in the fixed *XYZ* and moving *xyz* reference frames are presented in Table 16.

## 6.4 *Measurement Noise Model*

Ericsson [18] developed a technique for automatic detection of defects in rolling element bearings. Simulation of noise added to the accelerometer signal to account for the proximity of other equipment was critical to validating the technique. Ericsson proved that Gaussian white noise is an acceptable model for this application. Additionally, measurement noise generated by a typical accelerometer is also Gaussian white noise [5], although the level is considerably lower than the noise level associated with an industrial setting. Following

**Table 16:** Noisy data detectability band values (estimation error of AMI and Two-Sided AMI, adjusted with noise confidence interval, for prototypical system in uncracked condition). Error values and absolute values of analytical quantities averaged over the identified peaks.

<i>Noisy Data</i>	Fixed <i>XYZ</i>		Moving <i>xyz</i>	
Quantity	Detectability Band Values	Mean of Absolute Analytical Value	Detectability Band Values	Mean of Absolute Analytical Value
<i>AMI</i>				
$\text{Re}(\lambda_k)$	1.55	0.67	2.7	0.60
$\text{Im}(\lambda_k)$	0.62	19.78	1.4	14.57
$\text{Re}(A_k)$	0.20	0.12	0.21	0.06
$\text{Im}(A_k)$	0.17	0.05	0.35	0.05
$ A_k $	0.21	0.13	0.32	0.08
$\arg(A_k)$	1.5	1.5	1.3	2.1
<i>Two-Sided AMI</i>				
$\text{Re}(\lambda_k)$	3.8	0.67	3.4	0.67
$\text{Im}(\lambda_k)$	1.5	19.77	1.24	19.77
$\text{Re}(C_k)$	1.23	0.80	1.33	0.42
$\text{Im}(C_k)$	0.54	0.34	0.84	0.35
$ C_k $	0.71	0.88	0.89	0.52
$\arg(C_k)$	1.2	1.63	1.4	1.5

Allen and Ginsberg [3], Gaussian white noise is added to the time domain response for noisy data analysis. The noise is scaled to have a standard deviation equal to 4% of the average of the maximum  $Z$  and  $Y$  direction displacements due to  $Z$ -direction impulse excitation of the prototypical system in its nominal condition. The same noise profile, defined as *noise* 1 in the previous section, is used in every analysis.

## 6.5 Time Domain Solution Procedure

The prototypical system in the cracked configuration is described by linear ordinary differential equations of motion with periodically time-varying coefficients. A frequency domain solution is not appropriate, so numerical integration in the time domain was performed.

Numerical integration is accomplished with the MATLAB ODE solver *ode15s*. The MATLAB [64] documentation and a reference text by Shampine *et al.* [61] provide detailed information on the use of *ode15s*. The recommended process for determining which MATLAB ODE solver to use calls for starting with *ode45*, which uses an explicit Runge-Kutta



method. If a trial run of the code shows that *ode45* can not perform the required integration efficiently, or at all, the next recommended step is to assume the problem is stiff and employ *ode15s*. This function is a variable order solver based on the Klopfenstein-Shampine family of numerical differentiation formulas. Most MATLAB ODE solvers accept ODEs expressed in the general form

$$M(t, y)\dot{y} = F(t, y). \quad (79)$$

Here,  $M(t, y)$  is a nonsingular matrix termed the mass matrix. The impulse response of the prototypical system is calculated as free vibration due to initial conditions, so there is no forcing function. The resulting expression of the state space formulation of the equations of motion for the prototypical system for use by *ode15s* is

$$[S(t)] \{\dot{x}\} = [R(t)] \{x\}. \quad (80)$$

See Eqs. 9 and 10 for the state space formulation and the  $R$  and  $S$  matrices.

Trial and error testing of the various MATLAB ODE solvers which were able to correctly integrate the problem without generating an error code showed that the *ode15s* function was the best choice, in terms of required processing time, for solution of the equations describing the prototypical system. The *MaxOrder* property of *ode15s* was set to 1. This limited the implicit solver to first order numerical differentiation. Initial testing showed that derivatives of second and higher orders often led to numerical instabilities in the time domain solution of the prototypical system.

With the numerical integration method of solution operating properly, but quite slowly for some test cases, a Floquet theory solution [53], [4] was investigated. Solving for the prototypical system's time response using Floquet theory was attractive in some respects. The computational time for the required matrix exponentiation would be less than the computational time required for numerical integration over the entire time record. However, formulating the Floquet theory solution was beyond the scope of the project and was not done.

## 6.6 Exponential Window for Time Response

The computer processing time required to generate prototypical system time domain data with a time record long enough to let the response decay to zero was found to be prohibitively long in many system configurations. Because it was desired to investigate a large number of configurations, an exponential window [23] was employed to decrease the total processing time required to obtain a simulation that could be properly transformed to the frequency domain. The computed time domain response of the prototypical system,  $\{q(t)\}$ , was modified in the following manner,

$$\{q_{\text{exp}}(t)\} = \exp\left(-\beta \frac{t}{T}\right) \{q(t)\} \quad (81)$$

where  $T$  is the length of the time window, and  $\beta$  is the exponential window coefficient. The selection of  $\beta$  is critical to the effectiveness of the exponential window. If  $\beta$  is too small, leakage in the FFT processing of the time domain data will lead to poor estimates of the modal properties from AMI processing. If the value of  $\beta$  is too large, valuable modal data may be unduly suppressed, making it impossible for AMI to extract. This is especially likely in the presence of a persistent noise signature.

AMI processing of the frequency domain representation of windowed response data is identical to that of non-windowed data. AMI returns estimates of the eigenvalues and associated residues. The residue estimates are unaffected by the use of the exponential window. As long as  $\beta$  is real, as it is in the present work, the AMI estimates for  $\text{Im}(\lambda)$  are also unaffected by the exponential window. The relationship between the AMI estimate for the eigenvalue, estimated by processing windowed experimental data, and the analytical eigenvalue shows that

$$\lambda_{\text{windowed}} = \lambda_{\text{analytical}} - \frac{\beta}{T} \quad (82)$$

If one wishes to evaluate the results in terms of natural frequencies and damping ratios, instead of the eigenvalues and residues, then the calculation of the natural frequency is done as shown in Eq. 24 and the damping ratio is calculated using Eq. 83. The damping ratio calculated from the estimate of the eigenvalue from AMI processing of the windowed data

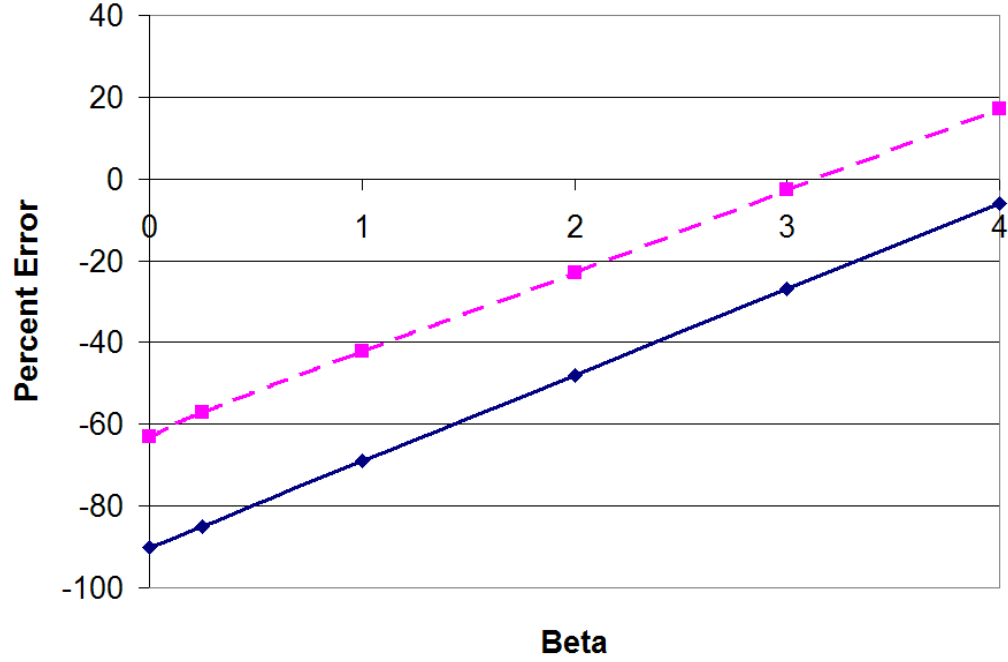


**Figure 17:** Percent error in AMI-estimated  $\text{Re}(\lambda)$  versus exponential window coefficient  $\beta$ . Solid =  $-1.2568 + i5.4879$  mode. Dashed =  $-1.2695 + i33.1281$  mode.

is represented by  $\zeta'$ , while the *actual* damping ratio is represented by  $\zeta$ .

$$\zeta = \zeta' - \left( \frac{\beta}{\omega_n T} \right) \quad (83)$$

The time domain response of the prototypical system in the nominal configuration was used to determine the optimum value of  $\beta$  for the analysis. The impulse response was calculated for a nondimensional time unit record of length  $T = 8$ , and windowed response data was calculated with values of  $\beta$  ranging from 0.5 to 8. Each set of windowed response data was converted to the frequency domain and processed with AMI. The AMI estimates for  $\text{Re}(\lambda_k)$  and  $\text{Im}(\lambda_k)$  for the  $-1.2568 + i5.4879$  mode and the  $-1.2695 + i33.1281$  mode were compared with the corresponding analytical values for each value of  $\beta$ . (These two modes were the most dominant modes in the response.) The percent error of the estimates is plotted against  $\beta$  in Figures 17 and 18. The value  $\beta = 3$  provided the best combination of error in  $\text{Re}(\lambda_k)$  and  $\text{Im}(\lambda_k)$  for both modes. Although different values of  $\beta$  may provide better performance at different damage states,  $\beta = 3$  is used throughout.

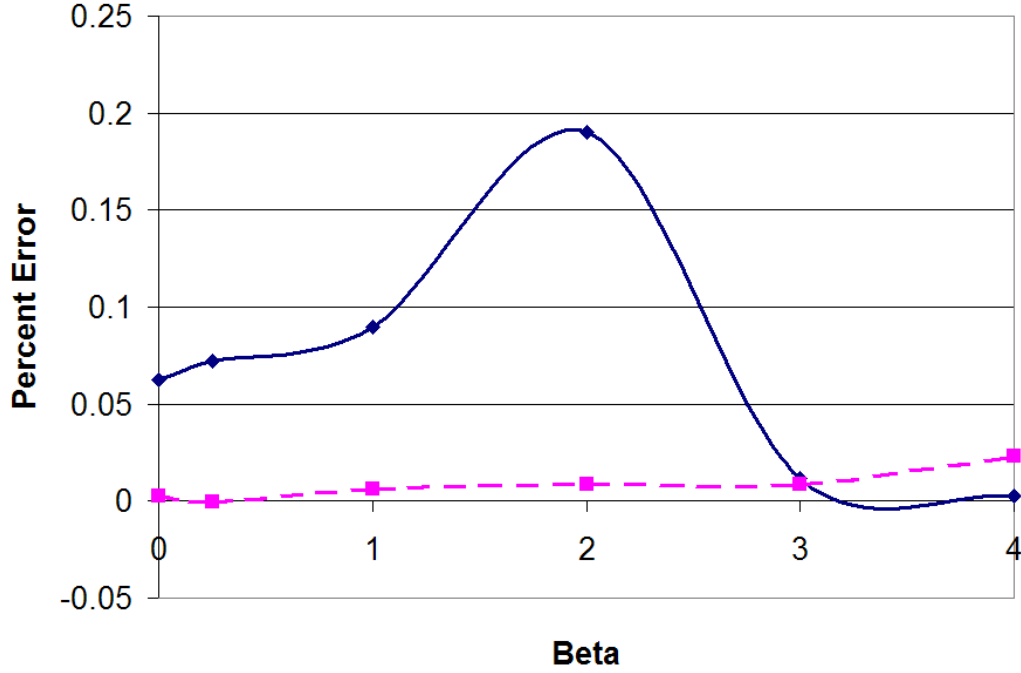


**Figure 18:** Percent error in AMI-estimated  $\text{Im}(\lambda)$  versus exponential window coefficient  $\beta$ . Solid =  $-1.2568 + i5.4879$  mode. Dashed =  $-1.2695 + i33.1281$  mode.

### 6.7 Valid Frequency Range of Prototypical System Model

When the crack depth is very small, the standard model describing a cracked shaft should have the same frequency response characteristics as the simplified model of the uncracked shaft. Testing this statement revealed an anomaly. The simplified model was solved in both the time domain and the frequency domain for the response to an impulse at the bearing closer to the disk, and the responses were identical. The frequency response from the time domain solution of the simplified model is presented in Figure 19. The uncracked standard model was solved in the time domain for the response to the same impulse. The frequency domain representation of the response is shown in Figure 20. The response of the uncracked standard model matched the response of the simplified model with respect to the location of poles over the 0 to 200 nondimensional frequency unit range. For frequencies below 40 nondimensional frequency units, the shapes of local minima and maxima in the two responses generally matched. The region between 40 and 60 nondimensional frequency

units was dominated by a local minimum, and there was poor agreement between the two responses. For frequencies above 60 nondimensional frequency units, the shapes of both the local minima and local maxima in the standard model response showed poor agreement with the shapes of the corresponding minima and maxima in the response of the simplified model.

The nature of a local minimum decreases the likelihood of an exact match between the responses of the standard and simplified models. Slight differences between the models could impact the cancellation required to form a minimum enough to produce corresponding local minima with significantly different shapes. Conversely, the summation required to form a maximum is not as sensitive to slight differences between the models. The differences between corresponding local maxima should not be as visually apparent as the potential differences in corresponding local minima.

The magnitudes of the local maxima were of the same order of magnitude for frequencies from 0 to approximately 60 nondimensional frequency units. Above 60 nondimensional frequency units, the magnitude of the response of the standard model of the prototypical system in the uncracked configuration was considerably greater than the magnitude of the response of the simplified model. The additional stiffness terms introduced into the model of the prototypical system to represent the shaft crack lose their effectiveness with increasing frequency. (This phenomenon is exhibited by the natural frequencies of a beam supported by a spring at one end. The higher-frequency modes in that case look like those of a free end.) For this reason, the standard model does not accurately represent the behavior of the uncracked system at higher frequencies. Consequently, the usable range of frequency response for the standard model of the prototypical system is restricted to 0 to 60 nondimensional frequency units.

In Chapter IV, AMI and Two-Sided AMI were used to identify the simplified model of the prototypical system. Of the four modes identified in this clean data testing, only one ( $\lambda = -1.4755 + 65.6800i$ ) was above the 60 nondimensional frequency unit limitation imposed on the standard model. In Chapter V, which also used the simplified model, very few instances of detectable bearing wear involved the ( $\lambda = -1.4755 + 65.6800i$ ) mode.

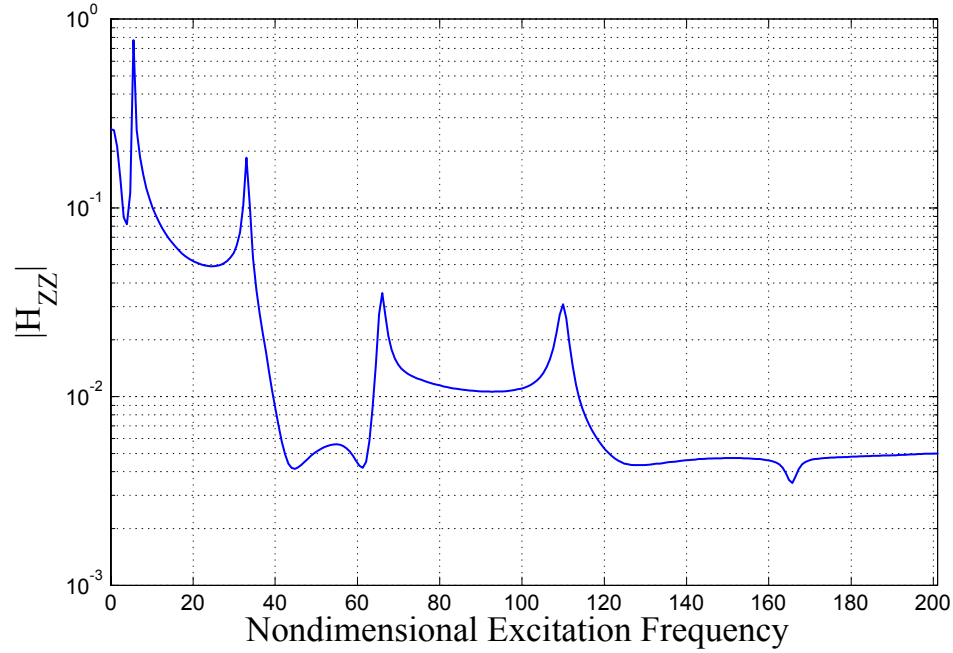


**Figure 19:** FRF  $H_{ZZ}$  of nominal system calculated from time domain response of simplified model of prototypical system.

The standard model of the prototypical system exhibits the characteristics of a cracked shaft through the use of a technique from the literature. The fact that the responses of the standard and simplified models do not match at higher frequencies does not detract significantly from the defect detection work presented here. The agreement between the responses in the lower-frequency range, where the majority of identifiable system modes is located, supports this. The goal of the development work was to create a cracked shaft model that would exhibit the relevant phenomena. Once this goal was met, an exhaustive numerical methods study to ensure better high-frequency agreement was not undertaken.

## 6.8 Analysis Method

The system is operated at a constant rotation rate of 1.35 nondimensional frequency units, which is between the first two critical speeds, 0.73 and 2.3 nondimensional frequency units. For each crack depth, system responses to both  $Y$ -direction and  $Z$ -direction impulses are required. The impulse excitation occurs at the bearing closer to the disk (Bearing 1), and

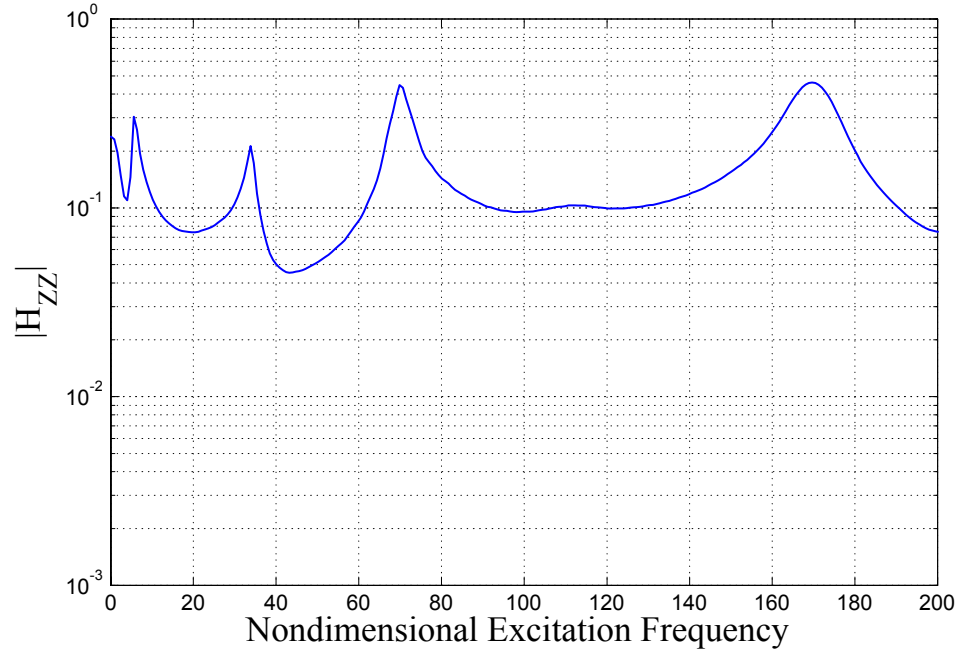


**Figure 20:** FRF  $H_{ZZ}$  of nominal system calculated from time domain response of standard model of prototypical system.

the equations, defined in the fixed coordinate system, are solved in the time domain. The moving coordinate system time domain response is calculated from the fixed coordinate system response as previously discussed. The responses to a given impulse are converted to the frequency domain, yielding FRFs for  $Y$ -direction and  $Z$ -direction response for fixed coordinate system data and FRFs for  $y$ -direction and  $z$ -direction response for moving coordinate system data. The parameters for the FFT calculations are  $T = 8$  nondimensional time units and  $N = 512$  sampling intervals. In order to avoid leakage, the previously described exponential window is used to increase the rate of decay of the response. The corresponding dFRFs are calculated from the FRFs. The FRF and dFRF data sets are processed independently by AMI and Two-Sided AMI.

After the response of the nominal system is calculated, the system is configured with one transverse crack located at midspan. The relative depth of this crack is increased in each successive analysis. The crack depths used in the investigation are shown in Table 17. The complete analysis is conducted first with clean time domain data and then repeated

with noise-contaminated data.

It is shown in the Results section that some peaks identified at one damage state are identified at some, but not all, following damage states. Other identified peaks are present in the response at each damage state. Due to these characteristics and the fact that no AMI data processing operation depends on previous work, each identified peak is tracked independently in these analyses.

**Table 17:** Shaft cracks used in analysis.

Relative Depth	Depth ( $m$ )
10%	0.008
20%	0.016
30%	0.024
40%	0.032

## 6.9 Results

### 6.9.1 Time Domain Response

Representative time domain responses are presented in this section. In each example, nondimensional displacement is plotted against nondimensional time. Time domain  $Z$ -direction response at Bearing 1 to a  $Z$ -direction impulse at Bearing 1 is shown in Figure 21. The prototypical system was in the nominal condition, and clean, unwindowed, fixed  $XYZ$  data is presented here. The corresponding  $Y$ -direction response at Bearing 1 to the same impulse excitation is shown in Figure 22.

The effect of noise on the time domain response is shown in Figure 23. The clean data shown in Figure 21 was contaminated with the previously defined noise profile.

The unwindowed responses in Figures 21 through 23 are nonzero at the end of the nondimensional time window shown. Computation time required for a decay to zero response was high for many system configurations investigated. The exponential window described in Section 6 was applied to the response so that leakage did not negatively impact the conversion to the frequency domain. A representative result is shown in Figure 24. Here, the exponential window was applied to the noisy fixed  $XYZ$  coordinate system time response shown in Figure 23, in preparation for conversion to frequency domain.



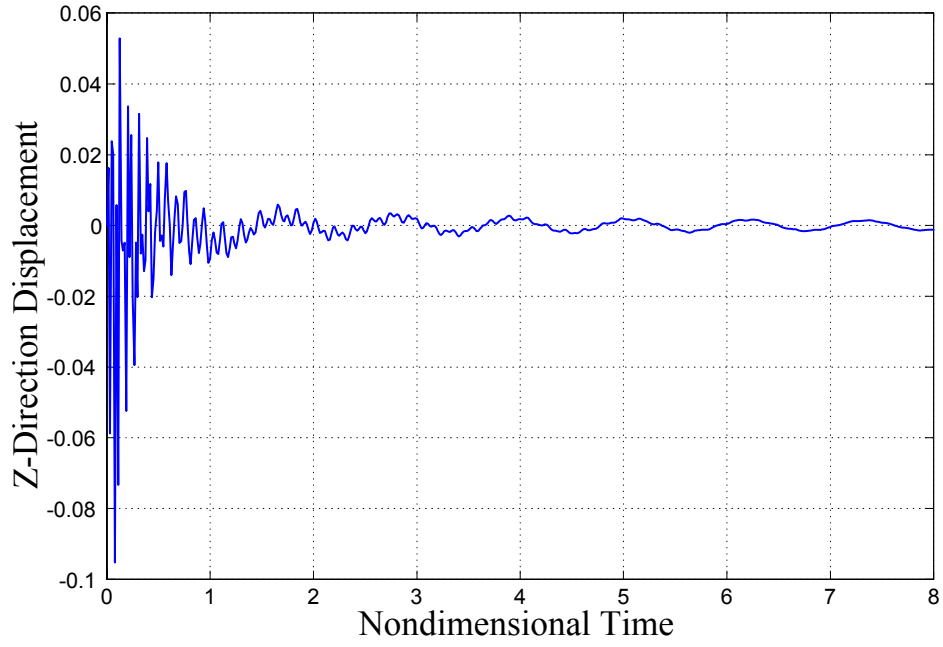


**Figure 21:** Z-direction response of nominal system at Bearing 1 due to Z-direction impulse at Bearing 1. Clean, unwindowed, fixed *XYZ* data.

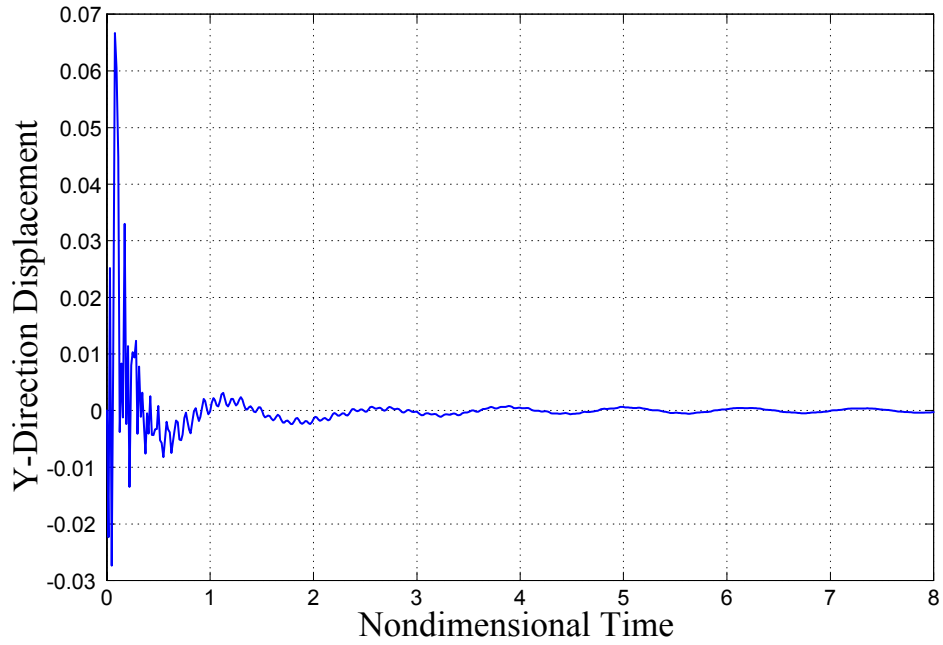


**Figure 22:** Y-direction response of nominal system at Bearing 1 due to Z-direction impulse at Bearing 1. Clean, unwindowed, fixed *XYZ* data.

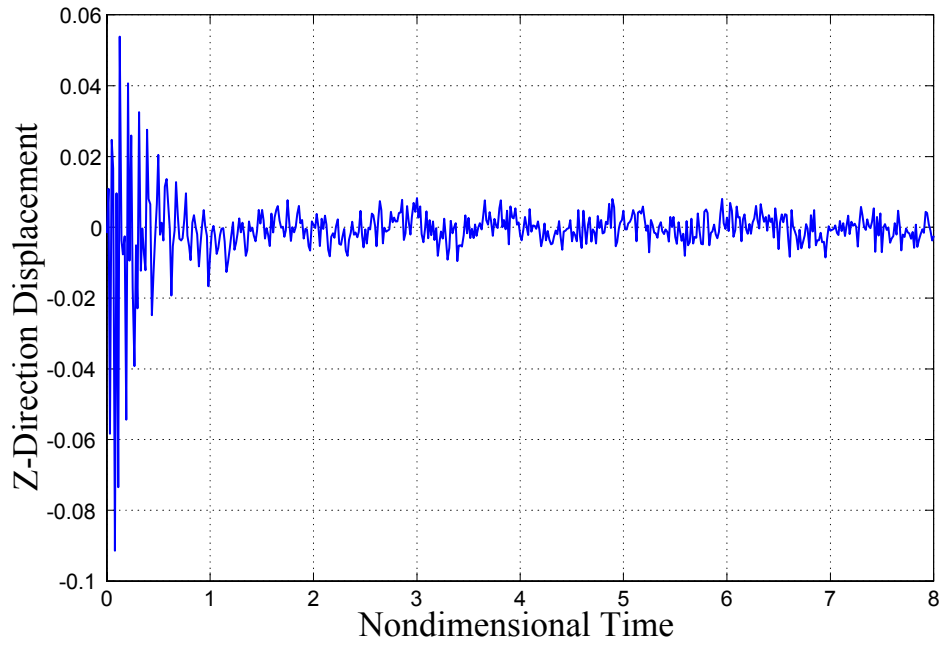


**Figure 23:**  $Z$ -direction response of nominal system at Bearing 1 due to  $Z$ -direction impulse at Bearing 1. Noisy, unwindowed, fixed  $XYZ$  data.

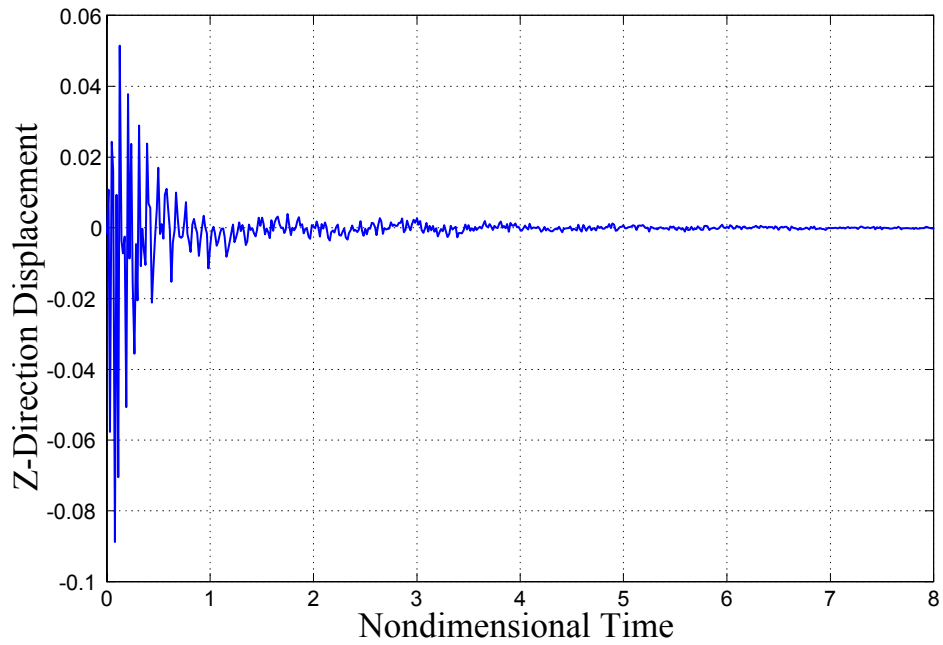


**Figure 24:**  $Z$ -direction response of nominal system at Bearing 1 due to  $Z$ -direction impulse at Bearing 1. Noisy, windowed, fixed  $XYZ$  data.

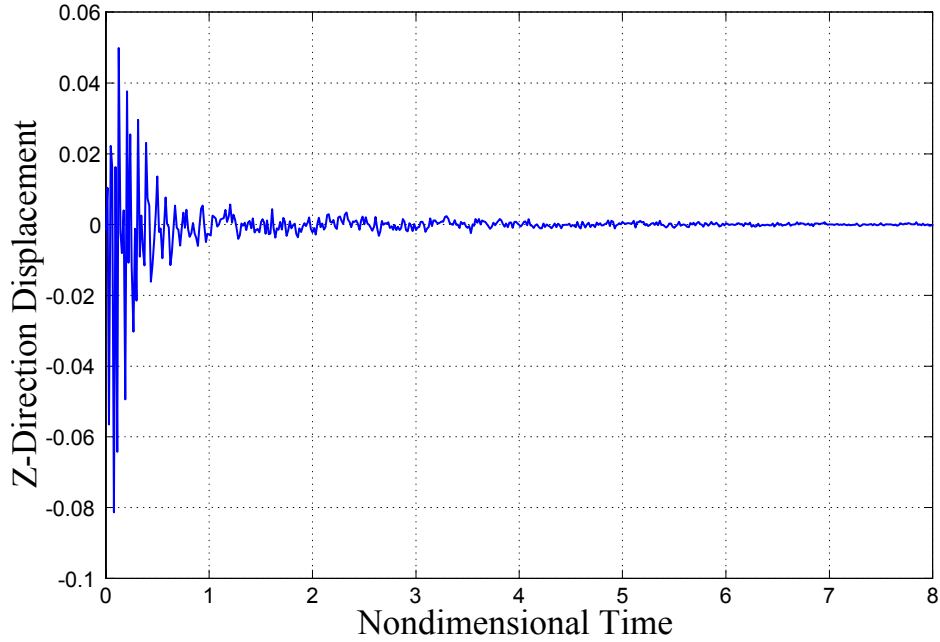


**Figure 25:**  $z$ -direction response of nominal system at Bearing 1 due to  $Z$ -direction impulse at Bearing 1. Noisy, windowed, moving  $xyz$  data.

The effect of using the moving  $xyz$  coordinate system is shown in Figure 25. The windowed, noisy, fixed  $XYZ$  data shown in Figure 24 was converted to the moving coordinate system. Changes in the response resulting from a conversion to the moving coordinate system are more evident in the frequency spectrum than in the time response.

The work in this chapter is based on processing response data of the prototypical system configured with a transverse shaft crack. The fixed  $XYZ$  coordinate system, noisy, exponentially windowed,  $Z$ -direction displacement at Bearing 1, due to a  $Z$ -direction impulse at Bearing 1, for the prototypical system with a crack of 0.4 relative depth is shown in Figure 26. The corresponding moving  $xzy$  coordinate system time response is shown in Figure 27.

### 6.9.2 Frequency Domain Response

Representative FRFs and dFRFs are presented in this section. Clean, windowed, fixed  $XYZ$  coordinate system response data for the nominal system is shown in the frequency domain as the  $H_{ZZ}$  FRF in Figure 28. The  $Z$ -direction response at Bearing 1 was due to

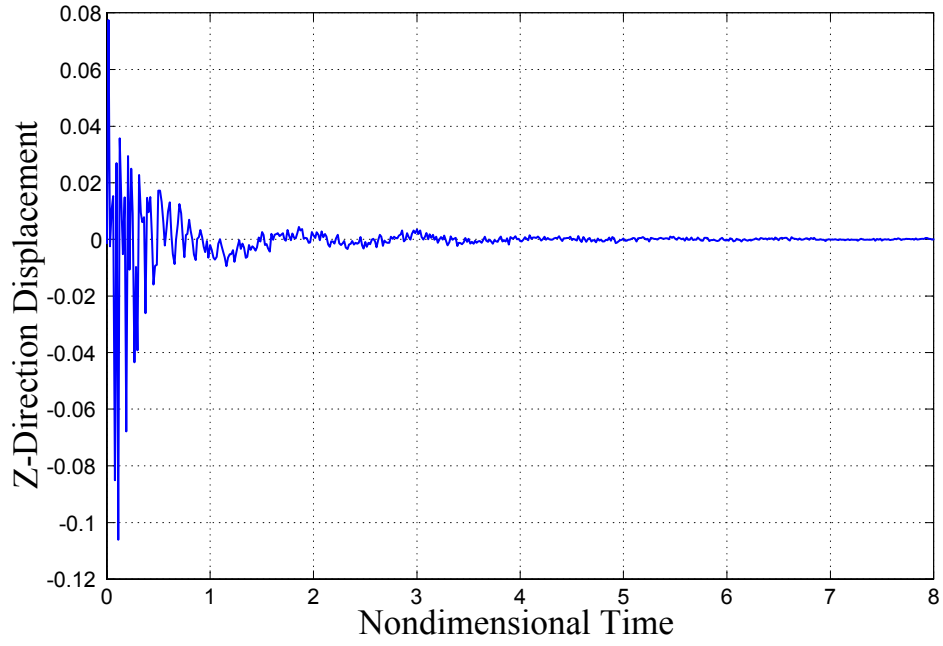


**Figure 26:**  $Z$ -direction response at Bearing 1, due to  $Z$ -direction impulse at Bearing 1, of system with crack of 0.4 relative depth. Noisy, windowed, fixed  $XYZ$  data.

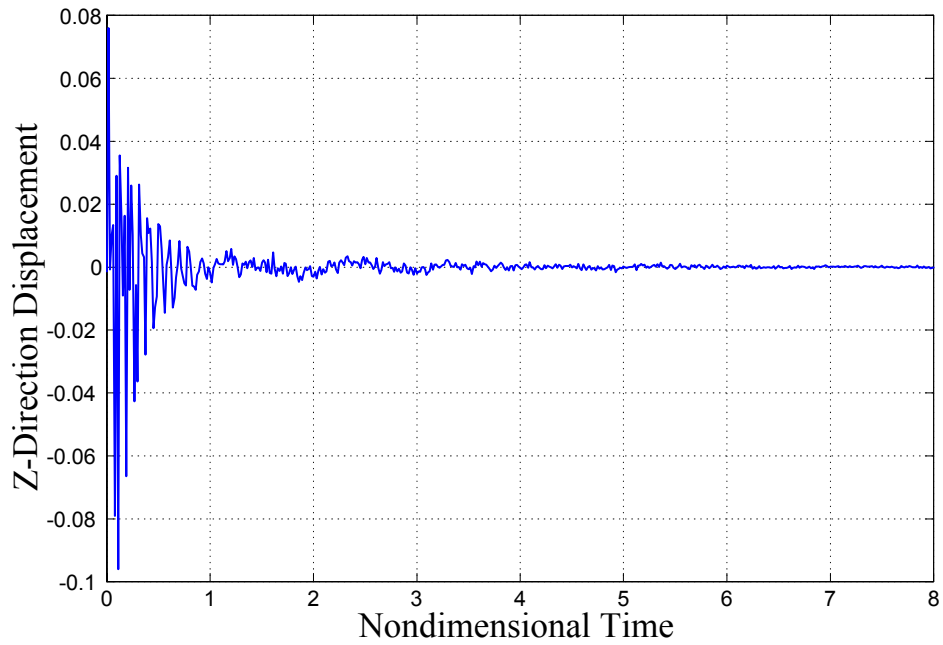


**Figure 27:**  $z$ -direction response at Bearing 1, due to  $Z$ -direction impulse at Bearing 1, of system with crack of 0.4 relative depth. Noisy, windowed, moving  $xyz$  data.

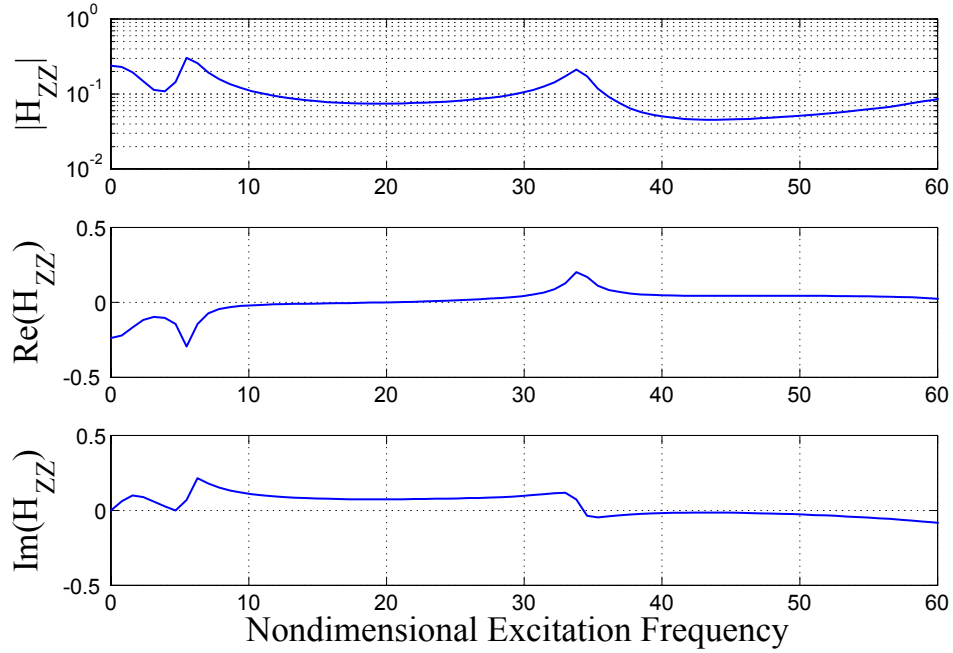


**Figure 28:** FRF  $H_{ZZ}$  of nominal system at Bearing 1, due to impulse at Bearing 1. Clean, windowed, fixed  $XYZ$  data

a  $Z$ -direction impulse at Bearing 1. The top plot in the figure is the magnitude of  $H_{ZZ}$  versus nondimensional frequency. The real and imaginary parts of  $H_{ZZ}$  are plotted versus nondimensional frequency in the middle and bottom plots in the figure. This format is used for all figures in this section. Note that the plots only display data inside the frequency range where the model is estimated to be valid (0 to 60 nondimensional frequency units), as defined previously.

The clean data, fixed coordinate system, normal dFRF,  $H_{PG}$ , and reverse dFRF,  $H_{P\hat{G}}$ , for the nominal system with excitation and response at Bearing 1 are shown in Figures 29 and 30.

The effects on the FRF and dFRF of converting from the fixed  $XYZ$  coordinate system to the moving  $xyz$  coordinate system are illustrated next. The clean, fixed coordinate FRF and dFRFs in Figures 28 through 30 were converted to the moving coordinate system. The moving coordinate system  $H_{ZZ}$ ,  $H_{PG}$ , and  $H_{P\hat{G}}$  are in Figures 31, 32, and 33, respectively.

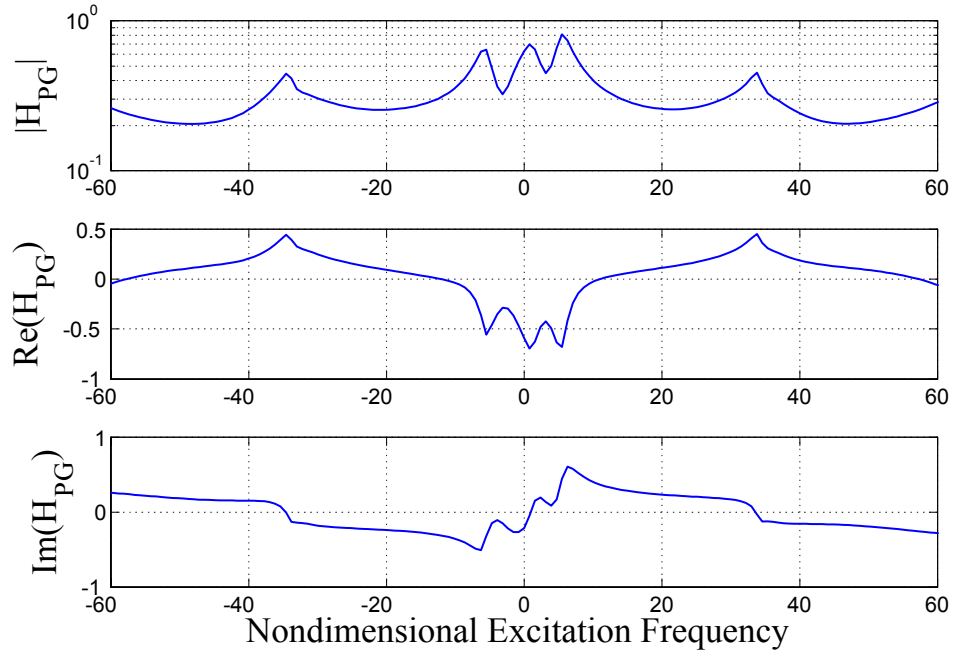


**Figure 29:** dFRF  $H_{PG}$  of nominal system at Bearing 1, due to impulse at Bearing 1. Clean, windowed, fixed  $XYZ$  data

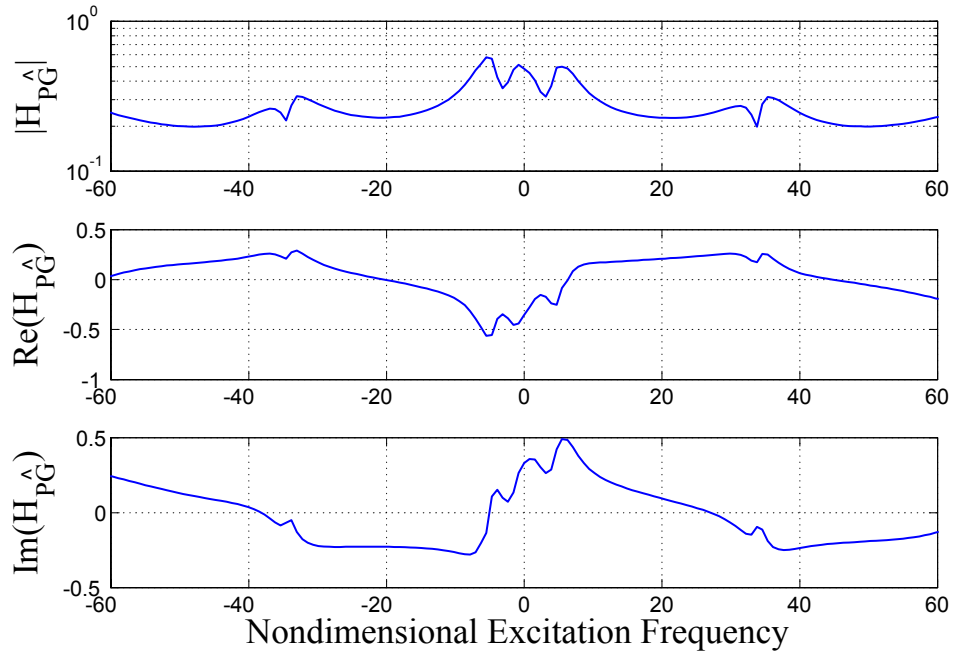


**Figure 30:** dFRF  $H_{PG\hat{}}$  of nominal system at Bearing 1, due to impulse at Bearing 1. Clean, windowed, fixed  $XYZ$  data

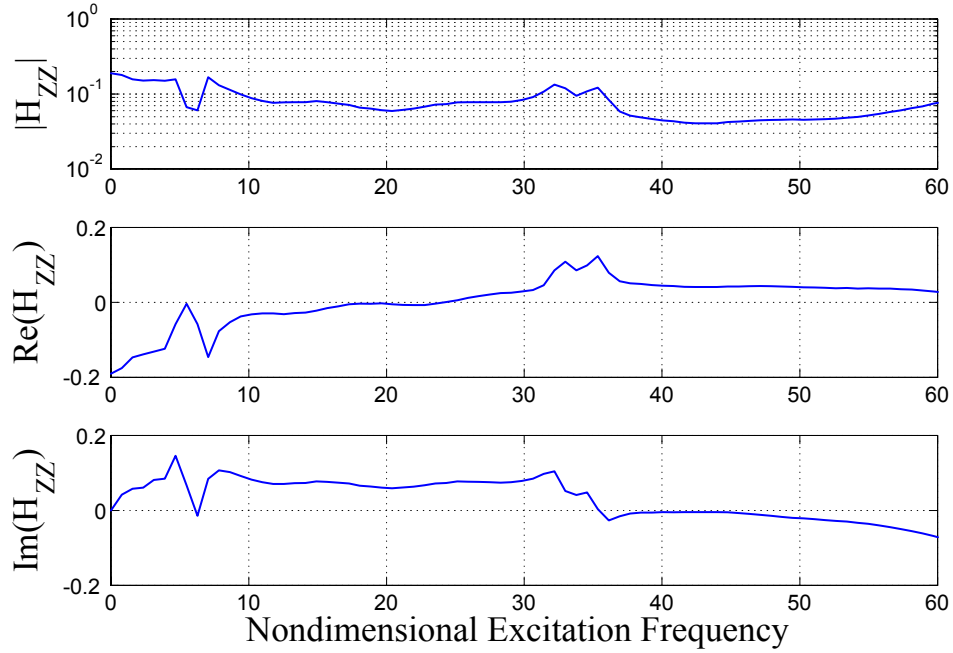


**Figure 31:** FRF  $H_{ZZ}$  of nominal system at Bearing 1, due to impulse at Bearing 1. Clean, windowed, moving  $xyz$  data

The shaft speed (1.35 nondimensional frequency units) is low compared to most nondimensional excitation frequency values at which peaks exist. A consequence of this, and of the high levels of system damping, is that the two distinct peaks in the moving coordinate system associated with one peak in the fixed coordinate system (see Table 2) appear as one peak with a width greater than that of its fixed coordinate system counterpart.

The contamination of time domain response data with noise produced changes in the FRF and dFRFs. The noisy data FRF and dFRF companions to the clean data, fixed  $XYZ$  coordinate system response data for the nominal system shown in Figures 28 through 30 are presented in Figures 34 through 36. The visual changes to the frequency response were similar for all data sets. The effects of noise on AMI and Two-Sided AMI processing of FRFs and dFRFs are quantified later in this section.

The transverse shaft crack introduced changes to the FRF and dFRF that were evident not only in AMI processing, but also during visual inspection in some cases. The most notable effects in one or more of the three subplots (magnitude, real part, and imaginary

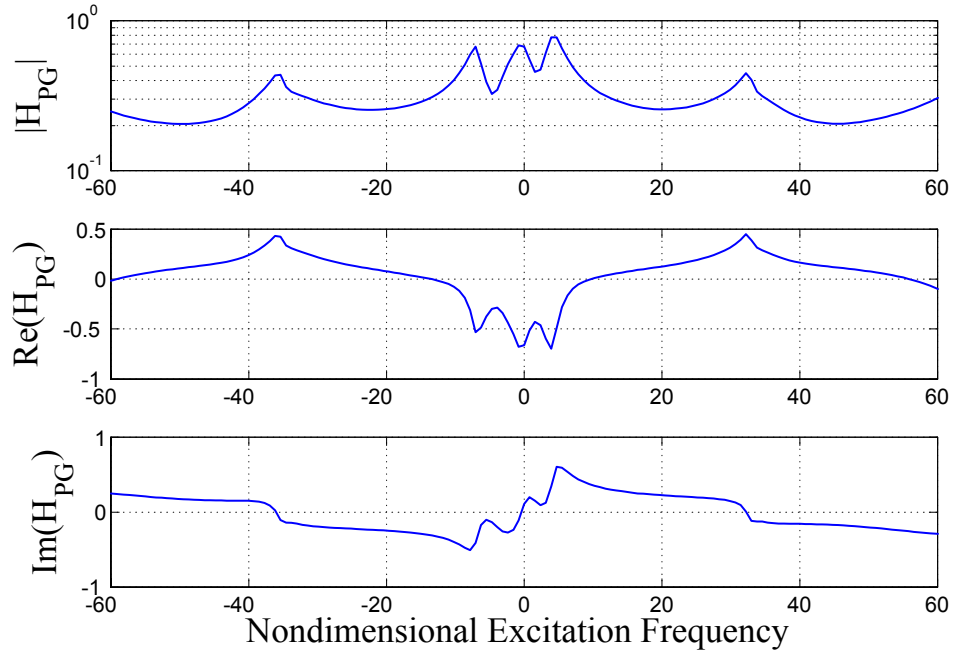


**Figure 32:** dFRF  $H_{PG}$  of nominal system at Bearing 1, due to impulse at Bearing 1. Clean, windowed, moving  $xyz$  data

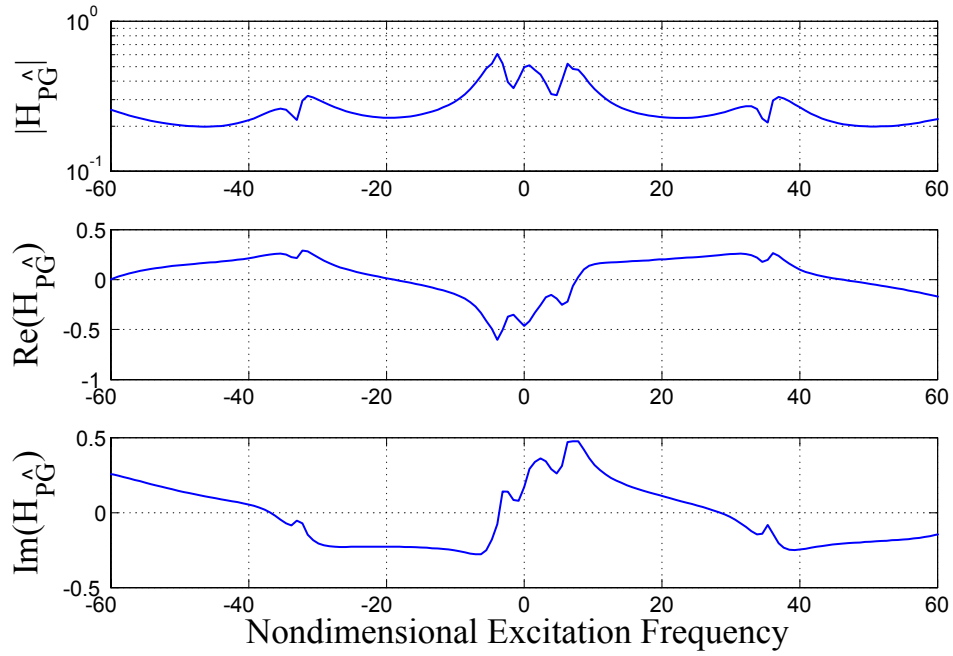


**Figure 33:** dFRF  $H_{PG}$  of nominal system at Bearing 1, due to impulse at Bearing 1. Clean, windowed, moving  $xyz$  data



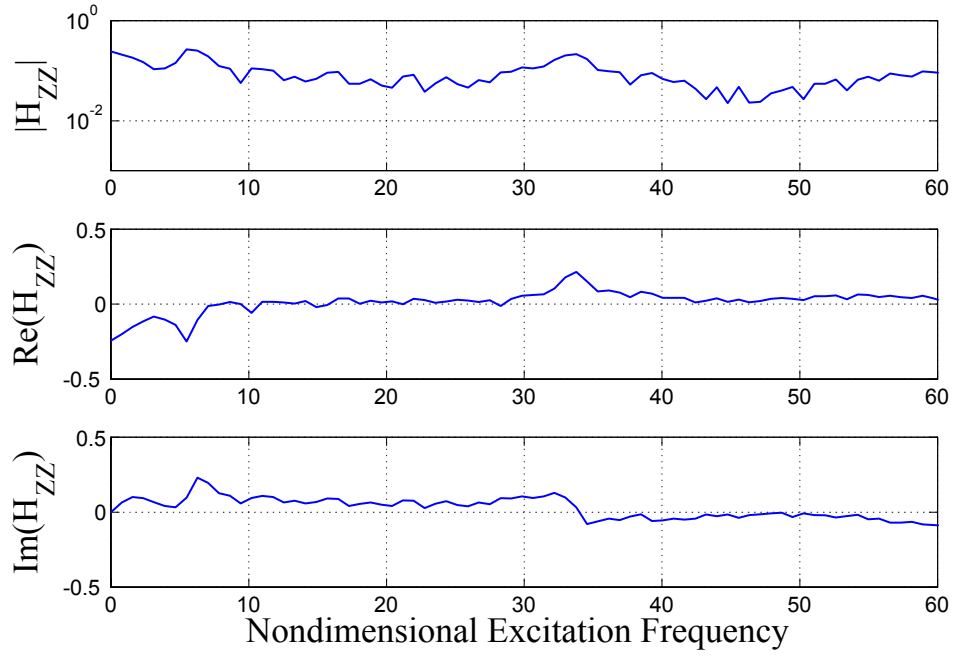


**Figure 34:** FRF  $H_{ZZ}$  of nominal system at Bearing 1, due to impulse at Bearing 1. Noisy, windowed, fixed  $XYZ$  data

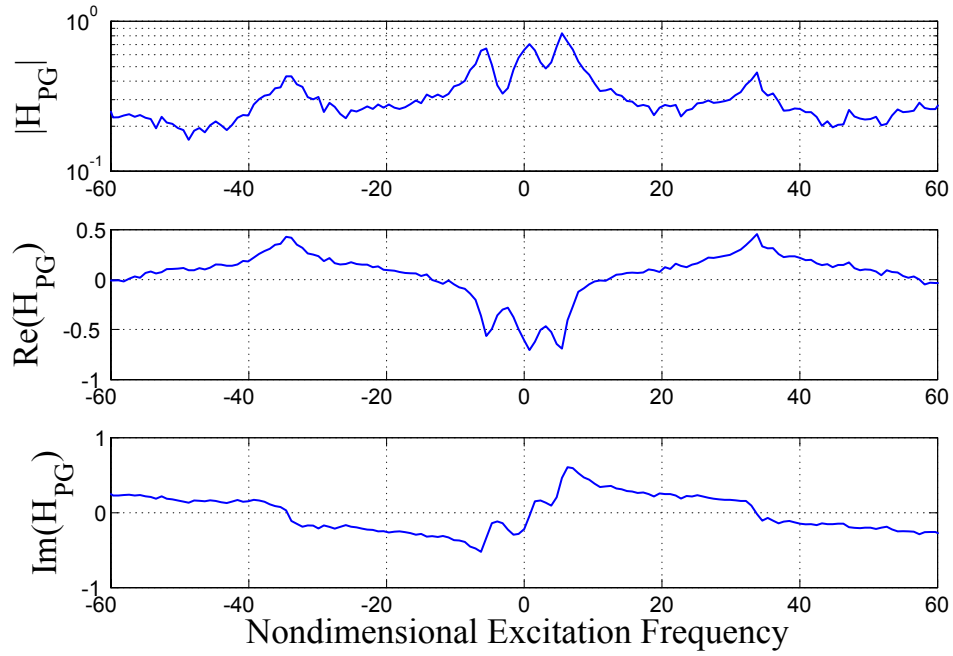


**Figure 35:** dFRF  $H_{PG}$  of nominal system at Bearing 1, due to impulse at Bearing 1. Noisy, windowed, fixed  $XYZ$  data

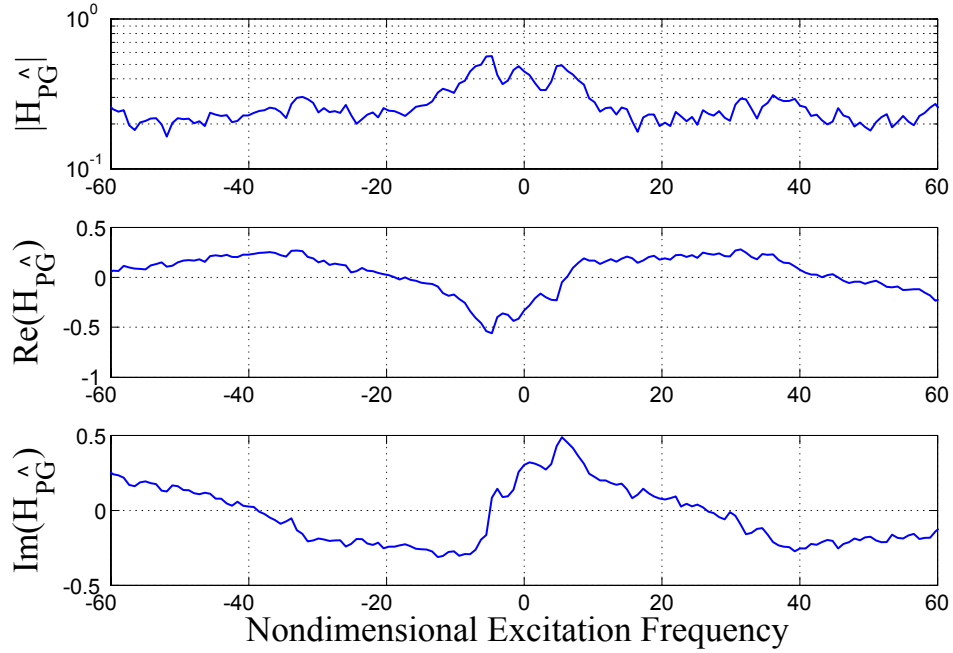


**Figure 36:** dFRF  $H_{PG}^{\wedge}$  of nominal system at Bearing 1, due to impulse at Bearing 1. Noisy, windowed, fixed  $XYZ$  data

part) are illustrated with the following examples. Figures 37, 38, and 39 show noisy data  $H_{ZZ}$ ,  $H_{PG}$ , and  $H_{PG}^{\wedge}$  in the fixed  $XYZ$  coordinate system for the prototypical system with a crack of 0.2 relative depth. The corresponding plots for the nominal system were previously introduced in Figures 34, 35, and 36. Figures 40, 41, and 42, show the same quantities for the prototypical system with a 0.4 relative depth crack. The only change visually evident in the subplots associated with the FRF  $H_{ZZ}$  was a slight increase in both  $|H_{ZZ}|$  and  $\text{Re}(H_{ZZ})$ , in the region above 30 nondimensional frequency units, with increasing crack depth. In the  $|H_{PG}|$  subplot, the heights of the peaks at approximately  $\pm 5$  and  $\pm 33$  nondimensional frequency units increased, relative to the peak at approximately 1 nondimensional frequency unit, with increasing crack depth. The same effect was seen in the  $|H_{PG}^{\wedge}|$  subplot with increasing crack depth.

### 6.9.3 Detectability Plots

Representative detectability plots are presented in this section. Figure 43 shows the damage metric *change in*  $\text{Re}(A_k)$  plotted versus relative crack depth for the FRF  $H_{ZZ}$  estimated

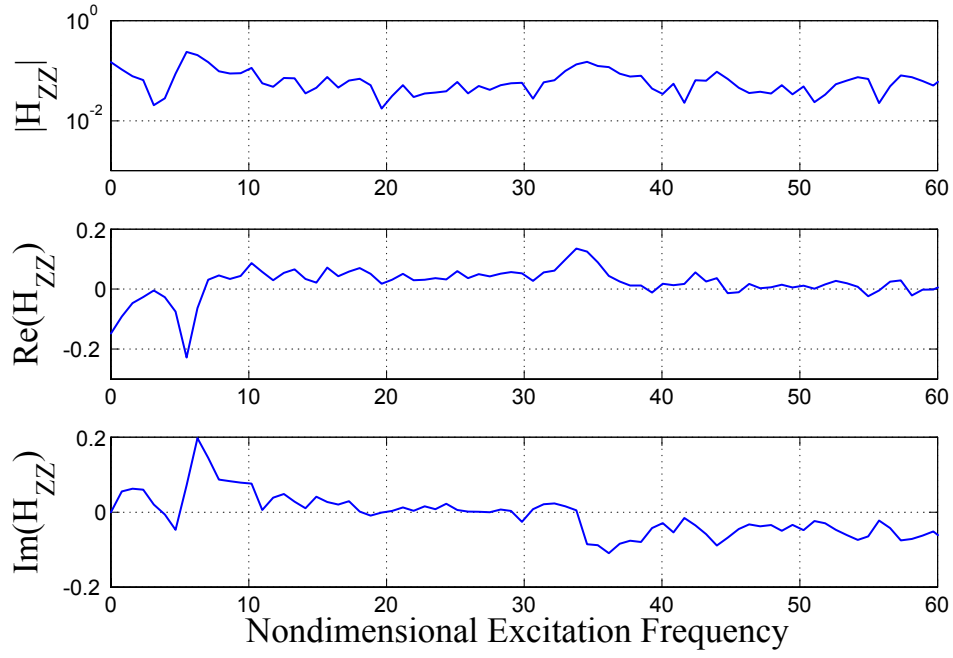


**Figure 37:** FRF  $H_{ZZ}$  at Bearing 1, due to impulse at Bearing 1, for system with crack of 0.2 relative depth. Noisy, windowed, fixed  $XYZ$  data.

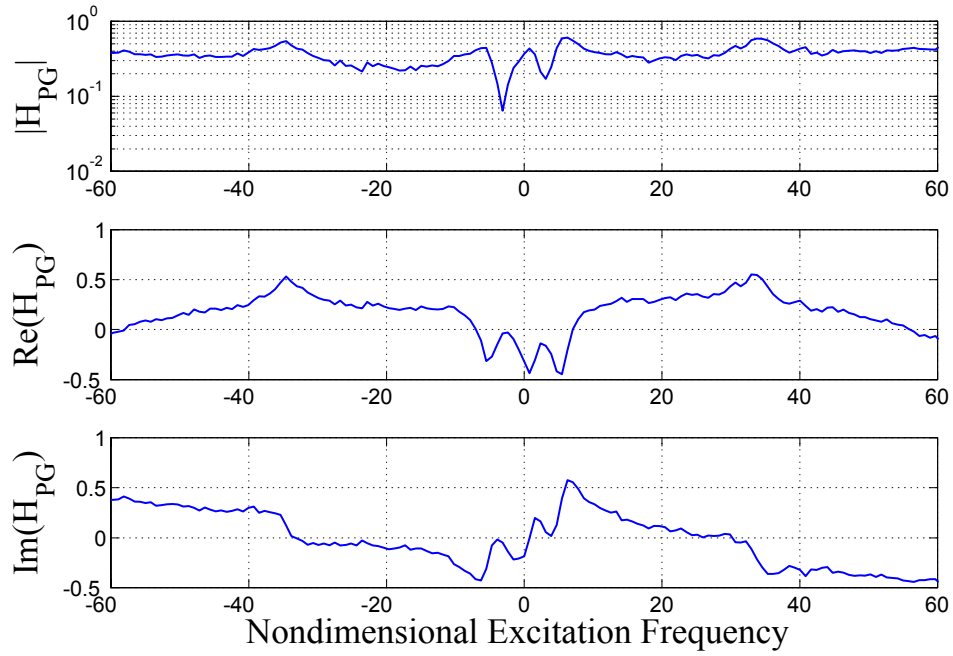


**Figure 38:** dFRF  $H_{PG}$  at Bearing 1, due to impulse at Bearing 1, for system with crack of 0.2 relative depth. Noisy, windowed, fixed  $XYZ$  data.

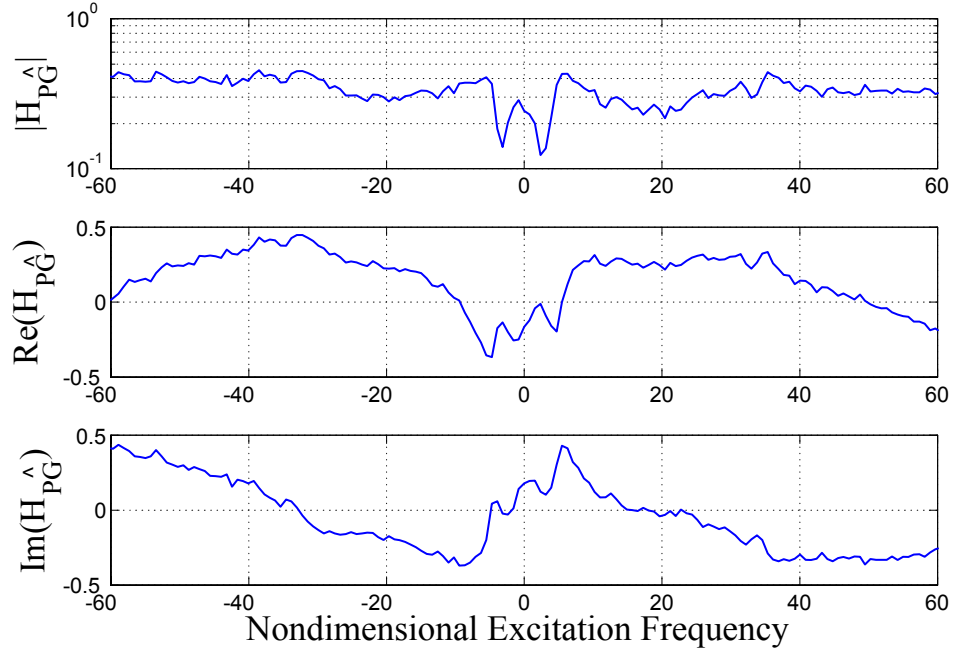


**Figure 39:** dFRF  $H_{PG}^A$  at Bearing 1, due to impulse at Bearing 1, for system with crack of 0.2 relative depth. Noisy, windowed, fixed  $XYZ$  data.

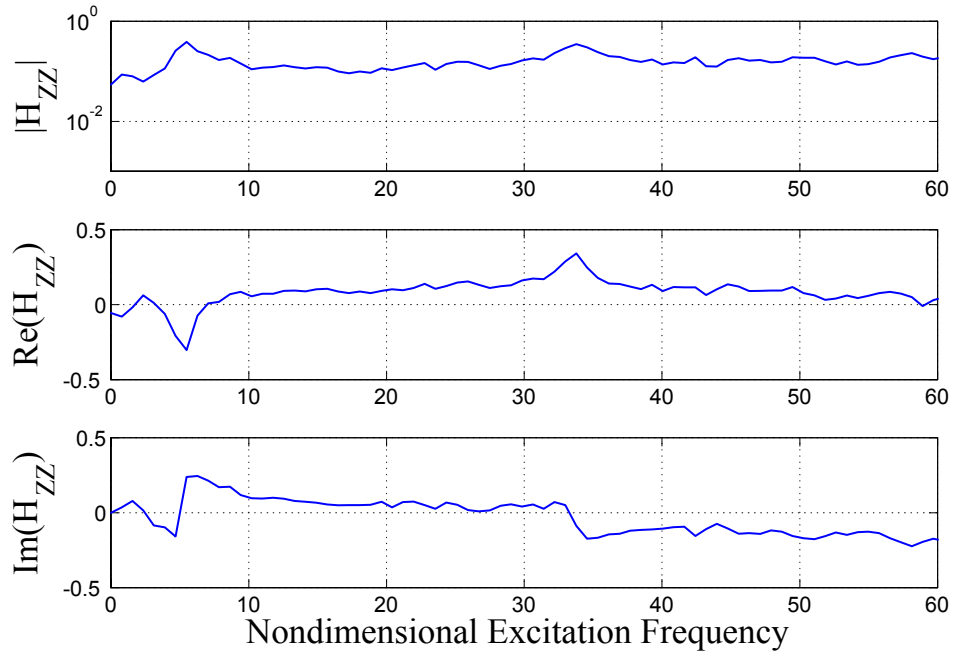


**Figure 40:** FRF  $H_{ZZ}$  at Bearing 1, due to impulse at Bearing 1, for system with crack of 0.4 relative depth. Noisy, windowed, fixed  $XYZ$  data.

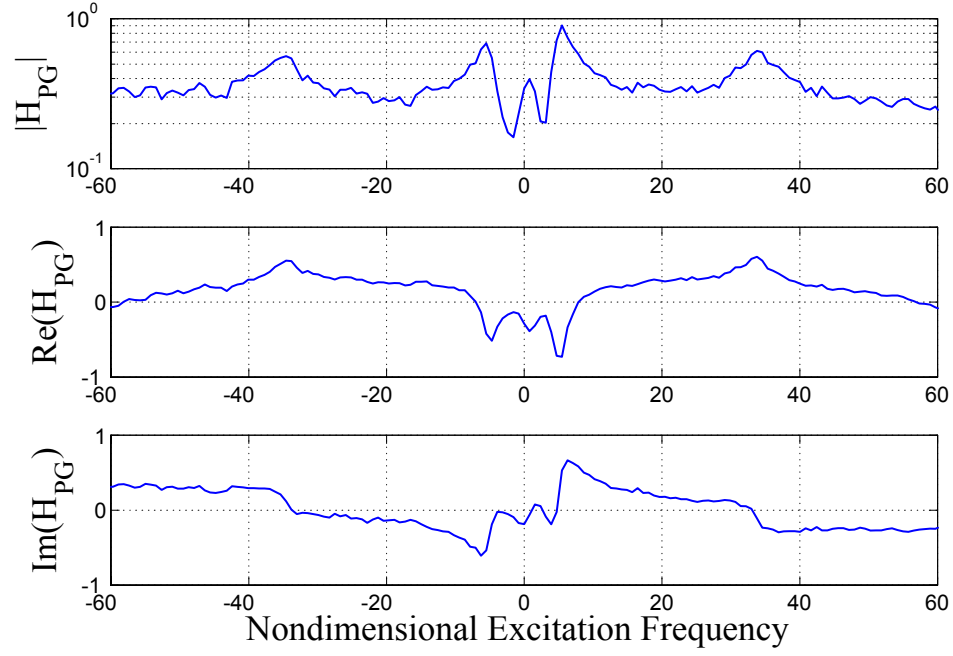


**Figure 41:** dFRF  $H_{PG}$  at Bearing 1, due to impulse at Bearing 1, for system with crack of 0.4 relative depth. Noisy, windowed, fixed  $XYZ$  data.

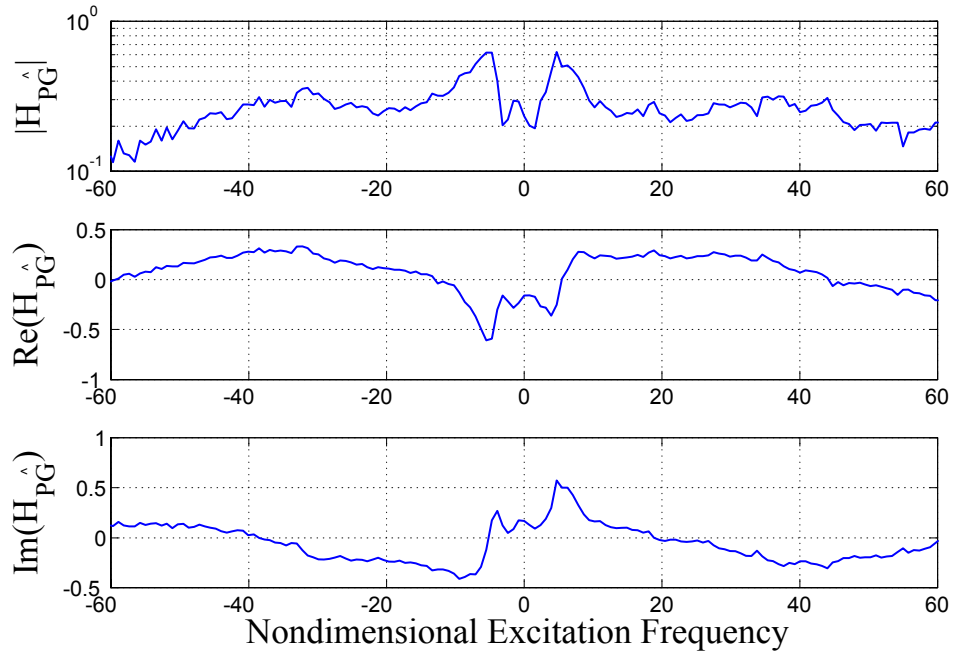


**Figure 42:** dFRF  $H_{PG}^{\wedge}$  at Bearing 1, due to impulse at Bearing 1, for system with crack of 0.4 relative depth. Noisy, windowed, fixed  $XYZ$  data.

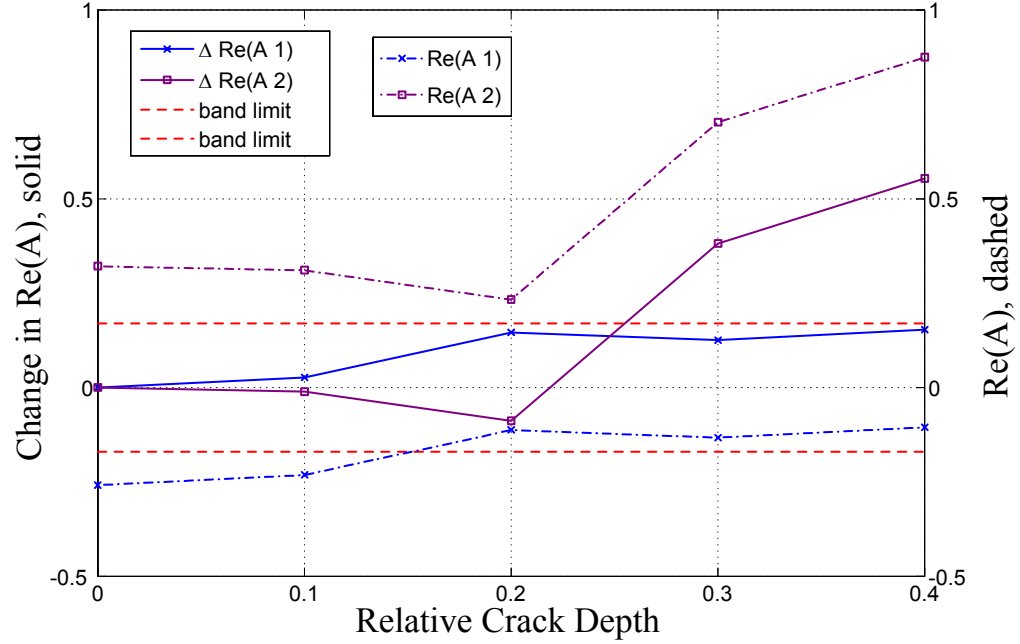


**Figure 43:** Detectability chart for  $\text{Re}(A)$ . FRF  $H_{ZZ}$  constructed with clean, fixed  $XYZ$  coordinate system data. Horizontal dashed lines are detectability band limits.

by AMI with clean, fixed  $XYZ$  coordinate system data. For this metric, the crack was detectable with identified peak 2 ( $\text{Im}(\lambda) \approx 33$ ). The plot for peak 2 crossed the detectability band at 0.3 relative crack depth and trended away from the detectability band with increasing crack depth. The plot for peak 1 ( $\text{Im}(\lambda) \approx 5$ ) did not cross the detectability band.

Figure 44 illustrates an instance where application of a metric would not lead to detection of a crack. The change in the imaginary part of the eigenvalue for (negative frequency range) peaks identified by Two-Sided AMI processing of dFRF  $H_{PG}$  remained inside the detectability band for all crack depths investigated.

The *change in*  $\text{Im}(\lambda_k)$  (for negative frequency range peaks) is shown for the fixed coordinate system dFRF  $H_{PG}$  for clean and noisy data in Figures 45 and 46, respectively, to illustrate the effect of time domain noise on detectability. With the introduction of noise, the overall number of identified peaks dropped from 4 to 3 and the number of peaks for which the crack is detectable dropped from 2 to 1. Many, but not all, combinations of

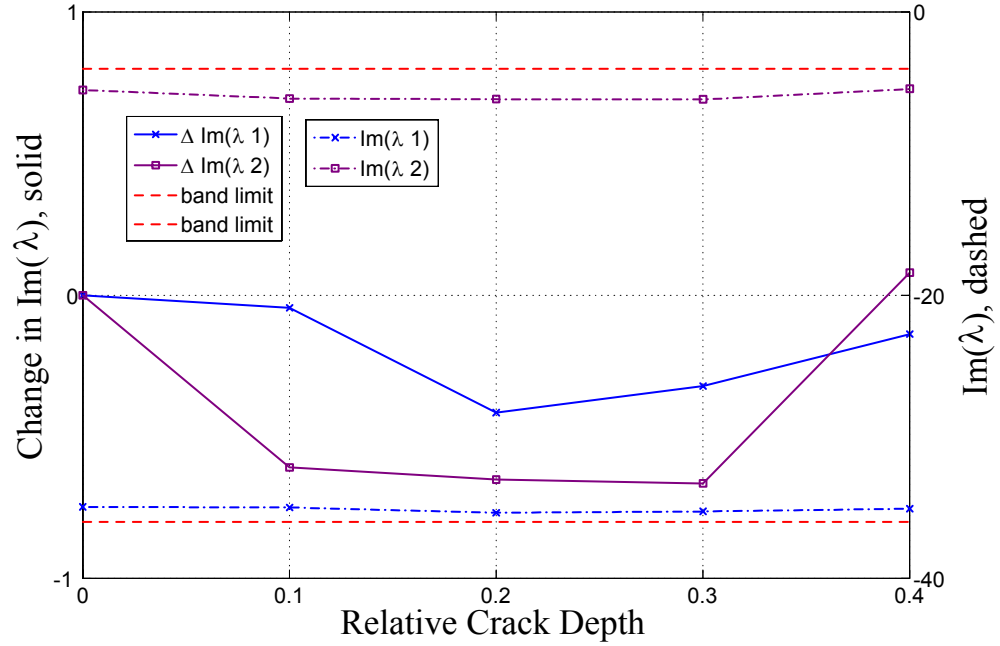


**Figure 44:** Detectability chart for  $\text{Im}(\lambda)$ . Negative frequency range dFRF  $H_{PG}$  constructed with clean, fixed  $XYZ$  coordinate system data. Horizontal dashed lines are detectability band limits.

data format and damage metric exhibited this behavior. Note that in Figure 45, while the curve for  $\lambda_3$  remained outside the detectability band at the largest crack depth investigated, the trend was toward the detectability band. This violates the previously given definition of detectability, so the crack was detectable with the metric for only two identified peaks ( $\lambda_1$  and  $\lambda_4$ ).

#### 6.9.4 Detectability Summary

The complete results of the crack detectability study are presented in this section. One hundred and twenty detectability charts, like those shown in Figures 43 through 46, were required to analyze all the combinations of the 6 damage metrics, the 5 data types ( $H_{ZZ}$ , positive frequency range  $H_{PG}$ , negative frequency range  $H_{PG}$ , and positive and negative frequency range  $H_{P\hat{G}}$ ) and the 4 conditions (clean, fixed  $XYZ$  coordinate system; noisy, fixed  $XYZ$  coordinate system; and clean and noisy moving  $xyz$  coordinate system) in the

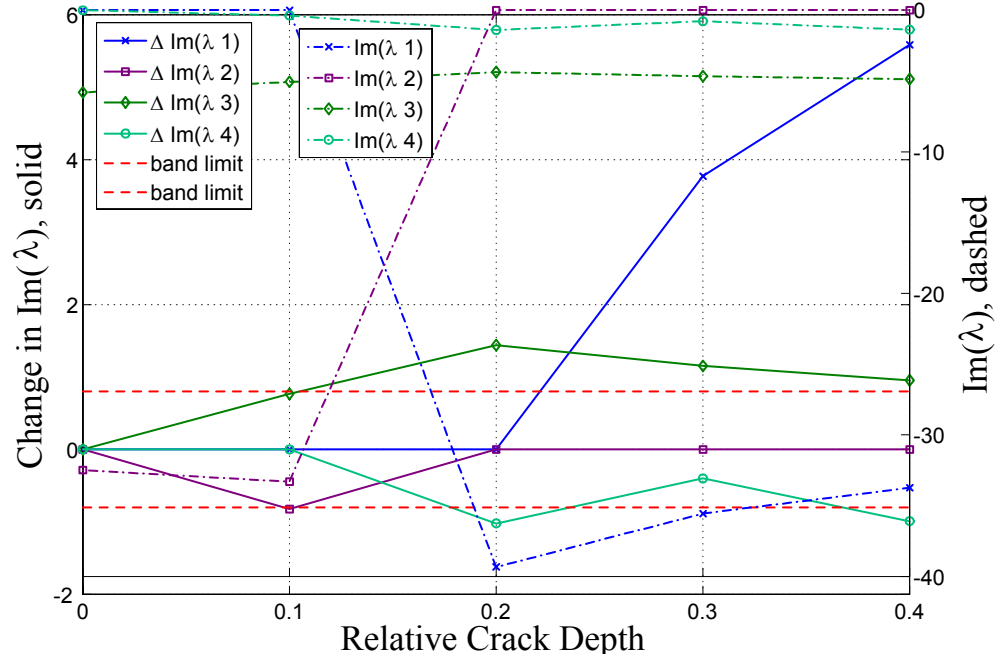


**Figure 45:** Detectability chart for  $\text{Im}(\lambda)$ . Negative frequency range dFRF  $H_{P\hat{G}}$  constructed with clean, fixed  $XYZ$  coordinate system data. Horizontal dashed lines are detectability band limits.

study. (Note that the data estimated from the normal and reverse dFRFs were broken into positive and negative frequency ranges for the analysis simply to facilitate visual detectability analysis by reducing the number of curves on the plot.) The detectability data are presented in tabular form.

The following discussion (specifically based on Table 20) describes the format used by all tables referred to in this section. (Table 20 is the subject of the discussion solely as a matter of convenience. It is the first table of its type to have non-zero elements in the top three data rows.) The top row of the table identifies which damage metrics are being discussed. A four-row group follows for each data type. The first row of the group tells what kind of data is processed, and gives the number of discrete frequency domain peaks identified by AMI. Thus, the first four-row group in Table 20 presents detectability data for the FRF  $H_{ZZ}$ . A total of 3 discrete peaks were identified by AMI during the processing of the FRFs for the given conditions (clean, moving  $xyz$  reference frame data) over the complete range of relative crack depths in the study. The second row in the four-row group,



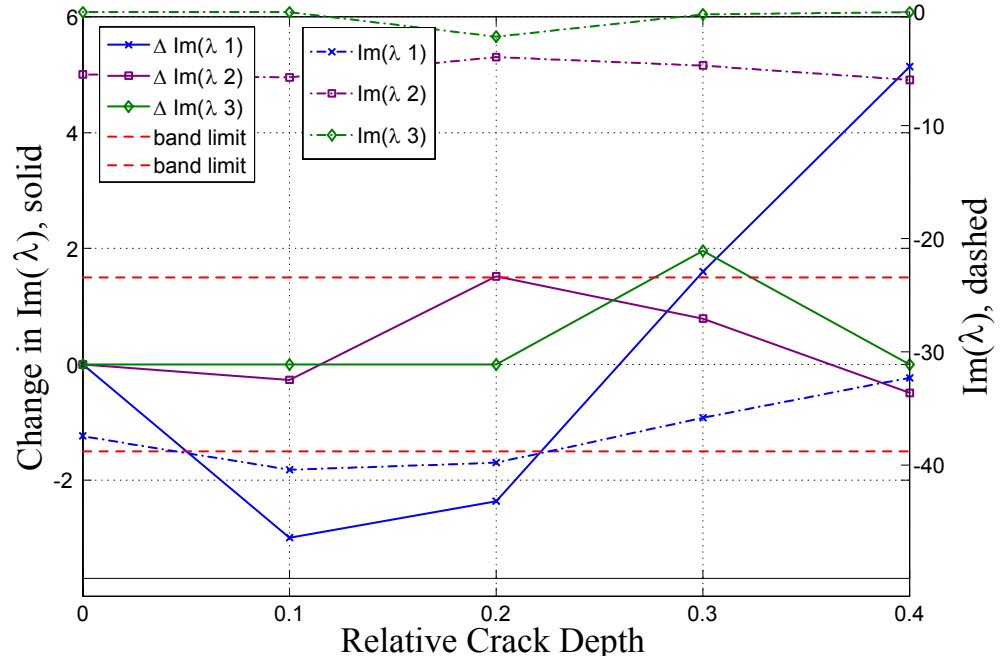


**Figure 46:** Detectability chart for  $\text{Im}(\lambda)$ . Negative frequency range dFRF  $H_{P\hat{G}}$  constructed with noisy, fixed  $XYZ$  coordinate system data. Horizontal dashed lines are detectability band limits.

“Number/% of Peaks Meeting Detectability Criterion,” presents the number of identified peaks that meet the detectability criteria discussed previously. (For example, in the case of *change in*  $\text{Im}(\lambda_k)$ , 1 of the 3 peaks identified by AMI met the detectability criteria.) The performance is also presented in percent format in the same cell ( $1/3 = 33\%$ ). The next row in the group, “Minimum Depth for Detectable Crack,” lists the minimum threshold of detectability. If there is only a single peak for which the crack is detectable, the threshold of detectability (the relative crack depth at which the plot of the damage metric first exceeds the detectability band) for that peak is given. If there are multiple peaks for which the crack is detectable, the minimum threshold of detectability for all cases is presented. (For *change in*  $\text{Im}(\lambda_k)$ , the threshold of detectability of the one peak for which the crack was detectable was 0.3 relative crack depth.) The fourth row of the group, “Average Depth for Detectable Crack,” gives the average threshold of detectability.

#### 6.9.4.1 Clean Data

The detectability data for the two eigenvalue-based metrics are shown in Table 18. These results are derived from clean, fixed  $XYZ$  coordinate system response data. The *change in*  $\text{Im}(\lambda_k)$  metric performed better than the *change in*  $\text{Re}(\lambda_k)$  metric. No crack of any depth was detectable with *change in*  $\text{Re}(\lambda_k)$  for the FRF  $H_{ZZ}$  or the dFRF  $H_{PG}$ . A crack was detectable with *change in*  $\text{Re}(\lambda_k)$  for one of the four identified peaks in the negative frequency range data for dFRF  $H_{P\hat{G}}$ , and the threshold of detectability was a relative crack depth of 0.4. The *change in*  $\text{Im}(\lambda_k)$  metric detected the presence of the crack with reverse dFRF  $H_{P\hat{G}}$  for both positive and negative frequency range data. The metric was more sensitive in the positive frequency range, where a crack of 0.1 relative depth was detected. The crack was detectable with two of four identified peaks in the negative frequency range, with an average relative crack depth for detection of 0.35.

Results for the four residue-based metrics derived from clean  $XYZ$  response data are described in Table 19. With  $H_{ZZ}$  data, both *change in*  $\text{Re}(A_k)$  and *change in*  $|A_k|$  detected the crack. Both metrics detected the crack with one of the two identified peaks, at 0.3 relative crack depth. The *change in*  $\text{Re}(A_k)$  and *change in*  $|A_k|$  metrics also detected the crack with  $H_{PG}$  data. In the positive frequency range, *change in*  $|A_k|$  detected a crack of 0.4 relative depth. In the negative frequency range, *change in*  $\text{Re}(A_k)$  and *change in*  $|A_k|$  detected cracks of 0.4 and 0.2 relative depth, respectively. With  $H_{P\hat{G}}$  data, no metric detected the crack with positive frequency range data, but all four metrics detected the crack with negative frequency range data. *Change in*  $\text{Im}(A_k)$  demonstrated the best performance by detecting the crack with two of four identified peaks at an average relative depth of 0.35.

The results for the two eigenvalue-based metrics derived from clean, moving frame  $xyz$  data are shown in Table 20. For  $H_{ZZ}$  data, a crack was detectable with one of three identified peaks at a relative depth of 0.3 using the *change in*  $\text{Im}(\lambda_k)$  metric, but the crack was not detectable using the *change in*  $\text{Re}(\lambda_k)$  metric. With  $H_{PG}$  data, the crack was not detectable with either metric. With  $H_{P\hat{G}}$  data, the crack was detectable in the positive frequency range with *change in*  $\text{Im}(\lambda_k)$  at a relative depth of 0.1. Both *change in*  $\text{Im}(\lambda_k)$

and *change in*  $\text{Re}(\lambda_k)$  detected the crack with negative frequency data with one of three identified peaks at a relative depth of 0.4.

The performance of the four residue-based metrics using clean  $xyz$  data is given in Table 21. For  $H_{ZZ}$  data, only *change in*  $\text{Im}(A_k)$  did not detect the crack. *Change in*  $|A_k|$  and *change in*  $\text{Re}(A_k)$  were the most sensitive. Both metrics detected the crack at a relative depth of 0.3. For  $H_{PG}$  data, the crack was not detectable at any depth with any metric in the positive frequency range. The metric *change in*  $|A_k|$  detected the crack at a relative depth of 0.4 with negative frequency range data. With the  $H_{P\hat{G}}$  data, the crack was detectable with all metrics except *change in*  $\text{Im}(A_k)$  in the negative frequency range. A crack of 0.1 relative depth was detectable with one of the three identified peaks using *change in*  $\arg(A_k)$ . The crack was not detectable at any depth with any metric using positive frequency range data.

#### 6.9.4.2 Noisy Data

The results for the two eigenvalue-based metrics derived from noisy, fixed  $XYZ$  response data are shown in Table 22. Both *change in*  $\text{Re}(\lambda_k)$  and *change in*  $\text{Im}(\lambda_k)$  demonstrated identically poor performance with  $H_{ZZ}$  and  $H_{PG}$  data. The crack was not detectable at any depth with either metric. With  $H_{P\hat{G}}$  data, neither metric was able to detect the presence of the crack in the positive frequency range. However, both metrics detected the crack with one of three identified peaks in the negative frequency range. The *change in*  $\text{Im}(\lambda_k)$  metric demonstrated better sensitivity by detecting the crack at 0.3 relative depth, compared to 0.4 relative depth for *change in*  $\text{Re}(\lambda_k)$ .

The performance of the four residue-based damage metrics with noisy, fixed coordinate system data is shown in Table 23. The metrics *change in*  $\text{Re}(A_k)$  and *change in*  $|A_k|$  both detected a crack of 0.3 relative depth using  $H_{ZZ}$  data. With  $H_{PG}$  data, the crack was not detectable using negative frequency range data. The *change in*  $|A_k|$  metric detected the crack at 0.4 relative depth using positive frequency  $H_{PG}$  data. No metrics detected the crack using positive frequency range  $H_{P\hat{G}}$  data, and only *change in*  $|A_k|$  detected the crack with negative frequency range  $H_{P\hat{G}}$  data.

The performance of the two eigenvalue-based metrics, derived from noisy, moving  $xyz$  coordinate system response data, is shown in Table 24. For  $H_{ZZ}$  data, only *change in*  $\text{Re}(\lambda_k)$  gave a positive result. A crack of 0.4 relative depth was detectable with one of the three identified peaks. With  $H_{PG}$  data, neither metric was able to detect a crack. For  $H_{PG}$  data, *change in*  $\text{Re}(\lambda_k)$  did not detect the crack at any depth in either frequency range. *Change in*  $\text{Im}(\lambda_k)$  detected a crack of 0.4 relative depth in the negative frequency range.

The final set of results, describing the performance of the residue-based metrics constructed from noisy  $xyz$  system response data, is presented in Table 25. For  $H_{ZZ}$  data, the metrics *change in*  $\text{Re}(A_k)$  and *change in*  $|A_k|$  detected cracks of 0.3 and 0.4 relative depth, respectively. No metric detected the crack with negative frequency range  $H_{PG}$  data, however, in the positive frequency range, *change in*  $|A_k|$  detected a 0.4 relative depth crack. In the  $H_{PG}$  data, the only metric to detect any crack was *change in*  $\arg(A_k)$ . With the negative frequency range data, this metric detected a crack of 0.4 relative depth, with one of three identified peaks. There was no crack detection using positive frequency range data.

## 6.10 Discussion

Performing experimental modal analysis (EMA) on non-modal data, for the purpose of shaft crack detection, was explored through the use of the standard model of the prototypical system. Since the cracked configuration of the prototypical system is time-varying with respect to both the fixed and moving coordinate systems, only non-modal response data were available. The time domain response of the prototypical system was calculated and converted to the frequency domain. This frequency domain response, in the forms of both standard frequency response functions (FRFs) and directional frequency response functions (dFRFs), was used to investigate the performance of six damage metrics. Experimental modal analysis of the response data using the Algorithm of Mode Isolation (AMI) for FRF data and Two-Sided AMI for dFRF data yielded estimates of “eigenvalues” and associated “residues.” The non-modal data was processed by AMI and Two-Sided AMI in the same

manner as modal data. The algorithms' outputs were still referred to as eigenvalues and residues, even though the time-varying system that produced the response data had no eigenvalues. Two metrics described the behavior of the eigenvalues: change in the real part of the eigenvalue ( $\text{Re } \lambda_k$ ) and change in the imaginary part of the eigenvalue ( $\text{Im}(\lambda_k)$ ). Four metrics were based on residues: change in the real part of the residue ( $\text{Re}(A_k)$ ), change in the imaginary part of the residue ( $\text{Im}(A_k)$ ), change in the phase of the residue ( $\arg(A_k)$ ), and change in the magnitude of the residue ( $|A_k|$ ). A system defect was said to be detectable with a metric if the change in the metric due to the presence of the defect was greater than the level of estimation accuracy AMI demonstrated with the type of response data in question in an analysis of the standard model in the nominal condition. A single transverse shaft crack, located at mid-span, was the defect examined, and the analysis was conducted with the system in five different configurations: nominal (uncracked) and relative crack depths of 0.1, 0.2, 0.3, and 0.4. For each system configuration, the  $H_{ZZ}$  FRF and the  $H_{PG}$  and  $H_{P\hat{G}}$  dFRFs were processed by AMI and Two-Sided AMI, respectively. All excitation and measurement was conducted at the bearing closer to the disk. The complete analysis was performed with clean time domain response data, and then repeated with time domain response data contaminated with white noise.

For the purposes of the following discussion, “consistency” is related to the number of data types a particular metric was able to detect a crack with. For instance, if a crack was detectable with *change in*  $\text{Im}(\lambda_k)$  for  $H_{ZZ}$  and  $H_{P\hat{G}}$  data, and the same crack was detectable with *change in*  $\arg(A_k)$  for  $H_{ZZ}$  data only, then the *change in*  $\text{Im}(\lambda_k)$  metric would have demonstrated greater consistency. The term “sensitivity” is related to the threshold of detection. If one metric detected the crack at a relative depth of 0.3 and another metric detected the crack at a relative depth of 0.1, then the second metric would have demonstrated greater sensitivity.

The three metrics delivering the best performance with clean, fixed  $XYZ$  coordinate system data were *change in*  $\text{Im}(\lambda_k)$ , *change in*  $\text{Re}(A_k)$ , and *change in*  $|A_k|$ . As discussed previously, with the normal and reverse dFRFs each broken into positive and negative frequency ranges for the detectability analysis, there are five data types:  $H_{ZZ}$ , positive

and negative frequency range  $H_{PG}$ , and positive and negative frequency range versions of  $H_{PG}$ . Regarding consistency, the crack was detectable with four of the five data types using *change in*  $|A_k|$ , three data types using *change in*  $\text{Re}(A_k)$ , and two data types using *change in*  $\text{Im}(\lambda_k)$ . Addressing sensitivity, *change in*  $\text{Im}(\lambda_k)$  detected a 0.1 relative depth crack with positive frequency range  $H_{PG}$  data, *change in*  $|A_k|$  detected a 0.2 relative depth crack with negative frequency range  $H_{PG}$  data, and *change in*  $\text{Re}(A_k)$  detected a 0.3 relative depth crack with  $H_{ZZ}$  data.

The inclusion of noise in the fixed  $XYZ$  time responses negatively impacted the performance of almost all metrics. The noise made crack detection impossible with *change in*  $\text{Im}(A_k)$  and *change in*  $\arg(A_k)$ , and the noise decreased the sensitivity of the *change in*  $|A_k|$  metric (0.2 relative depth crack detected with clean data and 0.3 relative depth crack detected with noisy data). The noise decreased to one (negative frequency range  $H_{PG}$ ) the type of data for which the crack was detectable with *change in*  $\text{Im}(\lambda_k)$ . The *change in*  $\text{Re}(\lambda_k)$  metric, which was not one of the best metrics with clean data, was the metric least impacted by the presence of noise. Neither the consistency nor the sensitivity of the metric was affected. *Change in*  $\text{Re}(\lambda_k)$  was able to detect a crack of 0.4 relative depth using both clean and noisy negative frequency range  $H_{PG}$  data. The sensitivity (but not the consistency) of *change in*  $\text{Re}(A_k)$  was also unaffected by the noise. For crack detection work in the fixed  $XYZ$  coordinate system, the damage metrics *change in*  $\text{Im}(\lambda_k)$ , *change in*  $\text{Re}(A_k)$ , and *change in*  $|A_k|$  exhibited low sensitivity to the effects of noise in the vibration signal and detected cracks of 0.3 relative depth with noisy data. Negative frequency range  $H_{PG}$  data proved to be the most robust data type with respect to noise for eigenvalue-based metrics. For residue-based metrics,  $H_{ZZ}$  and positive frequency range  $H_{PG}$  data were the most robust types with respect to noise.

The metrics *change in*  $\text{Im}(\lambda_k)$ , *change in*  $|A_k|$ , and *change in*  $\text{Re}(A_k)$  gave the best performance with both clean and noisy moving  $xyz$  coordinate system data. With clean data, the crack was detectable with *change in*  $\text{Im}(\lambda_k)$ , *change in*  $|A_k|$ , and *change in*  $\text{Re}(A_k)$  with three of five data types, three data types, and two data types, respectively. Clean data sensitivity showed that *change in*  $\text{Im}(\lambda_k)$  detected a crack of 0.1 relative depth, while both

residue-based metrics detected a crack of 0.3 relative depth. For *change in*  $\text{Im}(\lambda_k)$ , noise decreased to one the number of data types that the crack was detectable with, and increased the minimum detectable crack to 0.4 relative depth. Noise decreased the consistency of both residue-based metrics, but only negatively impacted the sensitivity of *change in*  $|A_k|$  (0.3 relative depth crack detected with clean data and 0.4 relative depth crack detected with noisy data). With clean and noisy data, the metric *change in*  $\text{Im}(A_k)$  gave the worst performance, detecting no crack with any type of data. The *change in*  $\text{Re}(\lambda_k)$  metric was, as with fixed  $XYZ$  coordinate system results, the least impacted by noise, in terms of consistency and sensitivity. The metric detected a crack of 0.4 relative depth with both clean and noisy data. The damage metrics *change in*  $\text{Im}(\lambda_k)$ , *change in*  $\text{Re}(\lambda_k)$ , *change in*  $|A_k|$ , and *change in*  $\text{Re}(A_k)$  are the best choices for future crack detection work in the moving coordinate system. They were relatively robust in the presence of noise and were capable of detecting the crack.

The results for both fixed coordinate system data and moving coordinate system data showed that the presence of noise in the time domain response had, as expected, a negative effect on most metrics. The noise typically reduced the number of peaks identified by AMI. In some instances, the noise had a negligible effect on the size of the detectable crack (*change in*  $\text{Im}(\lambda_k)$  for  $XYZ$  negative frequency range  $H_{PG}$  data), while in other instances the introduction of noise completely negated the metric (*change in*  $|A_k|$  for  $XYZ$  negative frequency range  $H_{PG}$  data). A reasonable level of measurement noise did not prevent the detection of a shaft crack through tracking a number of metrics.

Comparing the performance of the metrics *change in*  $\text{Im}(\lambda_k)$ , *change in*  $|A_k|$ , and *change in*  $\text{Re}(A_k)$  with noisy, fixed coordinate system data and noisy, moving coordinate system data shows that there is a benefit to choosing fixed coordinates over moving coordinates. The crack was detectable with all three metrics in both coordinate systems. The sensitivity of the metrics was greater in the fixed coordinate system (crack detected at average relative depth of 0.3) than in the moving coordinate system (crack detected at an average relative depth of 0.36). The results show that the reverse dFRF was by far the best data type for crack detection work with eigenvalue-based metrics, regardless of noise and choice of

coordinate system. The residue-based metrics had some degree of success with all three data types.

Although processing frequency response data of a time-varying system is not the intended use of any version of AMI, the results presented in this chapter show that the concept has potential for crack detection. The metrics *change in  $\text{Im}(\lambda_k)$* , *change in  $\text{Re}(\lambda_k)$* , *change in  $|A_k|$* , and *change in  $\text{Re}(A_k)$*  demonstrated good clean-signal sensitivity and sufficient resistance to the detrimental effects of noise.

Furthermore, the concept demonstrated a promising level of reliability. For instance, with noisy, fixed coordinate data, the crack was detectable with four of the six metrics. These four metrics included both eigenvalue-based metrics and residue-based metrics. One of these metrics, *change in  $|A_k|$* , detected the crack with  $H_{ZZ}$ ,  $H_{PG}$ , and  $H_{P\hat{G}}$  data. The results showed that crack detection through AMI processing of non-modal data is not solely dependent on one metric, one data type, or one modal property for success.

For installed equipment, it is most likely that fixed coordinate system response will be measured using existing probes. The easiest input to deliver to the system to induce the response is a fixed coordinate, unidirectional excitation. The result of this combination would be a standard, fixed coordinate system, FRF. The results suggest that the least complex diagnostic scheme with the best chance of detecting a shaft crack would track  $\text{Re}(\lambda_k)$  and  $\text{Im}(\lambda_k)$  from the FRFs and reverse dFRFs and  $\text{Re}(A_k)$  and  $|A_k|$  from all three data types. Since the dFRF data can be calculated from FRF data, no additional hardware (such as an exciter capable of delivering a complex impulse) would be required. Analyzing moving coordinate data would not require additional equipment either, since the moving coordinate system data can be calculated directly from the fixed coordinate system data.



**Table 18:** Crack detection performance of eigenvalue-based damage metrics for clean fixed reference frame FRF and dFRF data.

Damage Metric	Chng Re( $\lambda_k$ )	Chng Im( $\lambda_k$ )
<b>FRF Processing</b> (2 peaks identified)		
Number/% of Peaks Meeting Detectability Criterion	0/0%	0/0%
Minimum Depth for Detectable Crack	n/a	n/a
Average Depth for Detectable Crack	n/a	n/a
<b>Normal dFRF Processing</b>		
<i>Positive Frequency Range</i> (3 peaks identified)		
Number/% of Peaks Meeting Detectability Criterion	0/0%	0/0%
Minimum Depth for Detectable Crack	n/a	n/a
Average Depth for Detectable Crack	n/a	n/a
<i>Negative Frequency Range</i> (2 peaks identified)		
Number/% of Peaks Meeting Detectability Criterion	0/0%	0/0%
Minimum Depth for Detectable Crack	n/a	n/a
Average Depth for Detectable Crack	n/a	n/a
<b>Reverse dFRF Processing</b>		
<i>Positive Frequency Range</i> (2 peaks identified)		
Number/% of Peaks Meeting Detectability Criterion	0/0%	1/50%
Minimum Depth for Detectable Crack	n/a	0.1
Average Depth for Detectable Crack	n/a	0.1
<i>Negative Frequency Range</i> (4 peaks identified)		
Number/% of Peaks Meeting Detectability Criterion	1/25%	2/50%
Minimum Depth for Detectable Crack	0.4	0.3
Average Depth for Detectable Crack	0.4	0.35

**Table 19:** Crack detection performance of residue-based damage metrics for clean fixed reference frame FRF and dFRF data.

Damage Metric	Chng Re( $A_k$ )	Chng Im( $A_k$ )	Chng $ A_k $	Chng arg( $A_k$ )
<b>FRF Processing</b> (2 peaks identified)				
Number/% of Peaks Meeting Detectability Criterion	1/50%	0/0%	1/50%	0/0%
Minimum Depth for Detectable Crack	0.3	n/a	0.3	n/a
Average Depth for Detectable Crack	0.3	n/a	0.3	n/a
<b>Normal dFRF Processing</b>				
<i>Positive Frequency Range</i> (3 peaks identified)				
Number/% of Peaks Meeting Detectability Criterion	0/0%	0/0%	1/33%	0/0%
Minimum Depth for Detectable Crack	n/a	n/a	0.4	n/a
Average Depth for Detectable Crack	n/a	n/a	0.4	n/a
<i>Negative Frequency Range</i> (2 peaks identified)				
Number/% of Peaks Meeting Detectability Criterion	1/50%	0/0%	1/50%	0/0%
Minimum Depth for Detectable Crack	0.4	n/a	0.2	n/a
Average Depth for Detectable Crack	0.4	n/a	0.2	n/a
<b>Reverse dFRF Processing</b>				
<i>Positive Frequency Range</i> (2 peaks identified)				
Number/% of Peaks Meeting Detectability Criterion	0/0%	0/0%	0/0%	0/0%
Minimum Depth for Detectable Crack	n/a	n/a	n/a	n/a
Average Depth for Detectable Crack	n/a	n/a	n/a	n/a
<i>Negative Frequency Range</i> (4 peaks identified)				
Number/% of Peaks Meeting Detectability Criterion	1/25%	2/50%	1/25%	1/25%
Minimum Depth for Detectable Crack	0.4	0.3	0.4	0.4
Average Depth for Detectable Crack	0.4	0.35	0.4	0.4

**Table 20:** Crack detection performance of eigenvalue-based damage metrics for clean moving reference frame FRF and dFRF data.

Damage Metric	Chng Re( $\lambda_k$ )	Chng Im( $\lambda_k$ )
<b>FRF Processing</b> (3 peaks identified)		
Number/% of Peaks Meeting Detectability Criterion	0/0%	1/33%
Minimum Depth for Detectable Crack	n/a	0.3
Average Depth for Detectable Crack	n/a	0.3
<b>Normal dFRF Processing</b>		
<i>Positive Frequency Range</i> (2 peaks identified)		
Number/% of Peaks Meeting Detectability Criterion	0/0%	0/0%
Minimum Depth for Detectable Crack	n/a	n/a
Average Depth for Detectable Crack	n/a	n/a
<i>Negative Frequency Range</i> (3 peaks identified)		
Number/% of Peaks Meeting Detectability Criterion	0/0%	0/0%
Minimum Depth for Detectable Crack	n/a	n/a
Average Depth for Detectable Crack	n/a	n/a
<b>Reverse dFRF Processing</b>		
<i>Positive Frequency Range</i> (3 peaks identified)		
Number/% of Peaks Meeting Detectability Criterion	0/0%	1/33%
Minimum Depth for Detectable Crack	n/a	0.1
Average Depth for Detectable Crack	n/a	0.1
<i>Negative Frequency Range</i> (3 peaks identified)		
Number/% of Peaks Meeting Detectability Criterion	1/33%	1/33%
Minimum Depth for Detectable Crack	0.4	0.4
Average Depth for Detectable Crack	0.4	0.4

**Table 21:** Crack detection performance of residue-based damage metrics for clean moving reference frame FRF and dFRF data.

Damage Metric	Chng Re( $A_k$ )	Chng Im( $A_k$ )	Chng $ A_k $	Chng arg( $A_k$ )
<b>FRF Processing</b> (3 peaks identified)				
Number/% of Peaks Meeting Detectability Criterion	3/100%	0/0%	1/33%	2/66%
Minimum Depth for Detectable Crack	0.3	n/a	0.3	0.4
Average Depth for Detectable Crack	0.33	n/a	0.3	0.4
<b>Normal dFRF Processing</b>				
<i>Positive Frequency Range</i> (2 peaks identified)				
Number/% of Peaks Meeting Detectability Criterion	0/0%	0/0%	0/0%	0/0%
Minimum Depth for Detectable Crack	n/a	n/a	n/a	n/a
Average Depth for Detectable Crack	n/a	n/a	n/a	n/a
<i>Negative Frequency Range</i> (3 peaks identified)				
Number/% of Peaks Meeting Detectability Criterion	0/0%	0/0%	1/33%	0/0%
Minimum Depth for Detectable Crack	n/a	n/a	0.4	n/a
Average Depth for Detectable Crack	n/a	n/a	0.4	n/a
<b>Reverse dFRF Processing</b>				
<i>Positive Frequency Range</i> (3 peaks identified)				
Number/% of Peaks Meeting Detectability Criterion	0/0%	0/0%	0/0%	0/0%
Minimum Depth for Detectable Crack	n/a	n/a	n/a	n/a
Average Depth for Detectable Crack	n/a	n/a	n/a	n/a
<i>Negative Frequency Range</i> (3 peaks identified)				
Number/% of Peaks Meeting Detectability Criterion	1/33%	0/0%	1/33%	1/33%
Minimum Depth for Detectable Crack	0.4	n/a	0.4	0.1
Average Depth for Detectable Crack	0.4	n/a	0.4	0.1

**Table 22:** Crack detection performance of eigenvalue-based damage metrics for noisy fixed reference frame FRF and dFRF data.

Damage Metric	Chng Re( $\lambda_k$ )	Chng Im( $\lambda_k$ )
<b>FRF Processing</b> (2 peaks identified)		
Number/% of Peaks Meeting Detectability Criterion	0/0%	0/0%
Minimum Depth for Detectable Crack	n/a	n/a
Average Depth for Detectable Crack	n/a	n/a
<b>Normal dFRF Processing</b>		
<i>Positive Frequency Range</i> (2 peaks identified)		
Number/% of Peaks Meeting Detectability Criterion	0/0%	0/0%
Minimum Depth for Detectable Crack	n/a	n/a
Average Depth for Detectable Crack	n/a	n/a
<i>Negative Frequency Range</i> (3 peaks identified)		
Number/% of Peaks Meeting Detectability Criterion	0/0%	0/0%
Minimum Depth for Detectable Crack	n/a	n/a
Average Depth for Detectable Crack	n/a	n/a
<b>Reverse dFRF Processing</b>		
<i>Positive Frequency Range</i> (2 peaks identified)		
Number/% of Peaks Meeting Detectability Criterion	0/0%	0/0%
Minimum Depth for Detectable Crack	n/a	n/a
Average Depth for Detectable Crack	n/a	n/a
<i>Negative Frequency Range</i> (3 peaks identified)		
Number/% of Peaks Meeting Detectability Criterion	1/33%	1/33%
Minimum Depth for Detectable Crack	0.4	0.3
Average Depth for Detectable Crack	0.4	0.3

**Table 23:** Crack detection performance of residue-based damage metrics for noisy fixed reference frame FRF and dFRF data.

Damage Metric	Chng Re( $A_k$ )	Chng Im( $A_k$ )	Chng $ A_k $	Chng arg( $A_k$ )
<b>FRF Processing</b> (2 peaks identified)				
Number/% of Peaks Meeting Detectability Criterion	1/50%	0/0%	1/50%	0/0%
Minimum Depth for Detectable Crack	0.3	n/a	0.3	n/a
Average Depth for Detectable Crack	0.3	n/a	0.3	n/a
<b>Normal dFRF Processing</b>				
<i>Positive Frequency Range</i> (2 peaks identified)				
Number/% of Peaks Meeting Detectability Criterion	0/0%	0/0%	1/33%	0/0%
Minimum Depth for Detectable Crack	n/a	n/a	0.4	n/a
Average Depth for Detectable Crack	n/a	n/a	0.4	n/a
<i>Negative Frequency Range</i> (3 peaks identified)				
Number/% of Peaks Meeting Detectability Criterion	0/0%	0/0%	0/0%	0/0%
Minimum Depth for Detectable Crack	n/a	n/a	n/a	n/a
Average Depth for Detectable Crack	n/a	n/a	n/a	n/a
<b>Reverse dFRF Processing</b>				
<i>Positive Frequency Range</i> (2 peaks identified)				
Number/% of Peaks Meeting Detectability Criterion	0/0%	0/0%	0/0%	0/0%
Minimum Depth for Detectable Crack	n/a	n/a	n/a	n/a
Average Depth for Detectable Crack	n/a	n/a	n/a	n/a
<i>Negative Frequency Range</i> (3 peaks identified)				
Number/% of Peaks Meeting Detectability Criterion	0/0%	0/0%	1/33%	0/0%
Minimum Depth for Detectable Crack	n/a	n/a	0.4	n/a
Average Depth for Detectable Crack	n/a	n/a	0.4	n/a

**Table 24:** Crack detection performance of eigenvalue-based damage metrics for noisy moving reference frame FRF and dFRF data.

Damage Metric	Chng Re( $\lambda_k$ )	Chng Im( $\lambda_k$ )
<b>FRF Processing</b> (3 peaks identified)		
Number/% of Peaks Meeting Detectability Criterion	1/33%	0/0%
Minimum Depth for Detectable Crack	0.4	n/a
Average Depth for Detectable Crack	0.4	n/a
<b>Normal dFRF Processing</b>		
<i>Positive Frequency Range</i> (2 peaks identified)		
Number/% of Peaks Meeting Detectability Criterion	0/0%	0/0%
Minimum Depth for Detectable Crack	n/a	n/a
Average Depth for Detectable Crack	n/a	n/a
<i>Negative Frequency Range</i> (3 peaks identified)		
Number/% of Peaks Meeting Detectability Criterion	0/0%	0/0%
Minimum Depth for Detectable Crack	n/a	n/a
Average Depth for Detectable Crack	n/a	n/a
<b>Reverse dFRF Processing</b>		
<i>Positive Frequency Range</i> (3 peaks identified)		
Number/% of Peaks Meeting Detectability Criterion	0/0%	0/0%
Minimum Depth for Detectable Crack	n/a	n/a
Average Depth for Detectable Crack	n/a	n/a
<i>Negative Frequency Range</i> (3 peaks identified)		
Number/% of Peaks Meeting Detectability Criterion	0/0%	1/33%
Minimum Depth for Detectable Crack	n/a	0.4
Average Depth for Detectable Crack	n/a	0.4

**Table 25:** Crack detection performance of residue-based damage metrics for noisy moving reference frame FRF and dFRF data.

Damage Metric	Chng Re( $A_k$ )	Chng Im( $A_k$ )	Chng $ A_k $	Chng arg( $A_k$ )
<b>FRF Processing</b> (3 peaks identified)				
Number/% of Peaks Meeting Detectability Criterion	1/33%	0/0%	1/33%	0/0%
Minimum Depth for Detectable Crack	0.3	n/a	0.4	n/a
Average Depth for Detectable Crack	0.3	n/a	0.4	n/a
<b>Normal dFRF Processing</b>				
<i>Positive Frequency Range</i> (2 peaks identified)				
Number/% of Peaks Meeting Detectability Criterion	0/0%	0/0%	1/50%	0/0%
Minimum Depth for Detectable Crack	n/a	n/a	0.4	n/a
Average Depth for Detectable Crack	n/a	n/a	0.4	n/a
<i>Negative Frequency Range</i> (3 peaks identified)				
Number/% of Peaks Meeting Detectability Criterion	0/0%	0/0%	0/0%	0/0%
Minimum Depth for Detectable Crack	n/a	n/a	n/a	n/a
Average Depth for Detectable Crack	n/a	n/a	n/a	n/a
<b>Reverse dFRF Processing</b>				
<i>Positive Frequency Range</i> (3 peaks identified)				
Number/% of Peaks Meeting Detectability Criterion	0/0%	0/0%	0/0%	0/0%
Minimum Depth for Detectable Crack	n/a	n/a	n/a	n/a
Average Depth for Detectable Crack	n/a	n/a	n/a	n/a
<i>Negative Frequency Range</i> (3 peaks identified)				
Number/% of Peaks Meeting Detectability Criterion	0/0%	0/0%	0/0%	1/33%
Minimum Depth for Detectable Crack	n/a	n/a	n/a	0.4
Average Depth for Detectable Crack	n/a	n/a	n/a	0.4



## CHAPTER VII

# DEFECT DETECTION WITH MULTIPLE DEFECTS PRESENT

### ***7.1 Introduction***

This chapter extends the study of the use of EMA concepts for defect detection when the processed response data are non-modal, by considering the presence of multiple system defects. Because one of the defects investigated is the shaft crack, the response data are non-modal, regardless of the coordinate system chosen. A detailed discussion of how the presence of a shaft crack creates a time-varying system, and thereby non-modal response data, was presented in Chapter VI.

### ***7.2 Method Overview***

A single shaft crack at midspan and wear of Bearing 1 are simultaneously simulated with the standard model of the prototypical system. Both defects are introduced at levels previously proven to be detectable with at least one metric. One defect is held constant while the magnitude of the other defect is increased. FRF and dFRF response data sets, calculated from time domain response data, for a range of increasing defect magnitudes are processed by AMI. A determination of detectability is made through a comparison of the AMI-estimated properties for the nominal and damaged cases. The analysis is repeated with the opposite combination of constant and increasing defects. Although it is unlikely that two detectable defects will exist in a machine at one time, it is worthwhile to investigate their possible interaction when one defect is small enough that equipment failure is not imminent. The chance that two detectable defects will be present at the same time, and increasing at approximately the same rate, is so remote that the scenario is not addressed.

This multiple defect study is a preliminary analysis which is limited in resolution and focused on certain damage metrics that have been shown to give good results in previous

chapters. The full ranges of shaft crack depth and increased bearing clearance used in previous studies are investigated here, but not every intermediate value of crack depth or bearing clearance is simulated. In the shaft crack study presented in Chapter VI, it was shown that fixed coordinate system  $XYZ$  data delivered better performance than moving coordinate system data and that the metric *change in  $\text{Im}(\lambda_k)$*  detected the smallest crack. In the bearing wear study presented in Chapter V, *percent change in  $\text{Im}(\lambda_k)$*  demonstrated the greatest sensitivity of any metric. (Refer to the definitions of “sensitivity” and “consistency” in the Discussion section of Chapter VI.) The metric *percent change in  $|A_k|$*  was the next most sensitive metric in the bearing wear study, and it also delivered greater consistency than the *percent change in  $\text{Im}(\lambda_k)$*  metric. (The related *change in  $|A_k|$*  metric also performed well in the shaft crack study.) Therefore, in the multiple-defect study, only the two promising damage metrics *change in  $\text{Im}(\lambda_k)$*  and *change in  $|A_k|$*  are evaluated. Moving coordinate system data is not considered. In an effort to concentrate on generating the most useful results, only noisy data, constructed in the same manner as in the shaft crack study, is processed.

The time domain solution procedure used for the standard model of the prototypical system in Chapter VI is used in this study also. The valid frequency range of the standard model remains 0 to 60 nondimensional frequency units. The same type of graphical detectability analysis used in the shaft crack study for non-modal data is employed here (see Figure 16). The noisy data, fixed coordinate system detectability band values for  $\text{Im}(\lambda_k)$  and  $|A_k|$ , presented in the shaft crack study (see Table 16), are also valid for this study.

The conventions associated with performing EMA on non-modal data, which were defined in the shaft crack study, are used here as well. The results of AMI and Two-Sided AMI processing of non-modal data are referred to as “eigenvalues” and “residues” to avoid the introduction of unnecessary complexity in the discussion. Prominent sections of a frequency response plot to which data is fit are called “identified peaks,” not “modes.”

### 7.3 Analysis Method

The system is operated at a constant rotation rate of 1.35 nondimensional frequency units. For each operating condition, system responses to both  $Y$ -direction and  $Z$ -direction impulses are required. The impulse excitation occurs at Bearing 1, and the equations of motion, defined in the fixed coordinate system, are solved in the time domain. The fixed coordinate system time domain responses to a given impulse are contaminated with noise and independently converted to frequency domain. The parameters for the FFT calculations are  $T = 8$  nondimensional time units and  $N = 512$  sampling intervals. The same exponential window described previously in the shaft crack study is used here. The corresponding dFRFs are calculated from the FRFs. The FRF and dFRF data sets are processed separately by AMI and Two-Sided AMI. The response of the nominal system is available from the shaft crack study. The four different operating conditions (nominal plus three levels of defect) for each analysis (increasing bearing clearance with constant crack, and increasing crack depth with constant bearing clearance) are shown in Table 26. “Relative Crack Depth” is a percentage of the diameter of the prototypical system’s shaft. Note that all increased clearance values investigated are still within the range of normal operations ( $H8$  fit class), as defined in the bearing wear study. As in the shaft crack study, each identified peak is tracked independently as the defect magnitude increases.

**Table 26:** Operating conditions for standard model of prototypical system in dual defect study.

Operating Condition	Bearing Clearance ( $\mu\text{m}$ )	Brg Clearance Increase	Relative Crack Depth
<i>Increasing Bearing Clearance Analysis</i>			
1 (nominal)	50	0	0
2	60	20%	0.3
3	70	40%	0.3
4	89	79%	0.3
<i>Increasing Relative Crack Depth Analysis</i>			
1 (nominal)	50	0%	0
2	60	20%	0.3
3	60	20%	0.35
4	60	20%	0.4

## 7.4 Results

The multiple-defect time domain response plots are similar, at the resolution of visual inspection, to the time domain responses generated in the shaft crack study. Refer to the figures presented previously, including Figure 23, to see the form of the response.

The qualitative effects of multiple defects on the system frequency response are illustrated below in two cases. In the first case, a constant-magnitude, detectable shaft crack of relative depth 0.3 was present as the clearance in Bearing 1 was increased from nominal to the maximum for the H8 fit class. Figures 47, 48, and 49 show noisy data  $H_{ZZ}$ ,  $H_{PG}$ , and  $H_{PG\hat{G}}$  in the fixed  $XYZ$  coordinate system for the prototypical system with a crack of 0.3 relative depth. In each figure, the dotted line represents response with nominal bearings, and the solid line represents response with Bearing 1 worn to a 79% clearance increase. These curves represent the minimum and maximum clearances investigated, and, therefore, serve to illustrate the range of system responses encountered in the analysis. For the standard FRF, the general shape and amplitude of the curves were similar for both operating conditions. For the normal dFRF data, increased bearing clearance resulted in increased  $|H_{PG}|$  over the entire frequency range. The same effect was evident with  $|H_{PG\hat{G}}|$ . Additionally, a prominent peak in the low frequency response of the cracked shaft system with nominal bearings broadened with the addition of bearing wear, so as to become visually insignificant in the reverse dFRF data format.

In the second case, the clearance in Bearing 1 was held constant at a worn value while a shaft crack was introduced. Refer to Figures 50, 51, and 52. In each figure, the response of the system with an intact shaft and bearing clearance increased 20% from nominal is represented by the dotted line, and the response for the system at the same bearing clearance with a 0.4 relative depth shaft crack is represented by the solid line. These curves bound the system responses encountered in the analysis because they are associated with the smallest and largest cracks evaluated. Slight amplitude differences were evident in both the  $\text{Re}(H_{ZZ})$  and  $\text{Im}(H_{ZZ})$  subplots due to the presence of a shaft crack (see Figure 50). Also, the magnitude of  $H_{ZZ}$  was greater in the cracked shaft case for all nondimensional frequency units greater than 5. The difference was most obvious above 35 nondimensional

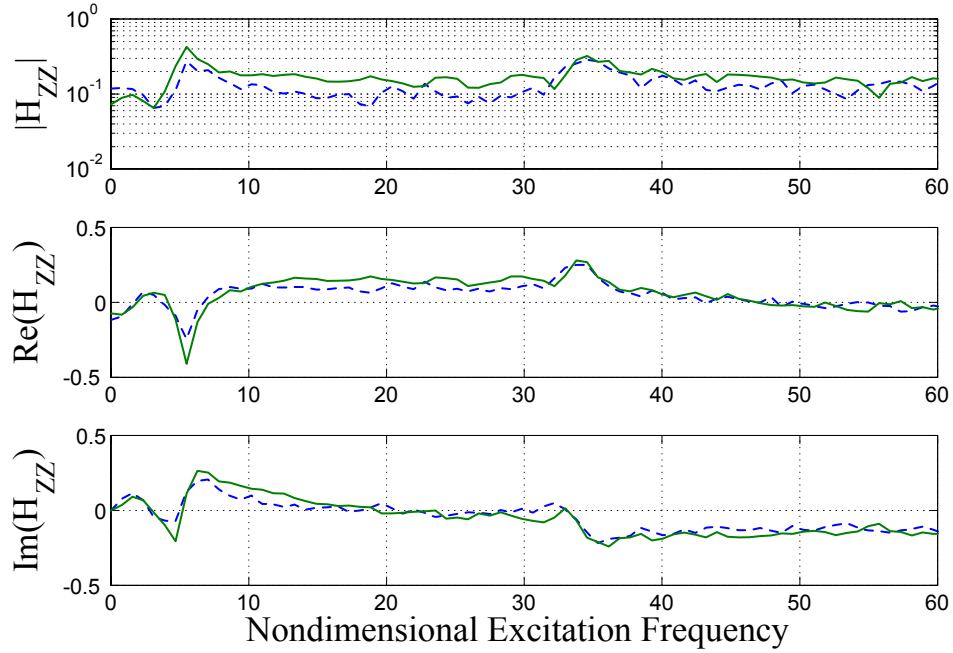


**Figure 47:** FRF  $H_{ZZ}$  at Bearing 1, due to impulse at Bearing 1, for system with crack of 0.3 relative depth. Nominal bearing clearance: dotted line. 79% increase in bearing clearance: solid line. Noisy, windowed, fixed  $XYZ$  data.

frequency units. Slight increases in both  $|H_{PG}|$  (Figure 51) and  $|H_{PG}|$  (Figure 52) over most of the frequency range, due to the inclusion of the shaft crack, were visible. Note that the inclusion of the crack had the opposite effect in the very low frequency range ( $-2$  to 2 nondimensional frequency units) of both plots.

Ten detectability charts were required to analyze all the combinations of the 2 damage metrics and the 5 data types ( $H_{ZZ}$ , positive and negative frequency range  $H_{PG}$ , and positive and negative frequency range  $H_{PG}$ ). Only noisy, fixed  $XYZ$  coordinate system data was used in the study. Note that, as in the shaft crack study, the properties estimated from the normal and reverse dFRFs were separated based on the frequency range of the processed response data (positive or negative) simply to facilitate visual detectability analysis by reducing the number of curves on the plot. The complete set of detectability data is presented in tabular form and discussed below.

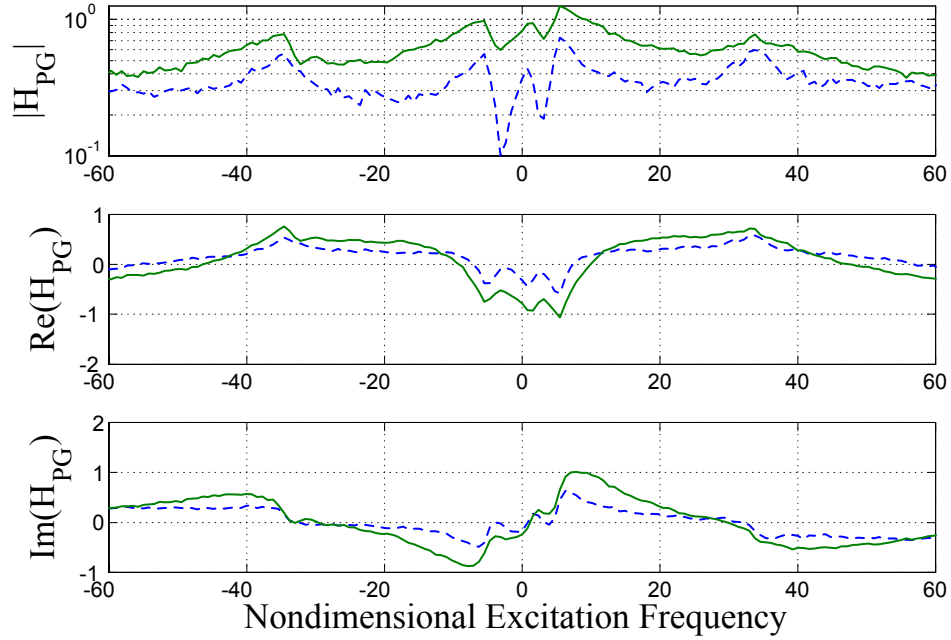


**Figure 48:** dFRF  $H_{PG}$  at Bearing 1, due to impulse at Bearing 1, for system with crack of 0.3 relative depth. Nominal bearing clearance: dotted line. 79% increase in bearing clearance: solid line. Noisy, windowed, fixed  $XYZ$  data.

#### 7.4.1 Constant Shaft Crack and Increasing Bearing Wear

The outcome of this analysis is presented in Table 27. (Refer to the explanation of the format of the results tables in Chapter VI.) With standard FRF data, bearing wear was not detectable with either *change in*  $\text{Im}(\lambda_k)$  or *change in*  $|A_k|$ . Bearing wear was detectable with both metrics for normal dFRF data. The metric *change in*  $\text{Im}(\lambda_k)$  detected the defect with both positive and negative frequency range data, but only at the most advanced wear state (79% clearance increase). *Change in*  $|A_k|$  demonstrated greater sensitivity by detecting wear at 20% clearance increase in both frequency ranges. No level of bearing wear was detectable by the *change in*  $\text{Im}(\lambda_k)$  metric with reverse dFRF data, but the *change in*  $|A_k|$  metric detected wear in both frequency ranges using reverse dFRF data. With negative frequency range data, wear was detectable at 20% clearance increase. The best combination of metric and data type was *change in*  $|A_k|$  and positive and negative frequency range normal dFRF data. Here, bearing wear was detectable with four of five

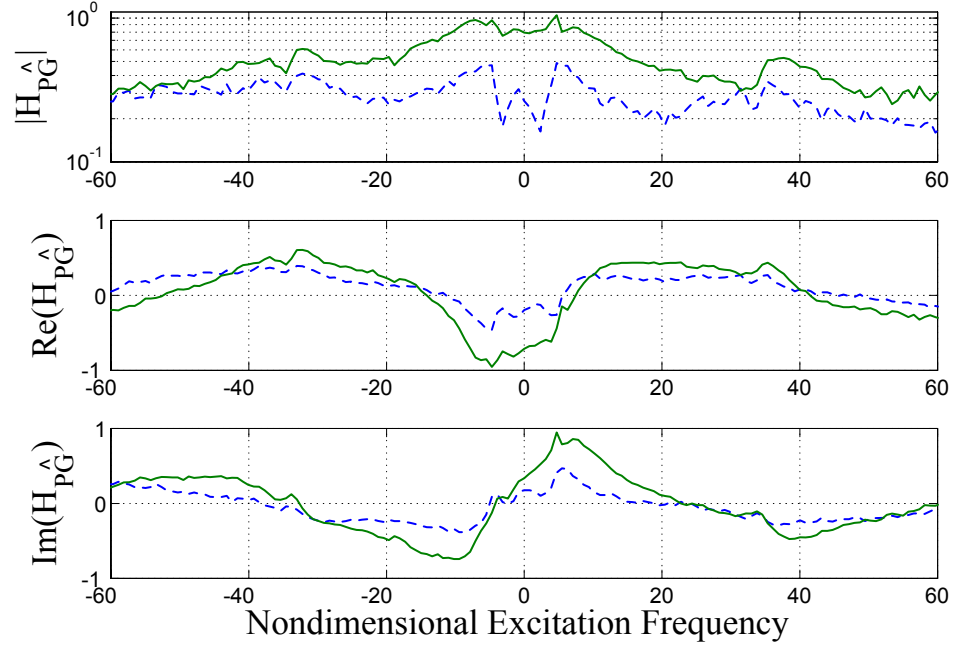


**Figure 49:** dFRF  $H_{PG}$  at Bearing 1, due to impulse at Bearing 1, for system with crack of 0.3 relative depth. Nominal bearing clearance: dotted line. 79% increase in bearing clearance: solid line. Noisy, windowed, fixed XYZ data.

identified peaks. The average level of detectable wear was a 30% increase in clearance, and the minimum amount of detectable wear was a 20% clearance increase.

#### 7.4.2 Constant Bearing Wear and Increasing Shaft Crack

The detectability data for this case is presented in Table 28. *Change in  $\text{Im}(\lambda_k)$*  was not able to detect a crack of any depth with either standard FRF data or normal dFRF data. With reverse dFRF data, *change in  $\text{Im}(\lambda_k)$*  detected the crack with one of two identified peaks in both the positive and negative frequency ranges. The minimum relative crack depth required for detection was 0.3 in both cases. *Change in  $|A_k|$*  was able to detect a 0.4 relative depth crack with FRF data and a 0.3 relative depth crack with negative frequency range normal dFRF data. Crack detection with this metric was not possible with reverse dFRF data.

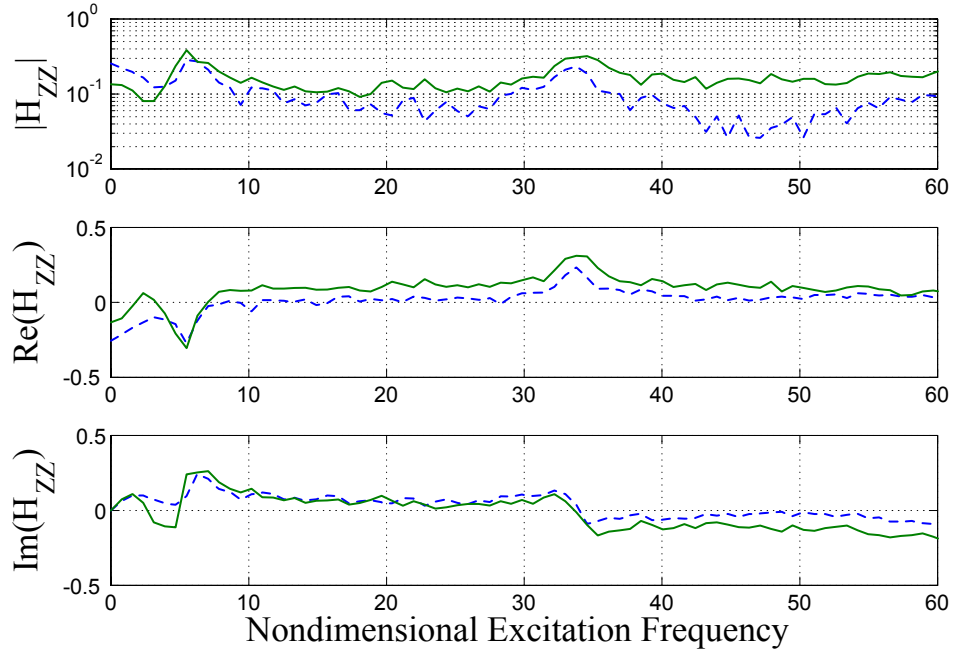


**Figure 50:** FRF  $H_{ZZ}$  at Bearing 1, due to impulse at Bearing 1, for system with 20% increase in bearing clearance. Intact shaft: dotted line. Shaft with crack of 0.4 relative depth: solid line Noisy, windowed, fixed  $XYZ$  data.

## 7.5 Discussion

The study of defect detection through the use of EMA techniques on non-modal data was continued using the standard model of the prototypical system configured with multiple defects. The time domain response of the system was calculated and converted to the frequency domain. This frequency domain response, in the forms of both standard frequency response functions (FRFs) and directional frequency response functions (dFRFs), was used to investigate the performance of the damage metrics change in the imaginary part of the eigenvalue ( $\text{Im}(\lambda_k)$ ) and change in the magnitude of the residue ( $|A_k|$ ). Both metrics had performed well in previous single-defect testing. Experimental modal analysis of the response data using the Algorithm of Mode Isolation (AMI) for FRF data and Two-Sided AMI for dFRF data yielded system parameters in terms of “eigenvalues” and associated “residues.” The non-modal data were processed by AMI and Two-Sided AMI as if it were modal data. A system defect was said to be detectable with a metric if the change in the



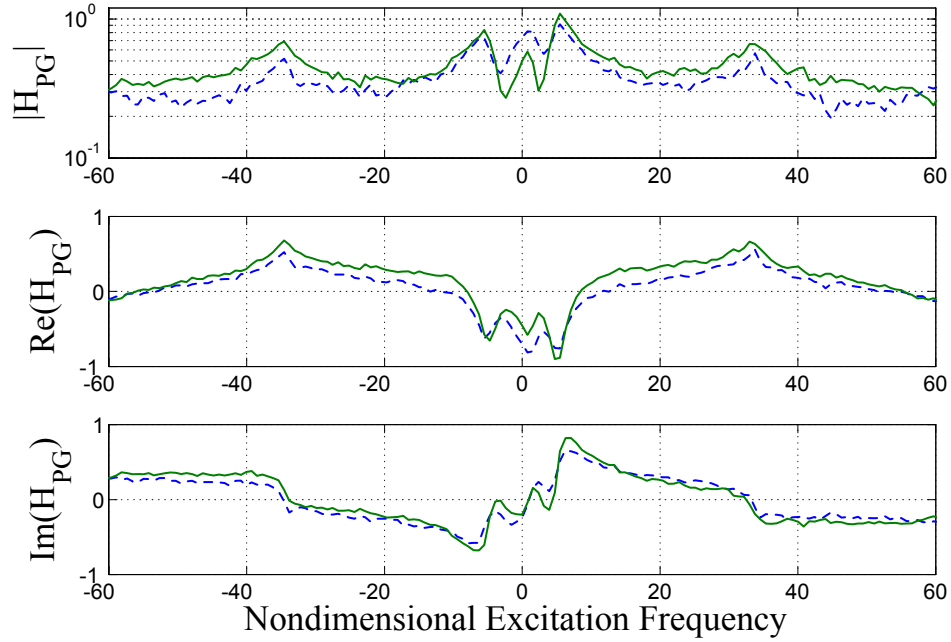


**Figure 51:** dFRF  $H_{PG}$  at Bearing 1, due to impulse at Bearing 1, for system with 20% increase in bearing clearance. Intact shaft: dotted line. Shaft with crack of 0.4 relative depth: solid line Noisy, windowed, fixed  $XYZ$  data.

metric due to the presence of the defect was greater than AMI's estimation error in the processing of response data generated by the standard model of the prototypical system in nominal condition. A single transverse shaft crack, located at mid-span, and bearing wear, simulated with increased clearance in one bearing, were the defects examined. The time-varying nature of the cracked system prevented an analytical model analysis to generate comparison properties of modal data. Two simulations were conducted. In the first, a crack of detectable magnitude was put in the system and held at a constant size while bearing clearance was increased. In the second, the opposite combination of constant- and increasing-magnitude defects was used. For each system configuration tested, the  $H_{ZZ}$  FRF and the  $H_{PG}$  and  $H_{PG}$  dFRFs were processed by AMI and Two-Sided AMI, respectively. All excitation and measurement was conducted at the bearing closer to the disk. All testing was done with fixed coordinate system data contaminated with white noise in the time domain. The specific objective of this work was to determine what effect the

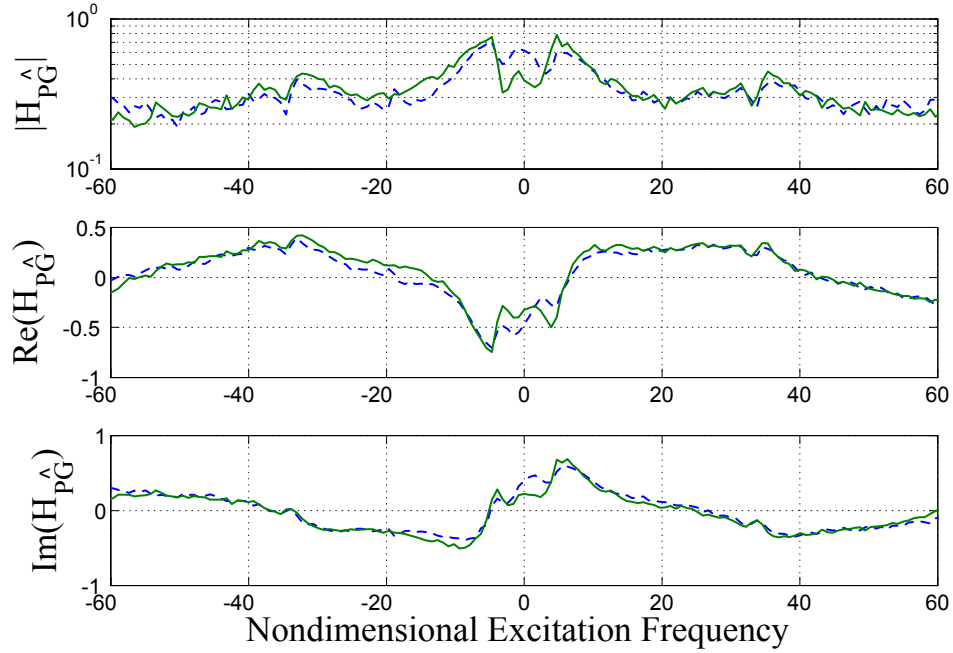


**Figure 52:** dFRF  $H_{PG}$  at Bearing 1, due to impulse at Bearing 1, for system with 20% increase in bearing clearance. Intact shaft: dotted line. Shaft with crack of 0.4 relative depth: solid line. Noisy, windowed, fixed  $XYZ$  data.

presence of a constant-magnitude, detectable defect would have on detectability of another defect of increasing magnitude. The broader objective was to more fully understand the practice of conducting EMA on non-modal data.

### 7.5.1 Constant Shaft Crack and Increasing Bearing Wear

Tables 13 and 14 show bearing wear detection performance of eigenvalue- and residue-based damage metrics for single-defect operating conditions. The multiple-defect data is in Table 27. Comparison of the performance of the eigenvalue-based metrics with single-defect data and multiple-defect data reveals the expected trends. The sensitivity of the metric based on  $\text{Im}(\lambda_k)$  is reduced, due to the presence of the crack. For example, with FRF data, bearing wear was detectable, at an average increase in bearing clearance of 35%, in the single-defect case, but no level of wear was detectable in the multiple-defect study. With dFRF data, a 20% increase in bearing clearance was detected in the single-defect study. In the multiple-defect study, no wear was detected with reverse dFRF data, and the lowest

level of bearing wear detectable with normal dFRF data was a 79% clearance increase. A similar trend was apparent in the performance of the metrics based on  $|A_k|$ . In general, the presence of an additional detectable defect reduced, but did not totally eliminate, the metrics' ability to detect bearing wear.

It is important to keep in mind that for bearing wear, the comparisons between single-defect data and multiple-defect data are not direct. The single-defect testing was done with clean data generated through the frequency domain solution of the simplified model of the prototypical system. The multiple-defect testing was done with noisy data generated from the time domain solution of the standard model of the prototypical system. Furthermore, slightly different metrics (*percent* changes versus *changes*) were used in the two studies. Even with all the differences between the single-defect testing and the multiple-defect testing considered, the results confirm a conclusion drawn in the bearing wear study of Chapter V. Residue-based metrics show potential for hydrodynamic bearing wear detection.

An important observation that can be made from a review of only the data in Table 27 is that the presence of a detectable shaft crack did not prevent the detection of bearing wear in the range of normal operating clearances by both *change in*  $\text{Im}(\lambda_k)$  and *change in*  $|A_k|$ .

### 7.5.2 Constant Bearing Wear and Increasing Shaft Crack

Tables 22 and 23 show shaft crack detection performance of eigenvalue- and residue-based damage metrics for single-defect operating conditions, and the multiple-defect study data is in Table 28. Unlike the constant crack / increasing wear analysis, the comparison between single-defect and multiple-defect data for this analysis is direct because both noisy data and the same metrics were used in each study. The sensitivity of the *change in*  $\text{Im}(\lambda_k)$  metric with reverse dFRF data was not impacted by the presence of bearing wear. The minimum relative depth for a detectable crack was 0.3 for both single- and multiple-defect data. Changes in the metric's sensitivity with standard FRF data and normal dFRF data could not be evaluated because no crack was detectable with the metric using either data type in either the single-defect study or the multiple-defect study.

The sensitivity of the *change in  $|A_k|$*  metric was lower in the multiple-defect study (crack detected at 0.4 relative depth) than in the single-defect study (crack detected at 0.3 relative depth) with standard FRF data. With normal dFRF data, the metric's sensitivity actually improved slightly in the multiple-defect study, relative to the single-defect study. The introduction of multiple defects caused the metric to be unable to detect the crack with reverse dFRF data. However, in the single-defect study, *change in  $|A_k|$*  detected a 0.4 relative depth crack with reverse dFRF data. Note that for each data type presented in Tables 23 and 28 and discussed here, the crack was detected by *change in  $|A_k|$*  with only one identified peak.

### 7.5.3 General

The performance of the metrics *change in  $\text{Im}(\lambda_k)$*  and *change in  $|A_k|$*  supports one conclusion drawn in the shaft crack study in Chapter VI. Although AMI is structured to work with modal data, it was still possible to successfully perform defect detection using non-modal response data. Furthermore, the presence of one constant-magnitude detectable defect did not prevent the detection of a second defect of increasing magnitude through AMI processing of non-modal data.

**Table 27:** Defect detection performance of damage metrics with two defects present. Crack held constant at 0.3 relative depth while bearing clearance increased. Noisy, fixed reference frame data.

<b>Damage Metric</b>	<b>Chng</b> $\text{Im}(\lambda_k)$	<b>Chng</b> $ A_k $
<b>FRF Processing</b> (2 peaks identified)		
Number/% of Peaks Meeting Detectability Criterion	0/0%	0/0%
Minimum Clearance Increase for Detectable Wear	n/a	n/a
Average Clearance Increase for Detectable Wear	n/a	n/a
<b>Normal dFRF Processing</b>		
<i>Positive Frequency Range</i> (3 peaks identified)		
Number/% of Peaks Meeting Detectability Criterion	1/33%	2/66%
Minimum Clearance Increase for Detectable Wear	79%	20%
Average Clearance Increase for Detectable Wear	79%	30%
<i>Negative Frequency Range</i> (2 peaks identified)		
Number/% of Peaks Meeting Detectability Criterion	1/50%	2/100%
Minimum Clearance Increase for Detectable Wear	79%	20%
Average Clearance Increase for Detectable Wear	79%	30%
<b>Reverse dFRF Processing</b>		
<i>Positive Frequency Range</i> (2 peaks identified)		
Number/% of Peaks Meeting Detectability Criterion	0/0%	1/50%
Minimum Clearance Increase for Detectable Wear	n/a	79%
Average Clearance Increase for Detectable Wear	n/a	79%
<i>Negative Frequency Range</i> (2 peaks identified)		
Number/% of Peaks Meeting Detectability Criterion	0/0%	1/50%
Minimum Clearance Increase for Detectable Wear	n/a	20%
Average Clearance Increase for Detectable Wear	n/a	20%

**Table 28:** Defect detection performance of damage metrics with two defects present. Bearing clearance held constant at 20 percent increase from nominal while crack depth increased. Noisy, fixed reference frame data.

Damage Metric	Chng $\text{Im}(\lambda_k)$	Chng $ A_k $
<b>FRF Processing</b> (2 peaks identified)		
Number/% of Peaks Meeting Detectability Criterion	0/0%	1/50%
Minimum Depth for Detectable Crack	n/a	0.4
Average Depth for Detectable Crack	n/a	0.4
<b>Normal dFRF Processing</b>		
<i>Positive Frequency Range</i> (3 peaks identified)		
Number/% of Peaks Meeting Detectability Criterion	0/0%	0/0%
Minimum Depth for Detectable Crack	n/a	n/a
Average Depth for Detectable Crack	n/a	n/a
<i>Negative Frequency Range</i> (2 peaks identified)		
Number/% of Peaks Meeting Detectability Criterion	0/0%	1/50%
Minimum Depth for Detectable Crack	n/a	0.3
Average Depth for Detectable Crack	n/a	0.3
<b>Reverse dFRF Processing</b>		
<i>Positive Frequency Range</i> (2 peaks identified)		
Number/% of Peaks Meeting Detectability Criterion	1/50%	0/0%
Minimum Depth for Detectable Crack	0.3	n/a
Average Depth for Detectable Crack	0.3	n/a
<i>Negative Frequency Range</i> (2 peaks identified)		
Number/% of Peaks Meeting Detectability Criterion	1/50%	0/0%
Minimum Depth for Detectable Crack	0.3	n/a
Average Depth for Detectable Crack	0.3	n/a

## CHAPTER VIII

### SUMMARY AND CONCLUSIONS

Hydrodynamic bearing wear detection technology is not very reliable. Most oil analysis methods are not instantaneous, and the vibration signature methods rely on ruling out other defects to arrive at the diagnosis of bearing wear. Many shaft crack detection methods depend on transient operation of the equipment and/or very accurate analytical models of the equipment. Both bearing wear and shaft cracks change the physical characteristics, and therefore the modal properties, of the system. With the proper method, identifying changes in the modal properties could be equivalent to identifying equipment defects. Across the business spectrum, owners typically demand that their equipment operates for long periods of time at the design point. Taking these facts into account, there is a need for a method to extract modal parameters from a noisy signal taken with existing instrumentation during normal operation of rotating equipment.

In Chapter *III*, an analytical model of a simple rotordynamic system from the literature was modified so that it could simulate the effects of a worn hydrodynamic bearing and a transverse shaft crack. The existing model was termed the “simplified” model, and the modified model was called the “standard” model. Excitation and measurement points for both models were limited to the bearing locations to accurately simulate installed equipment. The bearing wear was modeled as a uniform increase in clearance. Per published works, this type of wear simulation provides changes in stiffness and damping of the correct sign and order of magnitude. The shaft crack was modeled as an undamped, gaping crack, following a well-known method from the literature. A gaping crack model exhibits most of the effects associated with a crack, while being simpler to implement than a breathing crack model. The simplified model was solved in the frequency domain in the bearing wear study and in the testing of a new EMA routine. The standard model was solved in the time domain in studies involving shaft crack detection.

Although development and testing of the directional frequency response function (dFRF) is chronicled in the literature, the author was unable to find any published reports of the use of dFRFs in experimental modal analysis. In Chapter IV, the existing experimental modal analysis routine, Algorithm of Mode Isolation (AMI) was modified to process dFRFs, and named Two-Sided AMI. This was done to take advantage of the reported benefits of the dFRF: completely separating the backward and forward modes for an isotropic system, and indicating the presence of system asymmetry through changes in the magnitude of the reverse dFRF. The analysis frequency range was increased to cover both positive and negative values to account for the properties of the dFRF, standard AMI's reliance on the conjugate-even property of the FRF was removed, and a new complex least squares curve-fitting routine was developed.

Analysis of two simple systems was conducted with both standard and Two-Sided AMI. The testing showed that, for an isotropic system, processing the dFRF lead to the identification of more modes than the processing of the FRF, due to forward and backward modes being split into the positive and negative frequency ranges of the dFRF. The testing also proved that the presence of system anisotropy negated the advantage that processing the dFRF held over processing the FRF, because both forward and backward modes gave significant contributions in both positive and negative frequency ranges. Additionally, the results showed that standard and Two-Sided AMI offer comparable levels of performance when processing standard FRFs. Increased damping levels were shown to decrease the total number of modes identified (relative to the number of modes in the analytical solution), as well as to decrease the accuracy of estimates for  $\text{Re}(\lambda_k)$ .

Work using the simplified model of the prototypical system to determine if hydrodynamic bearing wear could be detected before the bearing clearance level exceeded normal operating limits was discussed in Chapter V. Both the FRF and the dFRF data formats were used in the testing. Four eigenvalue-based metrics and four modal residue-based metrics for bearing wear were evaluated. The deleterious effects of damping on the number of modes detected and on the accuracy of the estimates for  $\text{Re}(\lambda_k)$ , as seen in Chapter IV, were demonstrated again. The most sensitive eigenvalue-based metric was *percent change*



in  $\text{Im}(\lambda_k)$ ; however, all four residue-based metrics exhibited better consistency in mode detection than the eigenvalue-based metrics. The most promising residue-based metric, *percent change in  $|A_k|$*  detected a 26% average increase in bearing clearance. Processing FRF data gave better results than processing dFRF data. This preliminary study indicated that detection of wear, while the bearing is still operating in the normal range of clearances, is possible with AMI. This could lead to an improvement in the current state of the art, since bearing wear could become a primary diagnosis.

Performing experimental modal analysis (EMA) on non-modal data, for the purpose of shaft crack detection, was explored in Chapter VI through the use of the standard model of the prototypical system. Since the cracked configuration of the prototypical system is time-varying with respect to both the fixed and moving coordinate systems, only non-modal response data was available. AMI and Two-Sided AMI processed this non-modal data as if it were modal data. Six metrics were evaluated.

The metrics *change in  $\text{Im}(\lambda_k)$* , *change in  $|A_k|$* , and *change in  $\text{Re}(A_k)$*  delivered the three best combinations of sensitivity (measure of how small a defect is detectable) and consistency (measure of how many data types the defect is detectable with) in both the moving and fixed coordinate systems with clean data. (In the moving coordinate system with clean data, *change in  $\arg(A_k)$*  demonstrated sensitivity at the level of *change in  $\text{Im}(\lambda_k)$*  with lower consistency.) The inclusion of time domain noise led to decreases in consistency and sensitivity for each metric. Shaft cracks of 0.1 and 0.3 relative depths were detected using the *change in  $\text{Im}(\lambda_k)$*  metric with clean and noisy fixed coordinate system data, respectively. For noisy data, the results showed that this metric had better crack detection sensitivity with fixed coordinate system data (0.3 relative depth crack detected), as compared with moving coordinate system data (0.4 relative depth crack detected). The metric *change in  $\text{Re}(\lambda_k)$*  demonstrated below average sensitivity and excellent resistance to the effects of noise for both fixed and moving coordinate data. *Change in  $\text{Re}(\lambda_k)$*  detected a 0.4 relative depth crack regardless of noise state or coordinate system. For noisy data, the sensitivity of the residue-based metrics with data from the fixed coordinate system data was better than the sensitivity with moving coordinate system data. With noisy, fixed coordinate system

data, both *change in*  $|A_k|$ , and *change in*  $\text{Re}(A_k)$  detected a 0.3 relative depth crack.

Crack detection through EMA processing of noisy, non-modal data was found to be feasible. The results suggested that the least complex diagnostic scheme with the best chance of detecting a shaft crack would track  $\text{Re}(\lambda_k)$ ,  $\text{Im}(\lambda_k)$ ,  $\text{Re}(A_k)$ , and  $|A_k|$  from fixed coordinate system FRF and dFRF data. Implementation of this technique could lead to improved shaft crack detection methods in industry. A change in operating condition and/or a detailed analytical model of the system might no longer be required, as they currently are with many existing methods. There is a need for additional study in this area.

AMI processing of non-modal data for crack detection demonstrated a promising level of reliability. For instance, with noisy, fixed coordinate data, the crack was detectable with four of the six metrics. Both types of metrics (eigenvalue-based and residue-based) were included in the group of four. One of these four metrics, *change in*  $|A_k|$ , detected the crack with  $H_{ZZ}$ ,  $H_{PG}$ , and  $H_{P\hat{G}}$  data. The results showed that the concept is not solely dependent on one metric, one data type, or one modal property for success.

A well-known indicator of a shaft crack, the peak in the system frequency response at two times the shaft run speed ( $2X$ ), was not addressed in this work. The particular combination of shaft speed used in the analysis and the properties of the system model led to the  $2X$  peak being very close to a mode of the nominal system. Zooming into the FRF in the low-frequency range showed that the  $2X$  peak did indeed appear when the crack was introduced into the system model. The magnitude of the adjacent system peak was considerably larger than that of the  $2X$  peak, however. This amplitude difference, coupled with the width of the system peak resulting from high levels of system damping, made the identification of the  $2X$  peak by AMI and Two-Sided AMI essentially impossible. Since identifying the  $2X$  peak and tracking changes in it as the crack progressed were not goals of the study, the proximity of the  $2X$  peak to a nominal system mode did not impact the results. It is important to note that an investigator should be aware of the implications of the appearance of a  $2X$  peak while analyzing rotating equipment with AMI. If the combination of nominal system modes and shaft run speed is favorable, a new  $2X$  peak,

resulting from a shaft crack, would be identified by AMI. Furthermore, if the investigator suspects a shaft crack, the residual FRF, which is the original FRF minus all modal content identified by AMI, could be enlarged and scanned visually in the appropriate frequency range.

In Chapter *VII*, the investigation of defect detection by conducting EMA on non-modal data was continued in a multiple-defect study using the standard model of the prototypical system. The metrics *change in  $\text{Im}(\lambda_k)$*  and *change in  $|A_k|$* , which delivered the best performance in the two single-defect studies involving bearing wear and a shaft crack, were evaluated. Only noisy, fixed coordinate system data were used.

Shaft cracks of 0.3 relative depth and bearing wear as light as a 20% increase in clearance were detected in the presence of another defect. The metrics *change in  $\text{Im}(\lambda_k)$*  and *change in  $|A_k|$*  were proven to be effective at detecting bearing wear in a multiple-defect environment. The normal dFRF,  $H_{PG}$ , was the best data type for bearing wear detection, and the  $H_{ZZ}$  FRF was the worst. Both metrics were able to detect a shaft crack in the multiple-defect study, and crack detection was possible all three data types. For the case of constant bearing wear and increasing shaft crack depth, it was shown that the crack detection performance of both metrics was robust regarding the presence of multiple types of defects. The constant-depth crack with increasing bearing wear analysis showed that the sensitivity to bearing wear of the *change in  $\text{Im}(\lambda_k)$*  and the *change in  $|A_k|$*  metrics was reduced, but not eliminated, by the presence of the crack. (Note that the performance of *change in  $|A_k|$*  supports conclusions about residue-based metrics drawn in Chapter *V*.) Bearing wear in the range of normal operating clearances was detectable with both metrics in the multiple-defect study. The results suggest that AMI would be usable for defect detection of rotating machinery in the presence of multiple system defects, even though the response data are not that of a time-invariant system.

## CHAPTER IX

### FUTURE WORK

A number of areas for future research have been identified during the course of this project. It has been demonstrated that it is possible to detect hydrodynamic bearing wear and a shaft crack in a simple rotordynamic system by analyzing eigenvalues and modal residues estimated by different versions of AMI. Since there are documented needs for improved, on-line methods to detect these defects, more detailed analysis should be done. The concepts developed here should be evaluated in greater depth, with both physical equipment and more complex analytical models.

Introductory experimental work with physical equipment should employ systems of the same level of complexity as the prototypical system investigated here. That is, the system should have a single shaft with one disk and plain journal bearings. The analytical model could easily be modified to account for the physical system's geometry. The analyses described in Chapters *V*, *VI*, and *VII* of the present work could be repeated with the physical system. The updated analytical model could provide comparison data to further evaluate the defect detection techniques described here. If any damage metrics still show promise after this introductory experimental work, a more complicated physical system (and corresponding analytical model) should be developed and tested. Some obvious extensions in the move to a more complicated physical system are fluid-loaded rotors, shaft seals, and more advanced hydrodynamic bearings.

The crack detection work should be extended to machinery supported by rolling element bearings. The hydrodynamic bearings in the prototypical system provide significant damping compared to rolling element bearings. The new investigation would reveal whether this damping helps or hinders crack detection. A large segment of installed equipment is supported on rolling element bearings, and the knowledge from this additional study would help determine which classes of equipment would be best suited to crack detection using

AMI. The goal of the additional work would not be to detect defects in the rolling element bearing, since there is mature, available technology to do so.

In the studies presented here, AMI and Two-Sided AMI processed frequency response data over the complete frequency range of a given data set. When the profile of the data made it impossible for AMI to extract additional modes (or peaks), the Subtraction phase ended. The author did not manually “zoom in” to a smaller frequency range and allow AMI to continue mode identification. This was done to evaluate the hypothesis under the harshest condition: the situation in which the technician in the field has no previous knowledge of the machine’s vibratory characteristics. Two opportunities for future work present themselves. First, a determination of whether there is improved defect detection performance when the user manually limits the frequency range of AMI operation in order to concentrate on modes of the nominal system or identified peaks resulting from previous damage states is in order. Second, if this leads to improved performance, development of an automated method to “zoom in” to the appropriate frequency ranges would be of great benefit.

Allen and Ginsberg have developed a multi-input-multi-output (MIMO) version of AMI to improve standard AMI’s performance in the detection of close modes [3]. Performance of the modified algorithm, relative to other existing EMA methods, with response data from an actual structure is discussed in [3]. In the literature, the dFRF has been shown to effectively separate the closely spaced forward and backward modes of rotating equipment, and the present work demonstrated that this is a great aid in EMA. However, this benefit only occurs with isotropic systems. Processing standard FRFs with Allen and Ginsberg’s MIMO version of AMI may lead to an identification method for backward and forward modes that is not subject to the effects of system anisotropy.

A major limitation on the work presented here was the time required for time domain solutions of the standard model of the prototypical system. If further work is to be done using response data generated by an analytical model, increasing the speed of solution is a good topic for exploration. Investigating Floquet theory appears to be a logical initial activity.

Variable-speed testing would yield a large amount of diagnostic information for machinery that operates in such a manner. Since system stiffness and damping vary with speed in rotating structures, system natural frequencies and damping ratios also vary with speed. The basic premise of the constant-speed analysis was to detect changes in system physical parameters by detecting changes in AMI estimates of eigenvalues and residues. Since measurement and excitation was only at the bearing locations, there was a chance to miss modes in the analysis if they had very low response at the measurement locations. Variable-speed testing would give an improved opportunity to detect system physical parameter changes because the number of data sets (the number of shaft speeds analyzed) would be much greater. Testing over a range of shaft speeds would increase the probability of having modes with non-zero response at the measurement locations.

## APPENDIX A

### BEARING COEFFICIENTS

Vance [65] and Lee [38] presented the stiffness and damping coefficients of plain hydrodynamic bearings using the short-bearing approximation. An overview of the derivation of the coefficients is given in this Appendix, and the equation for each stiffness and damping coefficient is presented. The method used to calculate specific values of the coefficients, based on operating conditions and the physical characteristics of the prototypical system, is discussed.

#### *A.1 Derivation*

Considering linearized stiffness and damping coefficients and assuming small displacements and velocities relative to a steady state equilibrium position yields the equilibrium equation in terms of bearing coefficients.

$$\begin{Bmatrix} F_Y \\ F_Z \end{Bmatrix} = - \begin{bmatrix} k_{YY} & k_{YZ} \\ k_{ZY} & k_{ZZ} \end{bmatrix} \begin{Bmatrix} Y \\ Z \end{Bmatrix} - \begin{bmatrix} c_{YY} & c_{YZ} \\ c_{ZY} & c_{ZZ} \end{bmatrix} \begin{Bmatrix} \dot{Y} \\ \dot{Z} \end{Bmatrix} \quad (84)$$

Here,  $k_{ij}$  and  $c_{ij}$  are the dimensional stiffness and damping coefficients, and  $Y$  and  $Z$  are displacements in the  $Y$  and  $Z$  directions of the fixed  $XYZ$  coordinate system used in the thesis. Forces are represented by  $F$ . Solution of Reynolds' equation is required to determine the nonlinear forces generated by the bearing's fluid film. The general two-dimensional Reynolds' equation, ignoring the squeeze-film term and expressed in stationary cylindrical coordinates  $(r, \theta, X)$ , is

$$\frac{\partial}{\partial X} \left[ \frac{h^3}{6\mu} \frac{\partial P}{\partial X} \right] + \frac{1}{R^2} \frac{\partial}{\partial \theta} \left[ \frac{h^3}{6\mu} \frac{\partial P}{\partial \theta} \right] = \Omega \frac{\partial h}{\partial \theta}. \quad (85)$$

Here,  $h$  is the film thickness,  $P$  is the pressure in the film,  $R$  is the journal radius,  $\mu$  is fluid viscosity, and  $\Omega = 2\pi N$  rad/s. ( $N$  is the shaft speed in RPM.) The short-bearing approximation is valid for bearings with length-to-diameter ratios less than 0.3,

or  $L/D < 0.3$ . The approximation states that since the pressure gradient in the axial ( $X$ ) direction is much greater than the pressure gradient in the angular ( $\theta$ ) direction, the pressure gradient in the angular direction can be set to zero.

$$\begin{aligned}\frac{\partial P}{\partial X} &\gg \frac{\partial P}{\partial \theta} \\ \frac{\partial P}{\partial \theta} &\equiv 0\end{aligned}\tag{86}$$

Substituting this approximation into Eq. 85 leads to a simplified version of Reynold's equation.

$$\frac{\partial}{\partial X} \left[ \frac{h^3}{6\mu} \frac{\partial P}{\partial X} \right] = \Omega \frac{\partial h}{\partial \theta}.\tag{87}$$

The Half Sommerfeld (or  $\pi$ -film) boundary condition is imposed on the pressure distribution of the lubricant inside the bearing. Pressure is positive in the region of the bearing where the fluid film generates load support. The pressure is set to 0 to in the region where the film ruptures and does not provide load support.

$$\begin{aligned}P(\theta, X) &> 0 \text{ for } 0 < \theta < \pi \\ P(\theta, X) &= 0 \text{ for } \pi \leq \theta \leq 2\pi\end{aligned}\tag{88}$$

Using these boundary conditions, the forces generated by the fluid film are determined by integrating the pressure distribution  $P(\theta, X)$  over the area of positive pressure under steady state operating conditions. The bearing stiffness and damping coefficients are related to the fluid film forces by Eq. 84. The resulting coefficients are nondimensionalized in both [65] and [38] in the following manner.

$$\begin{aligned}K_{ij} &= \frac{k_{ij}C}{W} \\ C_{ij} &= \frac{c_{ij}C}{W}\end{aligned}\tag{89}$$

Here,  $K_{ij}$  and  $C_{ij}$  are nondimensional stiffness and damping coefficients,  $k_{ij}$  and  $c_{ij}$  are the dimensional stiffness and damping coefficients in Eq. 84,  $C$  is the bearing's radial clearance, and  $W$  is the load on the bearing.



The nondimensional stiffness coefficients are

$$\begin{aligned}
K_{YY} &= \frac{4 [\pi^2 + (32 + \pi^2) \epsilon^2 + 2 (16 - \pi^2) \epsilon^4] Q(\epsilon)}{(1 - \epsilon^2)} \\
K_{YZ} &= \frac{\pi [\pi^2 + (32 + \pi^2) \epsilon^2 + 2 (16 - \pi^2) \epsilon^4] Q(\epsilon)}{\epsilon \sqrt{(1 - \epsilon^2)}} \\
K_{ZY} &= \frac{-\pi [\pi^2 - 2\pi^2 \epsilon^2 - (16 - \pi^2) \epsilon^4] Q(\epsilon)}{\epsilon \sqrt{(1 - \epsilon^2)}} \\
K_{ZZ} &= 4 [2\pi^2 + (16 - \pi^2) \epsilon^2] Q(\epsilon)
\end{aligned} \tag{90}$$

The nondimensional damping coefficients are

$$\begin{aligned}
C_{YY} &= \frac{2\pi [\pi^2 + 2 (24 - \pi^2) \epsilon^2 + \pi^2 \epsilon^4] Q(\epsilon)}{\epsilon \sqrt{(1 - \epsilon^2)}} \\
C_{YZ} &= C_{ZY} = 8 [\pi^2 + 2 (\pi^2 - 8) \epsilon^2] Q(\epsilon) \\
C_{ZZ} &= \frac{2\pi \sqrt{(1 - \epsilon^2)} [\pi^2 + 2 (\pi^2 - 8) \epsilon^2] Q(\epsilon)}{\epsilon}
\end{aligned} \tag{91}$$

In Eqs. 90 and 91,  $\epsilon$  is the bearing's eccentricity ratio. This quantity is defined as the ratio of eccentricity ( $e$ ) to radial clearance ( $C$ ).

$$\epsilon = \frac{e}{C} \tag{92}$$

The eccentricity function,  $Q(\epsilon)$  is

$$Q(\epsilon) = \frac{1}{[\pi^2 (1 - \epsilon^2) + 16\epsilon^2]^{1.5}} \tag{93}$$

## ***A.2 Coefficient Calculation***

The nondimensional Sommerfeld number is used in the calculation of the proper values of the stiffness and damping coefficients for a specific operating condition. The Sommerfeld number,  $S$ , can be written in terms of the geometry of the bearing, the fluid viscosity, and the load on the bearing.

$$S = \frac{\mu N}{W} \left( \frac{R}{C} \right)^2 \frac{L^3}{D}. \tag{94}$$

The Sommerfeld number can also be expressed in terms of eccentricity ratio.

$$S = \frac{(1 - \epsilon^2)^2}{\pi \epsilon \sqrt{\pi^2 (1 - \epsilon^2) + 16 \epsilon^2}}. \quad (95)$$

In the thesis, the load on each bearing,  $W$ , is taken to be half of the weight of the system (shaft plus attached disk), expressed in Newtons. For a given lubricant, operating speed, bearing geometry, and system weight, the right-hand side of Eq. 94 is fully defined. The resulting value of the Sommerfeld number,  $S$ , is then substituted into the left-hand side of Eq. 95. Standard root-finding techniques are used to solve for the corresponding eccentricity ratio,  $\epsilon$ . The eccentricity ratio is then substituted into Eqs. 93, 90 and 91 to calculate the corresponding nondimensional stiffness and damping coefficients of the bearing.

## REFERENCES

- [1] AENIS, M., KNOPF, E., and NORDMANN, R., “Active magnetic bearings for the identification and fault diagnosis in turbomachinery,” *Mechatronics*, vol. 12, no. 8, pp. 1011–1021, 2002.
- [2] ALLEN, M. and GINSBERG, J., “A linear least-squares version of the algorithm of mode isolation for identifying modal properties. part ii: Application and assessment,” *Journal of Acoustical Society of America*, vol. 116, no. 2, pp. 908–915, 2004.
- [3] ALLEN, M. and GINSBERG, J., “Global, hybrid, mimo implementation of the algorithm of mode isolation,” in *IMAC-XXIII Conference Exposition on Structural Dynamics*, (Orlando, FL), Society for Experimental Mechanics, 2005.
- [4] ALLEN, M. and GINSBERG, J., “Floquet modal analysis to detect cracks in a rotating shaft on anisotropic supports,” in *24th International Modal Analysis Conference (IMAC XXIV)*, (St. Louis, MO), 2006.
- [5] ANALOG DEVICES, I., “Analog devices adxl202/adxl210 technical specification and datasheet,” tech. rep., 1999 1999.
- [6] API, *API Standard 670: Vibration, Axial-Position, and Bearing-Temperature Monitoring Systems*. Washington, DC: American Petroleum Institute, 4th ed., 2000.
- [7] BEIRYLA, D., TRETHEWEY, M., LISSENDEN, C., M.S., L., and MAYNARD, K., “Shaft crack monitoring via torsional vibration analysis; part 1 - laboratory tests,” in *IMAC-XXIII: A Conference and Exposition on Structural Dynamics*, (Orlando, FL), Society for Experimental Mechanics, 2005.
- [8] BENGISU, M., “Spectral shifting due to vibration transmission from rotating bodies 94-wa/nca-3,” in *1994 International Mechanical Engineering Congress Exhibition, of the Winter Annual Meeting*, vol. NCA, (Chicago, IL), ASME, 1994.

- [9] BLOCH, H. and GEITNER, F., *Practical Machinery Management for Process Plants, Volume 2: Machinery Failure Analysis and Troubleshooting*, vol. 2. Houston, TX: Gulf Publishing Company, third ed., 1997.
- [10] BUCHER, I. and EWINS, D., “Modal analysis and testing of rotating structures,” *Philosophical Transactions of the Royal Society Of London Series A - Mathematical Physical and Engineering Sciences*, vol. 359, no. 1778, pp. 61–96, 2001.
- [11] BUCHER, I. and SHOMER, O., “Detecting aysmmetry in rotating structures a combined actuation and signal processing approach,” in *IMAC-XXIII: A Conference and Exposition on Structural Dynamics*, (Orlando, FL), Society for Experimental Mechanics, 2005.
- [12] CASEY, C., *Crack Detection In Rotor Dynamic System By Vibration Monitoring*. Ms, Georgia Institute of Technology, 2000.
- [13] CHILDS, D., *Turbomachinery Rotordynamics*. New York: John Wiley and Sons, 1993.
- [14] DIMAROGONAS, A., “Vibration of cracked structures: A state of the art review,” *Engineering Fracture Mechanics*, vol. 55, no. 5, pp. 831–857, 1996.
- [15] DIMAROGONAS, A. and PAIPETIS, S., *Analytical Methods in Rotor Dynamics*. Applied Science Publishers, 1983.
- [16] EHRLICH, F., ed., *Handbook of Rotordynamics*. Malabar, FL: Krieger Publishing Company, 2nd ed., 1999.
- [17] EISENMANN SR., R. and EISENMANN JR., R., *Machinery Malfunction Diagnosis And Correction*. Upper Saddle River, NJ: Prentice Hall PTR, 1998.
- [18] ERICSSON, S., GRIP, N., JOHANSON, E., PERSSON, L., SJOBERG, R., and STROMBERG, J., “Towards automatic detection of local bearing defects in rotating machines,” *Mechanical Systems and Signal Processing*, vol. 19, no. 3, pp. 509–535, 2005.

- [19] EWINS, D., *Modal Testing; Theory, Practice, and Application*. Philadelphia, PA: Research Studies Press, 2nd ed., 2000.
- [20] EWINS, D. and GUTIERREZ-WING, E., “Modal characterisation of rotating machines,” in *IMAC-XIX: A Conference on Structural Dynamics*, vol. 2, (Kissimmee, FL), pp. 1249–1256, 2001.
- [21] GARRETT, P., GUINDON, E., TRETHEWEY, M., LEBOLD, M., and MAYNARD, K., “Shaft crack monitoring via torsional vibration analysis; part 2 - field applications,” in *IMAC-XXIII: A Conference and Exposition on Structural Dynamics*, (Orlando, FL), Society for Experimental Mechanics, 2005.
- [22] GASCH, R., “Dynamic behavior of simple rotor with a cross-sectional crack,” in *Vibrations in Rotating Machinery*, (Cambridge, UK), p. 123, Institue of Mechanical Engineers, 1976.
- [23] GINSBERG, J., *Mechanical and Structural Vibrations*. New York: John Wiley and Sons, 2001.
- [24] GINSBERG, J. and ALLEN, M., “A linear least-squares version of the algorithm of mode isolation for identifying modal properties. part i: Conceptual development,” *Journal of Acoustical Society of America*, vol. 116, no. 2, pp. 900–907, 2004.
- [25] GOLDMAN, P., MUSZYNSKA, A., BENTLY, D., DAYTON, K., and GARCIN, M., “Application of perturbation methodology and directional filtering for early rotor crack detection 99-gt-225,” in *ASME International Gas Turbine and Aeroengine Congress and Exhibition (IGTI 1999)*, (Indianapolis, IN), ASME, 1999.
- [26] GREEN, I. and CASEY, C., “Crack detection in a rotor dynamic system by vibration monitoring - part i: Analysis,” in *ASME Turbo Expo 2003. Power for Land, Sea, and Air*, (Atlanta, GA), ASME, 2003.
- [27] GUDMUNDSON, P., “The dynamic behavior of slender structures with cross-sectional cracks,” *Journal of Mech. Phys. Solids*, vol. 31, pp. 329–345, 1983.

- [28] HASHIMOTO, H., WADA, S., and KATSUHIRO, N., "Performance characteristics of worn journal bearings in both laminar and turbulent regimes. part i: Steady-state characteristics," *ASLE Transactions*, vol. 29, no. 4, pp. 565–571, 1986.
- [29] HASHIMOTO, H., WADA, S., and KATSUHIRO, N., "Performance characteristics of worn journal bearings in both laminar and turbulent regimes. part ii: Dynamic characteristics," *ASLE Transactions*, vol. 29, no. 4, pp. 572–577, 1986.
- [30] HUANG, S., HUANG, Y., and SHIEH, S., "Vibration and stability of a rotating shaft containing a transverse crack," *Journal of Sound and Vibration*, vol. 162, no. 3, pp. 387–401, 1993.
- [31] IMREGUN, M. and SANLITURK, K., "Natural frequency and damping changes produced by fatigue cracks," in *15th International Seminar on Modal Analysis and Structural Dynamics*, (Leuven, Belgium), pp. 791–805, 1990.
- [32] JAKEMAN, R., "Performance of oil film dynamic coefficients of a misaligned stern tube bearing," *ASLE Transactions*, vol. 29, no. 4, pp. 441–450, 1986.
- [33] JOH, Y. and LEE, C., "Excitation methods and modal parameter identification in complex modal testing of rotating machinery," *Modal Analysis: The International Journal of Analytical and Experimental Modal Analysis*, vol. 8, no. 3, pp. 179–203, 1993.
- [34] JOH, Y. and LEE, C., "Use of dfrfs for diagnosis of asymmetric/anisotropic properties in rotor-bearing system," *Journal of Vibration and Acoustics*, vol. 118, no. 1, pp. 64–69, 1996.
- [35] KIKUCHI, K., "Analysis of unbalance vibration of rotating shaft system with many bearings and disks," *Bulletin of Japanese Society of Mechanical Engineers*, vol. 13, no. 61, pp. 864–872, 1970.

- [36] KOIZUMI, T., TSUJIUCHI, N., and SAKAI, T., “Diagnosis for rotating shaft using adaptive modal parameter identification method,” in *IMAC 17*, vol. 2, (Kissimmee, FL), pp. 1974–1979, 1999.
- [37] KREUZINGER-JANIK, T. and IRRETIER, H., “Unbalance identification of flexible rotors based on experimental modal analysis,” in *7th International Conference on Vibrations in Rotating Machinery*, (Nottingham, UK), pp. 335–346, IMechE, 2000.
- [38] LEE, C., *Vibration Analysis of Rotors*. Dordrecht, The Netherlands: Kluwer Academic Publishers, 1993.
- [39] LEE, C. and KWON, K., “Crack detection in rotating machinery by modal testing,” in *7th International Conference on Vibrations in Rotating Machinery*, (Nottingham, UK), pp. 535–543, IMechE, 2000.
- [40] LEES, A. and FRISWELL, M., “The evaluation of rotor imbalance in flexibly mounted machines,” *Journal of Sound and Vibration*, vol. 208, no. 5, pp. 671–683, 1997.
- [41] LOPARO, K., ADAMS, M., LIN, W., ABDEL-MAGIED, M., and AFSHARI, N., “Fault detection and diagnosis of rotating machinery,” *IEEE Transactions On Industrial Electronics*, vol. 47, no. 5, pp. 1005–1014, 2000.
- [42] MARSCHER, W., “Modal testing of rotating machinery while it is operating,” *Sound and Vibration*, vol. 33, pp. 29–32, 1999 1999.
- [43] MAYES, I. and DAVIES, W., “The vibrational behaviour of a rotating shaft system containing a transverse crack,” in *Vibrations In Rotating Machinery*, (Cambridge, UK), pp. 53–64, Institute of Mechanical Engineers, 1976.
- [44] MESQUITA, A., DIAS, M., and MIRANDA, U., “A comparison between the traditional frequency response function (frf) and the directional frequency response function (dfrf) in rotordynamic analysis,” in *First South American Congress On Computational Mechanics, MECOM 2002*, vol. XXI, (Santa Fe-Parana, Argentina), 2002.

- [45] MUSZYNSKA, A., “Effects of an oversize, poorly lubricated bearing on rotordynamic response. part i: Experimental results, part ii: Analytical modeling,” in *Fourth International Symposium on Transport Phenomena and Dynamics of Rotating Machinery (ISROMAC-4)* (KIM, W.-J. Y. and J.H., eds.), vol. 2, (Honolulu, HI), pp. 1105–1125, Begell House, Inc, 1992.
- [46] NORDMANN, R., “Identification of modal parameters of an elastic rotor with oil film bearings,” *Journal of Vibration, Acoustics, Stress, and Reliability in Design*, vol. 106, pp. 107–112, 1984.
- [47] NORDMANN, R. and SHOLLHORN, K., “Identification of stiffness and damping coefficients of journal bearings by means of the impact method,” in *International Conference on Vibration in Rotating Machinery (ISROMAC)*, (Cambridge, England), pp. 231–238, Insitute of Mechanical Engineers, 1980.
- [48] PANTELIOU, S., CHONDROS, T., and ARGYRAKIS, V., “Damping factor as an indicator of crack severity,” *Journal of Sound and Vibration*, vol. 241, no. 2, pp. 235–245, 2001.
- [49] PAPADOPOULOS, C. and DIMAROGONAS, A., “Coupled longitudinal and bending vibrations of a rotating shaft with an open crack,” *Journal of Sound and Vibration*, vol. 117, pp. 81–93, 1987.
- [50] RANDALL, R., “State of the art in monitoring rotating machinery,” in *ISMA 2002: Conference on Noise and Vibration Engineering*, vol. IV, (Leuven, Belgium), pp. 1457–1477, 2002.
- [51] RAO, J., *Rotordynamics*. Wiley Eastern, 1983.
- [52] REDMOND, I., “Defect identification in rotordynamic systems,” in *IMAC-XV*, (Orlando, FL), pp. 845–856, 1997.
- [53] RICHARDS, J., *Analysis Of Periodically Time-Varying Systems*. Berlin: Springer-Verlag, 1st ed., 1983.



- [54] SABNAVIS, G., KIRK, R., KASARDA, M., and QUINN, S., “Cracked shaft detection and diagnostics: A literature review,” *The Shock and Vibration Digest*, vol. 36, no. 4, pp. 287–296, 2004.
- [55] SAN ANDRES, L., “The effect of journal misalignment on the operation of a turbulent flow hydrostatic bearing,” *Journal of Tribology*, vol. 115, pp. 355–363, 1993.
- [56] SAN ANDRES, L. and DE SANTIAGO, O., “Field methods for identification of bearing support parameters. part i - identification from transient rotor dynamic response due to impacts,” in *ASME Turbo Expo: Power for Land, Sea, and Air*, (Atlanta, GA), ASME, 2003.
- [57] SANDERSON, A., “The vibration behavior of a large steam turbine generator during crack propogation through the generator rotor (paper c432/102),” in *International Conference on Vibrations in Rotating Machinery (IMEchE)*, (Bath, UK), pp. 263–273, (IMEchE), 1992.
- [58] SANLITURK, K. and IMREGUN, M., “Theoretical modelling of the damping produced by fatigue cracks,” in *9th International Modal Analysis Conference*, vol. 2, (Florence, Italy), pp. 1370–1374, 1991.
- [59] SCHARRER, J., HECHT, R., and HIBBS, R., “Effects of wear on the rotordynamic coefficients of a hydrostatic journal bearing, 90-trib-20,” in *Joint ASME/STLE Tribology Conference*, (Toronto, Ont, Can), ASME, 1990.
- [60] SEKHAR, A., “Detection and monitoring of cracks in rotors through q factors,” *Proceedings of the Institution of Mechanical Engineers, Part C: Journal of Mechanical Engineering Science*, vol. 214, no. 7, pp. 949–954, 2000.
- [61] SHAMPINE, L., GLADWELL, I., and THOMPSON, S., *Solving ODEs with MATLAB*. Cambridge, UK: Cambridge University Press, 2003.
- [62] SHIGLEY, J. and MISCHKE, C., *Mechanical Engineering Design*. New York: McGraw-Hill, 5 ed., 1989.

- [63] SUBBIAH, R., BHAT, R., and SANKAR, T., “Rotational stiffness and damping coefficients of fluid film in a finite cylindrical bearing,” *ASLE Transactions*, vol. 29, no. 2, pp. 414–422, 1985.
- [64] THE MATHWORKS, I., “Matlab 7,” 2004.
- [65] VANCE, J., *Rotordynamics of Turbomachinery*. New York: Wiley, 1988.
- [66] WAUER, J., “Cracked rotor dynamics: A state of the art review,” *Applied Mechanics Reviews*, vol. 43, pp. 13–17, 1990.
- [67] WAUER, J., “Modelling and formulation of equations of motion for cracked rotating shafts,” *International Journal of Solids and Structures*, vol. 26, no. 8, pp. 901–914, 1990.
- [68] WILLIAMS, J., *Engineering Tribology*. Oxford: Oxford University Press, 1994.
- [69] WU, J., “Detection of simulated journal bearing wear using vibration analysis,” Tech. Rep. AD-A007142; USAMC-ITC-02-08-73-005, Army Material Command, Intern Training Center, 1974 1974.
- [70] WU, M. and HUANG, S., “Vibration and crack detection of a rotor with speed-dependent bearings,” *International Journal of Mechanical Sciences*, vol. 40, no. 6, pp. 545–555, 1998.
- [71] ZACHARIADIS, D., “Short bearing model for the evaluation of journal’s dynamic angular misalignment effects on rotor vibrations, 98-gt-397,” in *Proceedings of the International Gas Turbine and Aeroengine Congress and Exhibition*, (Stockholm, Sweden), ASME, 1998.
- [72] ZHANG, W. and TESTA, R., “Closure effects on fatigue crack detection,” *Journal of Engineering Mechanics*, vol. 125, no. 10, pp. 1125–1132, 1999.
- [73] ZIRKELBACK, N. and GINSBERG, J., “Ritz series analysis of rotating machinery: Validation, convergence, mode functions, and unbalance response,” *ASME Journal of Vibration and Acoustics*, vol. 123, pp. 492–501, 2002.